NUMERICAL MODELLING OF BEACH RECOVERY FOLLOWING A STORM EVENT

A HYBRID BEHAVIOURAL / PROCESS-BASED APPROACH

BY TIM VAN DAM

Cover designed by Sander Kruit

Numerical Modelling of Beach Recovery Following a Storm Event

A hybrid behavioural / process-based approach

by
Tim van Dam

in partial fulfilment of the requirements for the degree of

Master of Science
in Civil Engineering

Delft University of Technology
November 2019

Graduation committee:

Prof. dr. ir. S. G. J. (Stefan) Aarninkhof	(chair)	TU Delft
Dr. ir. R. T. (Robert) McCall		Deltares
Dr. ir. A. R. (Ap) van Dongeren		Deltares / IHE Delft
Dr. M. D. (Mitchell) Harley		UNSW / Water Research Laboratory
Prof. I. L. (Ian) Turner		UNSW / Water Research Laboratory
Dr. ir. M. F. S. (Marion) Tissier		TU Delft

Abstract

Sandy beaches are found along a large part of the world's coastline, and form the highly dynamic interface between sea and land. The dynamic nature of beaches is best displayed during storms as large amounts of sand are eroded in a matter of hours, potentially causing coastline retreat and increased vulnerability to the area behind it. Subsequent natural beach recovery is a longer-term wave-driven process where eroded sediment is transported back onshore to rebuild the beach towards its pre-storm conditions, providing coastal protection as it used to before.

While an abundance of numerical models is developed to simulate the morphological response to a storm event, the subsequent beach recovery is a process that has received significantly less attention. The complexity in numerical modelling of post-storm beach recovery lies in the importance of small-scale processes within a long-term period of months up to years, making detailed (i.e. process-based) modelling of beach recovery still unsuccessful today. This thesis describes the development of a hybrid behavioural / process-based model (XBeach) that successfully predicts the recovery of the subaerial beach at Narrabeen Beach, Australia, following a severe storm erosion in April 2015. The model is validated on the recovery period following a storm in June 2016 at the same site, and shows promising results.

A literature review provides insight in physical processes that drive onshore sediment transport. Furthermore, a review of conceptual models and formulations forms a basis for describing dependencies between environmental conditions and the morphological response of the beach. This review provides useful tools for the model development that is described in this thesis.

An analysis of the April 2015 and June 2016 storm events at Narrabeen Beach, and subsequent recovery of the subaerial beach, was carried out to identify the recovery process. High-frequency Lidar measurements were used to visualise the evolution of the beach profile, subaerial beach volume, and identify (the evolution of) different behavioural modes (after Phillips, 2018), throughout the recovery period, and provided information on the wave runup.

A 1D wave-averaged numerical model (XBeach Surfbeat, Roelvink et al., 2009) was set up, where the hydrodynamics are resolved on the scale of infragravity motions, and hence does not resolve individual waves and the wave shape itself. The results revealed that the traditional process-based approach does not capture berm growth, and the steep slope that is observed at Narrabeen Beach is not predicted. The recently developed Bermslope model (a behavioural swash zone sediment transport correction model, Roelvink and Costas, 2017) significantly improved the model's ability to predict berm growth as well as the characteristic steep slope. The shortcoming of the Bermslope model is however that the erosive response to episodic storm conditions is not captured, as the model continues to predict accretion during energetic conditions. Furthermore, the vertical growth of the berm is under-estimated.

The Lidar data and literature review were used to develop two model innovations. Firstly, using the concept of morphodynamic beach states (Wright and Short, 1984), and numerous other theoretical studies discussed in the literature review, a dependency between the wave conditions and the magnitude of the Bermslope sediment transport correction was included in the model. Secondly, a model innovation was developed to re-distribute the sediment transport over the upper swash zone, and hence account for incident band swash-induced sediment transport, which is not resolved in XBeach Surfbeat mode.

The results of the developed model showed a major improvement in terms of predicting the behaviour, and the response to episodic storm conditions throughout the recovery period, as well as the vertical extent of berm growth. During calm conditions, the model predicts accretion and berm growth as well as the steep profile that is observed at Narrabeen Beach. During episodic storm conditions, the model predicts erosion and a flatter, dissipative-looking profile which agrees well with the observations. The adapted The model obtains a high model skill after the recovery period of 76 days, in terms of subaerial beach profile (BSS = 0.96) and volume (RMAE = 0.021). The total runup height is predicted reasonably well (corr = 0.83, Rel. BIAS = -0.04), albeit with a significant scatter (SCI = 0.33).

The model is validated on the recovery of the subaerial beach at Narrabeen Beach, following the devastating storm in June 2016. Without any calibration, the model predicts the behaviour throughout the first 100 days of the recovery very well. However, the onshore migration of a sand bar (deposited at a water depth of 4 m) is not captured by the model. Furthermore, net import of sediment due to alongshore sediment transport (220 m^3/m within 6 months) is also not represented in the 1D model. As a consequence, there is not enough sediment supply to the subaerial beach to correctly predict the recovery, and the model skill deteriorates progressively from day 140 to 220. This is a limitation of a 1D simulation, and is not considered as a shortcoming of the present model.

The model results are very promising and show good potential for post-storm beach recovery studies, and long-term morphological coastal modelling in general. The model is very successful in predicting berm growth at a steep reflective beach, as well as episodic storm erosion.

Samenvatting

Een groot deel van de wereldwijde kustlijn bestaat uit zandstranden, en vormt het dynamische raakvlak tussen de zee en het land. De dynamiek van stranden toont zich het best tijdens stormen, waarbij grote hoeveelheden zand door de golven worden geërodeerd en in dieper water terecht komen in slechts enkele uren tot dagen. Hierbij treedt mogelijk een teruggetrokken kustlijn op met als gevolg dat het achterliggende land vergroot risico loopt op overstromingen. Het natuurlijke herstel van het strand is een langere termijn proces dat gestuurd wordt door golven die het zand terug brengen naar de kust, totdat het strand is herbouwd tot zijn oorspronkelijke staat en weer kan functioneren als natuurlijke bescherming.

Hoewel er een overvloed aan numerieke modellen is ontwikkeld die het effect van stormen op de kust kunnen simuleren, is het natuurlijke strandherstel wat hier op volgt minder nauwkeurig bestudeerd en begrepen. De complexiteit van het modelleren van strandherstel ligt in het belang van kleinschalige processen binnen een lange periode van maanden tot jaren, waardoor gedetailleerd procesmatig modelleren van strandherstel tot op de dag van vandaag nog steeds niet succesvol is. In deze thesis wordt de ontwikkeling van een hybride gedrags- / procesmatig model (XBeach) beschreven, welke in staat is om het herstel van het bovenzeese strand op Narrabeen Beach, Australië, te voorspellen, na een ernstige stormerosie in april 2015. Het model is gevalideerd op de herstelperiode na een storm in juni 2016 op dezelfde locatie, en toont veelbelovende resultaten.

Een literatuurstudie geeft inzicht in de fysische processen die een belangrijke rol spelen bij het landwaartse transport van sediment dat uiteindelijk leidt tot het herstel van het strand. Daarnaast vormt een overzicht van conceptuele modellen en formuleringen een basis voor het beschrijven van relaties tussen (golf) condities en de morfologische respons van het strand. Deze review biedt handige hulpmiddelen voor de modelontwikkeling die in deze thesis wordt beschreven en geïmplementeerd.

Een analyse van twee stormen, in april 2015 en juni 2016, en daaropvolgend herstel van het bovenzeese strand van Narrabeen Beach, werd uitgevoerd om het herstelproces te identificeren. Hoogfrequente Lidar-metingen werden gebruikt om de ontwikkeling van het strandprofiel en het bovenzeese strandvolume in kaart te brengen en (de evolutie van) verschillende “gedragsvormen” van het strand (volgens Phillips, 2018) te identificeren, gedurende de herstelperiode, en gaf inzicht in de golfoploop op het strand.

Er is een 1D golfgemiddeld numeriek model (XBeach Surfbeat, Roelvink et al., 2009) opgezet, waarbij de hydrodynamica wordt berekend in de schaal van golfgroepen en individuele golven en de golfvorm zelf wordt dus niet opgelost. De resultaten toonden aan dat het model bij toepassing van de traditionele procesmatige benadering niet in staat is om bermgroei voorspellen en dat de steile helling die wordt waargenomen bij Narrabeen Beach niet wordt correct wordt voorspeld. Het recent ontwikkelde Bermslope model (een corrigerend gedragsmodel voor sedimenttransport in de swash zone, Roelvink and Costas, 2017) verbeterde het vermogen om de groei van de berm en de karakteristieke steile helling te voorspellen aanzienlijk. De tekortkoming van het Bermslope model is echter dat de erosieve respons op episodische stormcondities niet wordt gesimuleerd, omdat het model tijdens energieke golfcondities aangroei blijft voorspellen. Bovendien wordt de verticale groei van de berm onderschat.

Het literatuuronderzoek en de Lidar data zijn gebruikt om twee modelinnovaties te ontwikkelen. Ten eerste, met behulp van het bekende morphodynamic beach states concept (Wright and Short, 1984), en tal van andere studies die in de literatuurstudie zijn besproken, werd een afhankelijkheid tussen de golfcondities en de grootte van de Bermslope sedimenttransport correctie in het model opgenomen. Ten tweede werd een modelinnovatie ontwikkeld om het sedimenttransport binnen de swash zone te herverdelen tot op de juiste hoogte, waarmee sedimenttransport door individuele korte golven wordt vertegenwoordigd, wat niet wordt beschouwd in XBeach Surfbeat.

De resultaten van het ontwikkelde model tonen een grote verbetering ten aanzien van het voorspellen van de geobserveerde gedragsvormen en de respons op episodische stormcondities gedurende de herstelperiode, evenals de verticale omvang van de bermgroei. Tijdens kalme golfcondities voorspelt het model horizontale en/of verticale aangroei van de berm, evenals het steile profiel dat wordt waargenomen bij Narrabeen Beach. Tijdens episodische stormcondities voorspelt het model erosie en een platter, dissipatief ogend profiel dat goed overeenkomt met de waarnemingen. Het ontwikkelde model verkrijgt een hoge score na de herstelperiode van 76 dagen, voor wat betreft de nauwkeurigheid in het voorspellen van het bovenzeese strandprofiel (BSS = 0.96) en volume (RMAE = 0.021). De totale hoogte van de golfoploop wordt tevens redelijk goed voorspeld (corr = 0.83, Rel. BIAS = -0.04), zij het met een significante spreiding (SCI = 0.33).

Het ontwikkelde model is gevalideerd op de herstelperiode van Narrabeen Beach na een vernietigende storm in juni 2016. Zonder enige kalibratie voorspelt het model de eerste 100 dagen van het strand herstel erg nauwkeuring. Er is echter een zandbank in dieper water die langzaam kustwaarts verplaatst, wat niet door het model wordt voorspeld. Bovendien is er een aanzienlijke netto aanvoer van sediment als gevolg van sedimenttransport evenwijdig aan de kust (220 m^3/m in 6 maanden tijd), wat niet in een 1D model wordt berekend. Het gevolg hiervan is dat het model, door een tekort aan sediment aanvoer, het herstel van het bovenzeese strand niet juist voorspelt op de lange termijn, waardoor de nauwkeurigheid van het model sterk afneemt van dag 140 naar 220. Dit is echter een beperking van een 1D berekening, en wordt niet beschouwd als een tekortkoming van het ontwikkelde model.

De modelresultaten zijn veelbelovend en tonen een goed potentieel voor modelstudies naar strandherstel na een storm, en lange termijn simulaties van kustmorfologie in het algemeen. Het model is zeer succesvol in het voorspellen van berm aangroei op een steil strand, en voorspelt tevens nauwkeurig tussentijdse erosie tijdens storm condities.

Acknowledgements

To start off with, thank you very much Stefan, for inviting me to a lunch meeting with Ian, which lead to a collaboration with the Water Research Laboratory (WRL) of the University of New South Wales (UNSW). And before I had the chance to approach Deltares, you already managed to get Ap interested and basically set up the whole committee. Thank you for your involvement, your advice and positivity during the meetings and phone calls we had.

Thank you Ap, for in the first place allowing me to take on this challenge, for your genuine interest in this research, and sharing your highly appreciated opinion – not only on the content, but also on details like the structure and layout of the present report. Furthermore, introducing me to a number of people in the field of coastal engineering has broadened my perspective and provided useful insights.

While the rest of the committee discouraged any further model development, and insisted to focus on finalising the thesis, you and Robert supported my stubbornness. You both pushed me to make the most out of this thesis, and when the report was still far from finished we already sent in an abstract of the present work to the ICCE. I'm looking forward to writing a publication on numerical modelling of post-storm beach recovery using XBeach.

Robert, thank you for your guidance on the compiling and coding part of this study. Incorporating a smoothing time in the runup formulation solved the stability issue I was struggling with. This eventually made my final model innovation successful, and significantly improved the model's performance, and the overall value of this research. Your contribution during the discussions we had is much appreciated, as well as your critical review on my conclusions chapter.

Mitch, from the start you were really involved, and you prevented me from getting lost in the details of wave-by-wave profile changes, while the focus was on the long-term recovery process. Thank you for helping me getting organised, showing me around at the lab and the UNSW campus, and for taking me to Narrabeen Beach to carry out the monthly site measurement (and trusting me in doing this correctly with a AU$ 30.000,- RTK-GPS in my hands).

Ian, when we first met in Stefan's office you immediately got me interested in the Australian coastal morphodynamics.After the (remote) kick-off meeting, you and Mitch kindly invited me to do a part of the research with you at the lab. My stay in Sydney has been a great experience, and feeling welcome at WRL greatly contributed to that. Thanks for taking me with you on the Coastal Engineering field trip and for showing me the 2nd year course you teach at the UNSW.

Marion, I would like to thank you for the helpful discussions and your advice during meetings and via emails. I really appreciate your comments on the report, and your critical review on the literature study in particular.

To all the fellow MSc students at Deltares, thanks for the joyful lunch breaks, interesting discussions and pleasant working atmosphere. To everybody at WRL, thanks for the warm welcome, the lunch lectures and the inspiring Monday morning meetings. Special thanks to Chris for assisting me with the data, and Nash, thanks for the useful discussions on XBeach. Yann and Steve, you really made my time at the lab, and my stay in Sydney more memorable. Thanks for the afternoon runs, surfing experience, beers, nights out, Thai food, and of course the interesting discussions on XBeach, lagoons, subgrid stresses and matrices.

To all my friends, I suppose I don't need to mention any names. Thanks for all the time I get to spend with you guys, during the past months, and all the years before that. I'm grateful and proud to have a group of friends who I consider family since when we were kids.

To my (former) room mates and fellow students, Remy and Radityo, thanks for the productive late night study sessions (with or without Leffe blond), the chess games, gym sessions, and for sharing good food and conversations.

To my family, my brothers, and of course my mum and dad, thank you for always encouraging me to chase my dreams. I didn't always take the easiest path, or make the smartest decisions, but you always supported me, believed in me, and inspired me. Thank you for all of this, and for your genuine interest in basically everything I do.

Lavinia, I appreciate all the time we spend together, whether we're studying, eating, or going to the gym. Somehow you always manage to put a smile on my face and keep me energised. Especially during the last few weeks, you really pushed me to get back to work at times that I lost focus and motivation. Thank you for your support, your patience with me, and all the positive energy.

Contents

Chapter 1

Introduction

1.1 Background

The coastline forms the highly dynamic interface between land and ocean, and provides a wide range of ecosystem services. Besides functioning as a habitat for numerous animal and plant species, and accommodation for recreational purposes (e.g. sunbathing and surfing), it has historically provided the opportunity to access the ocean to thrive (e.g. fishing and trading) and explore the world. It is therefore that a large part of the world population has settled near the coast – approximately 25% living within a distance of 100 km from the coast (Small and Nicholls, 2003) – and the supporting infrastructure is concentrated in these areas.

A recent study reveals that 31% of the world's coastline consists of sandy or gravel beaches, of which 24% is eroding at a rate exceeding 0.5 m per year (Luijendijk et al., 2018). The dynamic nature of beaches is observed on a range of time scales (Stive et al., 2002), as the shoreline responds to e.g. sea level rise (Bruun, 1962), the seasonal variation of the climate (Bosboom and Stive, 2015), and individual storm events (e.g. Harley et al., 2016).

The latter phenomenon displays the dynamic nature of beaches best, as an entire beach can be eroded in a matter of hours to days. Large amounts of sand are washed away and deposited offshore, causing a retreat of the coastline. Besides disruption of habitat for various animal and plant species, and the loss of recreational purposes, this can result in hazardous circumstances with respect to flooding of the hinterland.

Following the severe erosion of a sandy beach after a storm event, sediment is transported back onshore, and the beach and dunes are rebuilt to their pre-storm conditions. This process is much more complex than the erosion during a storm and can be considered to happen in three different phases. The onshore transport, and restoration of the nearshore morphology happens on the time scale of multiple days (e.g. Ranasinghe et al., 2012), while the recovery of the subaerial beach (i.e. the dry beach) may take several months up to years (e.g. Phillips et al., 2015; Phillips, 2018). Finally, the growth of the backbeach and dunes to their pre-storm conditions, which is an aeolian (wind-driven) process, may take several decades (Morton et al., 1994).

The subaerial beach forms the natural buffer of sediment that separates the coastal infrastructure from the sea. The depleted state of the subaerial beach following a storm event leaves the coastal infrastructure and communities vulnerable to subsequent storms (Forbes et al., 2004). An insight in the ability of the beach to recover to its pre-storm conditions, and the temporal scale accompanied with this, is therefore of fundamental importance for coastal management.

Various conceptual, empirical and numerical models have been developed to predict the response to a storm event. Knowledge on the subsequent recovery process, which is essential in order to fulfil in its functional requirements again, is however very limited. The recovery of the subaerial beach following a storm event is a complex wave-driven process, and is accomplished through onshore sediment transport, and exchange of sediment between the surf zone and dry beach. Sediment transport in the swash zone is the primary mechanism for this exchange, and is a complex process that is not very well understood.

In addition to the complexity of the small scale processes in the upper swash zone itself, complexity in numerical modelling of this phenomenon lies in the importance of the short time scales of turbulence and dissipation, within a longer-term recovery process. This range of time and spatial scales makes the long-term modelling computationally very expensive, and requires a simplified approach, which is, today, still not capable of reproducing the observed onshore sediment transport that leads to the recovery of beaches.

Some empirical (Kriebel and Dean, 1993) and equilibrium models (Davidson et al., 2013; Splinter et al., 2014) are developed to simulate long-term morphological change, and capture shoreline progradation and beach recovery. These models are based on empirical formulations and concepts of e.g. equilibrium profile and wave conditions, rather than describing the physical processes. Process-based modelling of beach recovery is however scarcely attempted due the complexities mentioned above.

1.2 Problem definition

The process-based model XBeach (Roelvink et al., 2009) is developed to model the relevant processes in each of the four storm impact regimes (Sallenger, 2000). XBeach is a well-established numerical model in the field of coastal engineering, that is known to have a high predictive skill for storm erosion studies. XBeach is fully valid on dissipative beaches, but on reflective beaches, which are morphodynamically very different from dissipative beaches, the model needs significantly more calibration (Oliveira, 2014). Processes like wave runup are reported to be under-estimated on reflective beaches, and offshore sediment transport in the swash zone is over-predicted (e.g. Van Rooijen, 2011), complicating the simulation of berm growth.

XBeach has been used for long-term simulations, where both storm-induced erosion and subsequent recovery were modelled at Narrabeen Beach, Australia (e.g. Pender and Karunarathna, 2013). However, two different parameter settings were used for the different conditions. Modelling berm growth in XBeach is challenging, which resulted in the recently developed Bermslope model (Roelvink and Costas, 2017) that aims to account for complex swash zone processes. However, this model is not yet tested thoroughly on steep, reflective beaches.

Narrabeen Beach is known for the extensive monitoring programme that is carried out since 1976, and its history of severe storm erosion events. State-of-the-art measurement techniques captured multiple storm events (e.g April 2015 and June 2016) and subsequent natural recovery of the subaerial beach. However, detailed numerical modelling of storm erosion and subsequent recovery of the subaerial beach has not been successful.

1.3 Research question

The aim of this study is to develop an XBeach model that successfully predicts post-storm recovery of the subaerial beach. Due to the temporal scale of the simulation time (i.e. months), computation of short waves is not feasible, and a wave-averaged approach is followed (i.e. XBeach Surfbeat). Assessment of the predictive skill of the currently available model formulations potentially identifies shortcomings. A review on relevant morphodynamic processes and model formulations provides insight to address these potential shortcomings by means of additional model development. This leads to the following research question:

"How can a wave-averaged process-based model (XBeach Surfbeat) be applied to successfully model the recovery of the subaerial beach following a storm event?"

1.4 Objectives

The main objective of the present study is to develop a process-based, wave-averaged model, XBeach Surfbeat, that successfully predicts the post-storm recovery of the subaerial beach. Additional model development might be required to make this possible. In order to meet the main research objective, and answer the research question, the following sub-objectives are formulated:

1. Identify the hydrodynamic and swash zone processes that are important for the onshore transport of sediment and the recovery of the subaerial beach;

2. Analyse the recovery of the subaerial beach following the April 2015 storm at Narrabeen Beach, Australia;

3. Assess the performance of the currently available XBeach model formulations with respect to predicting the observed post-storm beach recovery at Narrabeen Beach, and potentially identify shortcomings;

    a. Assess the "standard" XBeach model performance; and

    b. Explore the recently-introduced "Bermslope" model (Roelvink and Costas, 2017).

4. Develop innovations to the model to account for wave-dependency in the Bermslope sediment transport correction, and account for incident band swash-induced sediment transport in the upper swash zone; and

5. Validate the developed XBeach model on the recovery of the subaerial beach following the June 2016 storm event at Narrabeen Beach, Australia.

1.5 Approach

The aim of this study is to develop an XBeach Surfbeat model that successfully predicts the recovery of the subaerial beach following a storm event. In order to meet this objective, the sub-objectives listed in Section 1.4 are addressed as follows.

1. An analysis of the physical processes in the (nearshore) coastal zone that are responsible for the sediment exchange between the surf zone and the beach is carried out in Chapter 2. Furthermore, different types of models that are developed to describe (the effect of) these processes are explored. This literature review addresses the first sub-objective.

2. Next, an analysis of the study site, Narrabeen Beach, Australia is presented in Chapter 3. This location is chosen due to the impressive amount of data that is available, dating back to 1976, capturing numerous storms, and subsequent recovery processes. The April 2015 storm and subsequent recovery of the subaerial beach are analysed, and a conceptual model (Phillips, 2018) is discussed. This addresses the second research objective, and also elaborates on the insight on physical processes that are important for subaerial beach recovery (sub-objective 1). The analyses provides a basis for the assessment of the model performance.

3. Chapter 4 provides a description of the numerical model XBeach that is used to model beach recovery following the April 2015 storm event at Narrabeen Beach. The model setup is discussed and a small sensitivity analysis is carried out to gain insight in the relevant parameters to calibrate the model.

4. The model results are discussed in Chapter 5. The standard XBeach model (i.e. without Bermslope model) is first tested. Next, the Bermslope model is used to simulate the recovery. The results are compared to the observations, which are presented in Chapter 3. The model performance is quantified by assessing its predictive skill with respect to the evolution of the subaerial beach profile, the evolution of the subaerial beach volume and the behaviour of the beach throughout the recovery period. The results are discussed and shortcomings of the model are summarised.

5. The model assessment (Chapter 5) together with the analysis of the observed beach recovery process (Chapter 3) indicate the potential shortcomings of the current XBeach model. The insight on relevant physical processes and conceptual models of Chapter 2 is then used to address these shortcomings by means of additional model development. The model development – sub-objective 4 – is described in Chapter 6, and the performance of the adapted model will again be verified based on the observations.

6. Finally, the developed model will be validated on the recovery following the June 2016 storm at Narrabeen Beach to address the 5^{th} sub-objective. An analysis of the June 2016 storm, and subsequent recovery is presented in Chapter 7, followed by a brief description of the model setup. The results are presented, followed by a discussion on the model performance.

Chapter 2

Morphodynamics of the coastal zone

2.1 Introduction

The coastal zone is a highly dynamic region, where wave transformation and energy dissipation induced by various complex physical processes continuously reshape its geometry which in turn affects the hydrodynamics again. Understanding of the physical processes that dominate the morphodynamics of the coastal zone is of fundamental importance for the development of numerical coastal models that aim to predict the response of the coastline to the highly variable environmental conditions. While the entire coastal region encompasses a much broader region and range of physical processes, the focus of this study is on the nearshore region, and more specifically on the processes that are responsible for beach recovery following a storm event.

During a storm event, high energy waves erode sediment from the beach and after which it is deposited further offshore as an offshore bar, and cause a retreat of the shoreline. The subsequent recovery process is conducted by the onshore transport of this eroded sediment from the surf zone, through the swash zone, back upon the beachface. Hence, an understanding of the morphodynamics in the swash zone, and the entire nearshore region, is of fundamental importance for the numerical modelling of post-storm beach recovery.

The present chapter provides a literature review on the physical processes, conceptual models and advances in coastal morphodynamic modelling that are considered to be relevant for the numerical modelling of post-storm beach recovery.

The terminology and definitions of the various zones within the nearshore coastal region that are used throughout this thesis are introduced in Section 2.2. Theory on the generation of waves and how they propagate from deep water through the coastal zone is presented in Section 2.3. Section 2.4 discusses the hydrodynamics of the nearshore coastal region and covers physical processes like wave transformation, breaking, setup and runup. Section 2.5 provides a more detailed review on the hydrodynamics and morphodynamics in the swash zone specifically. Section 2.6 is devoted to the well-known concept of morphodynamic beach states (Wright and Short, 1984) and elaborates on the variability of beaches and surf zones. Finally, Section 2.7 provides a review of the wide range of existing models that aim to describe the morphological response of the coast to environmental conditions.

2.2 The coastal zone

The coastal zone consists of various regions in which the dynamics vary significantly. In deep water, the hydrodynamics are governed by external forcing, and there is no interaction with the bed. Hydrodynamically, the coastal zone can be subdivided in three main regions, being deep, intermediate and shallow water. Deep water is generally defined as the region where the water depth is larger than half of the wave length ($\frac{1}{2}L \leq h$). Where the water depth is less than 1/20 of the wave length, we speak of shallow water ($\frac{1}{20}L \geq h$), and the region in between is referred to as intermediate ($\frac{1}{20}L \leq h \leq \frac{1}{2}L$).

As the waves propagate from deep water towards the shore and the water depth decreases, the dynamics are affected by interaction with the bed as soon as they reach intermediate water depth. From this point, where the waves start to interact with the bed, up to the point where the waves rush up and down the beachface is referred to as the nearshore region, and can be subdivided into a number of zones (see Figure 2.1).

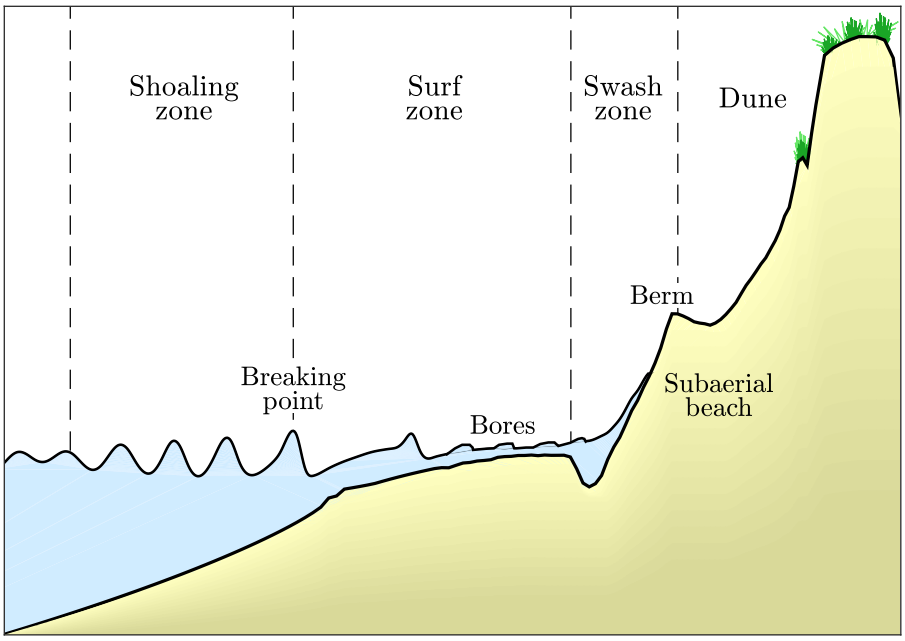

Figure 2.1: Definition of various zones within the nearshore coastal region.

In the shoaling zone, the waves start to feel the bottom, and waves tend to become steeper and higher, and potentially change direction, depending on the geometry of the bed and their angle of incidence. When waves become too steep or reach a bar, they start to break and their height decreases again, which is referred to as their breaking point. The energy of the broken waves is dissipated progressively as they propagate further onshore as bores through the surf zone. Wave transformation is discussed more in depth in Section 2.4.

Finally waves reach the shoreline, where they run up and down the beachface. This highly dynamic part of the beach is intermittently covered by the wave runup and is referred to as the swash zone. The morphodynamics of the swash zone (discussed in detail in Section 2.5) are of major importance for beach recovery as they distribute sediment over the subaerial beach (dry beach). Beyond the swash zone, aeolian (wind-driven) processes reshape the dry beach and dunes. This is beyond the scope of the present study and will not be discussed further.

2.3 Wave generation and propagation

Offshore, waves are generated during storm events and propagate onshore, where they reach the coast as swell. The propagation speed of a wave is dependent on the wave period and water depth through the dispersion relation:

$$\omega^2 = g\,k\,\tanh(k\,h) \tag{2.1}$$

Where ω is the frequency, k the wave number and h the water depth. This relation can be rewritten in order to derive an expression for the phase speed:

$$c^2 = \frac{g}{k}\,\tanh(k\,h) \tag{2.2}$$

Directional and frequency dispersion cause waves with similar frequencies to travel together from deep to shallow water. This ensemble of usually 6 to 7 waves travelling in the same direction at approximately the same phase speed is referred to as a wave group (illustrated in Figure 2.2). Their propagation velocity is straightforwardly related to their length and period, which depend on the differences in wave number and frequency respectively:

$$c_g = \frac{L_{group}}{T_{group}} = \frac{\Delta\omega}{\Delta k} \tag{2.3}$$

With $\Delta\omega$ the frequency difference of the wave signals, and Δk the difference in wave number. When we take the limit of $\Delta\omega$ and Δk to zero, we end up with the derivative of omega, which can be solved analytically:

$$c_g = \frac{\partial\omega}{\partial k} = \underbrace{\frac{1}{2}\left(1 + \frac{2kh}{\sinh(2kh)}\right)}_{n}\underbrace{\sqrt{\frac{g}{k}\tanh(kh)}}_{c} \tag{2.4}$$

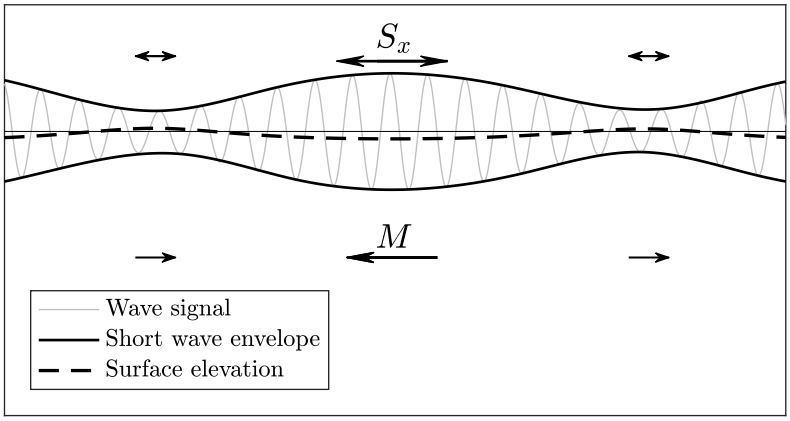

Figure 2.2: Illustration of a wave group, and the radiation stress-induced water level depression below the higher waves (modified from: Longuet-Higgins and Stewart, 1962).

From Equation 2.4 the expression for the phase speed of a single wave can be recognised (the dispersion relation, Equation 2.2). Hence n is the ratio between the wave group velocity and the phase speed, which varies from $\frac{1}{2}$ in deep water to 1 in shallow water.

The phenomenon of wave groups was first observed by Munk (1949) and later confirmed by Tucker (1950), who found a negative correlation between the water surface elevation and the short wave group envelope. Longuet-Higgins and Stewart (1962) later mathematically explained this negative correlation with their theory on radiation stress and mass transport. From the momentum balance (x component) they derived the following relation:

$$\frac{\partial \eta}{\partial t} = -\frac{1}{\rho\, g\, h}\,\frac{\partial S_{xx}}{\partial x} \tag{2.5}$$

Where η is the water surface elevation and S_x is the radiation stress, which was introduced by Longuet-Higgins and Stewart (1960). When vertical accelerations are neglected, and the waves are normally incident with respect to the coast, the expression for the radiation stress may be written as:

$$S_x = (2n - \tfrac{1}{2})\, E \tag{2.6}$$

With E the wave energy and n the ratio between the group velocity and the phase speed as defined in Equation 2.4. The radiation stress is a measure for the transfer of wave-induced momentum and, in a way, the stress can be considered to force the water apart, and hence cause a depression where the waves are largest, and an elevated surface where the waves are lowest. From conservation of momentum and mass also follows that the mean flow under the highest waves within the wave group is negative, and positive below the lowest waves (see Figure 2.2). For the full derivation and discussion on radiation stresses is referred to Longuet-Higgins and Stewart (1960, 1962).

2.4 Coastal hydrodynamics

2.4.1 Wave transformation and breaking

As waves propagate from deep into intermediate water depth, and start to be affected by the bed, they start to transform through various processes like shoaling, refraction, diffraction and eventually wave breaking. These processes are described below.

Shoaling
As a wave train, consisting of multiple waves, enters shallow water, the waves start to interact with the bottom and slow down. According to the linear dispersion relation (Equations 2.1 & 2.2), the propagation speed c decreases accordingly, while the frequency ω remains constant, hence causing the wave length L to decrease. As waves slow down, subsequent waves within the wave train start to catch up on the preceding ones and the wave energy becomes more concentrated, resulting in an increased wave height. This process is referred to as wave shoaling.

Refraction
When waves approach the coast at an angle with respect to the shore-normal direction (i.e. when waves are obliquely incident), the part of the wave crest that reaches shallow water first is

slowed down while the remainder of the wave crest is still in slightly deeper water and remains yet unaffected. This phenomenon is referred to as refraction and causes obliquely incident waves to bend towards normally incident as they travel through the shoaling zone to shallow water.

Diffraction
In presence of structures, abrupt bed geometry changes or other obstructions to the waves that approach the shore, a sudden variation in wave energy along the wave crest arises. This leads to a re-distribution of energy along the wave crest and causes waves to bend around e.g. structures or shoals. This process is referred to as wave diffraction.

Wave breaking
When a wave becomes too steep, it becomes unstable and starts breaking. Wave breaking can occur in deep water as well as in shallow water when the wave height becomes too large with respect to its length. Miche (1944) found the following expression for the limiting wave steepness at which waves start to break:

$$\frac{H}{L} = 0.142 \tanh(k\,h) \tag{2.7}$$

In deep water, the water depth does not affect the breaking mechanism and this breaker criterion reduces to $H_0 = 0.142\,L_0$. In shallow water, the breaker criterion is determined by water depth only, and the expression reduces to:

$$\frac{H}{L} = 0.142 \tanh(k\,h) \qquad = 0.142\,\frac{2\,\pi\,h}{L} \qquad \Rightarrow \qquad \frac{H_b}{h_b} \approx 0.88 \equiv \gamma_b \tag{2.8}$$

Where the subscript b denotes that wave breaking occurs, and γ_b is the breaker index. $\gamma_b = 0.88$ follows from linear wave theory, but other values are found using different theory and literature.

When the depth becomes too small, and waves become too steep, they start to break. It is in the breaker zone where they start to lose their energy. There are however various ways in which the waves can break, which depends on the geometry of the bed as well as on the wave characteristics. Galvin (1968) classified four different types of breaking waves, being spilling, plunging, collapsing and surging breakers (see Figure 2.3).

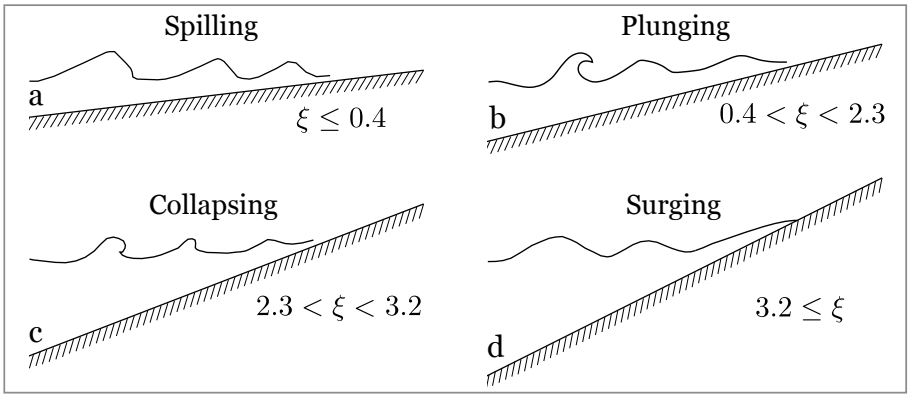

Figure 2.3: Different types of wave breaking (as identified by Galvin, 1968).

Battjes (1974) distinguished between the four types of wave breaking through a so-called "surf similarity" parameter ξ. This non-dimensional parameter (also known as the Iribarren number, Iribarren and Nogales, 1949) contains information on the wave steepness and the beach slope:

$$\xi = \frac{\beta}{\left(\frac{H}{L_0}\right)^{\frac{1}{2}}} \tag{2.9}$$

Where L_0 is the deep water wave height and β the beachface slope. Spilling breakers generally occur on relatively flat beaches ($\xi \leq 0.4$), where they break relatively far offshore and progressively dissipate their energy as they approach the beach. Plunging breakers are observed on a slightly steeper beachface ($0.4 < \xi < 2.3$). Surging breakers are found on steep beaches ($3.2 < \xi$), where waves surge up and down the beachface and most of the energy is reflected back offshore. Finally, collapsing breakers are found somewhere in between plunging and surging breakers ($0.4 < \xi < 2.3$).

2.4.2 Wave non-linearity

As the waves get closer to the shore, they become more and more non-linear until the point where they start to break. Besides an increasing wave height, the wave shape also changes in two ways. Firstly the wave crests become more peaked while the troughs become flatter, called wave skewness (asymmetric with respect to the horizontal axis). Wave skewness can be seen as the superposition of a primary and a secondary wave signal (with twice the frequency of the primary signal) that are in phase. When both the peak and the trough of the primary signal coincide with the peak of the secondary signal, the wave crests become more peaked and the troughs become flatter, which is referred to as positive skewness. Inversely, a negative skewness corresponds to the case where the peak and the though of the primary signal coincide with the troughs of the secondary signal, resulting in flat peaks and lower troughs. An example of a positively skewed wave is illustrated in Figure 2.4 – left.

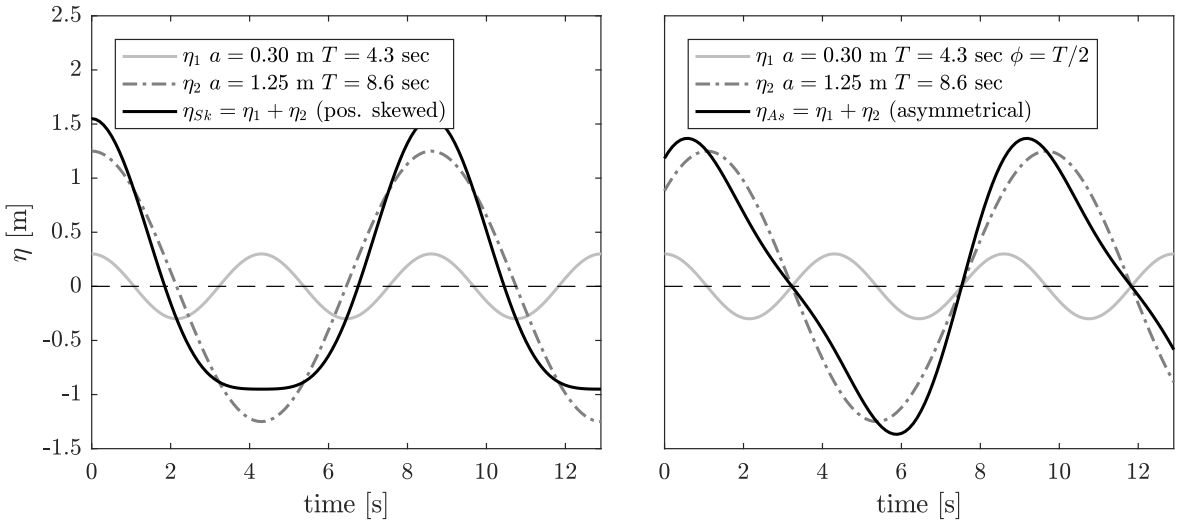

Figure 2.4: Illustration of wave skewness (left) and wave asymmetry (right) based on the superposition of two wave signals.

Secondly, as the waves propagate further onshore, they start to pitch forward and the face becomes steeper until the point of breaking, called wave asymmetry (asymmetric with respect to the vertical axis). In shallow water, the wave celerity is dependent on the water depth according to $c = \sqrt{g\,h}$. However, when the water depth becomes very small, and the wave amplitude becomes a significant fraction of the water depth, the wave height should be accounted for in a non-linear expression for the wave celerity:

$$c = \sqrt{g\,(h + \eta)} \tag{2.10}$$

From this relation it becomes clear that the wave crest propagates faster than the trough, and hence the waves start to pitch forward and become steeper. Wave asymmetry can be considered as the superposition of a primary signal and a secondary signal that is out of phase. Wave asymmetry is maximum when the secondary signal is 90^o out of phase, which concurs to the phase where wave skewness is no longer present.This is visualised in Figure 2.4 – right.

Initially, shoaling waves gradually become more skewed as they approach the shore and start interacting with the bottom. Closer to the surf zone, phase-shifting of the harmonics lead to an increase in wave asymmetry (cause the waves to pitch forward) and eventually a decrease in wave skewness (as this is only possible for harmonics that are in phase). Ultimately the pitching forward leads to wave breaking as the wave crest overtakes the trough, and the wave front becomes to steep.

2.4.3 Wave-induced setup and runup

Proper estimation of wave-induced setup and runup is of major importance in modelling swash morphodynamics and beach recovery. The maximum runup determines the horizontal (landward) and vertical extent to which sediment transport takes place, and hence where morphological changes occur.

Setup

Wave setup is defined as the time-averaged water level elevation at the shoreline and is driven by the cross-shore gradient in radiation stresses resulting from wave breaking (Longuet-Higgins and Stewart, 1962, 1964). Many studies have been dedicated to deriving the relationship between this wave-induced setup and environmental conditions. Assuming normally incident waves, with a wave height limited to a constant breaker index $\gamma_b = H/h$ throughout the surf zone, Bowen et al. (1968) derived a simplified expression for the setup at the shoreline:

$$\frac{\langle\eta\rangle}{H_b} = 0.38\gamma_b \tag{2.11}$$

With $\langle\eta\rangle$ the wave setup, H_b the breaking wave height and γ_b the breaker index. However, measurements showed that this expression underestimates the actual runup due to the asymptotic approach. Further research indicated that the setup at the shoreline is also affected by the surf zone topography (e.g. Holman and Sallenger Jr., 1985; Raubenheimer et al., 2001). An empirical formulation for the wave setup, taking into account the beach slope was proposed by Stockdon et al. (2006):

$$\langle\eta\rangle = 0.35\,\beta_f\,\sqrt{H_0\,L_0} \tag{2.12}$$

Where β_f is the foreshore slope, which is defined as the average slope over the region of the beachface between +/- 2 times the standard deviation of the water level record, around the mean setup level $\langle\eta\rangle$ (Stockdon et al., 2006).

Runup

The runup is defined as the height of the discrete water level maxima with respect to still water in absence of waves. The runup therefore depends on both the time-averaged wave setup and the total swash excursion S. Hunt (1959) derived an expression for the total runup, based on the deep-water wave height, wave period, and the beach steepness, expressed in the Iribarren number (Equation 2.9):

$$\frac{R}{H_0} = K\,\xi \tag{2.13}$$

Where R is the wave runup height, H_0 is the wave height in deep water and $K \approx 2.3$ a constant derived from a thorough analysis of experimental data (Hunt, 1959). Holman (1986) used field data to obtain a slightly different formulation, where the runup level is normalised by the significant wave height H_s:

$$\frac{R_2}{H_s} = 0.83\,\xi_0 + 0.2 \tag{2.14}$$

Here, ξ_0 includes the foreshore beach slope β_f and the deep water wave height. However, on natural beaches, the presence of sandbars strongly attenuates the offshore waves, hence the coefficients in Equation 2.14 are highly dependent on the site-specific bathymetry.

On morphodynamically different beaches, the relative contribution of the incident and infragravity band swash to the total swash varies (Guza and Thornton, 1982). Nielsen and Hanslow (1991) verified Equation 2.14 on a range of morphodynamic beach states, and found that while the runup was proportional to the Iribarren number for reflective beaches, the inclusion of the beach slope became less important for more dissipative beaches. Hanslow and Nielsen (1993) also stated that the runup on a dissipative beach was found to be independent of the beach slope. Stockdon et al. (2006) built upon the expression by Holman (1986), and parametrised the incident swash S_{inc} and infragravity swash S_{IG} separately as follows:

$$S_{inc} = 0.75\,\beta_f\,\sqrt{H_0\,L_0} \tag{2.15}$$

$$S_{IG} = 0.06\,\sqrt{H_0\,L_0} \tag{2.16}$$

To encompass the entire range of morphodynamic beach states, Stockdon et al. (2006) combined these two expressions into one to describe the total swash excursion:

$$S = \sqrt{0.563\,\beta_f^2 + 0.004}\,\sqrt{H_0\,L_0} \tag{2.17}$$

Finally, the total (2% exceedance) runup height $R_{2\%}$ is a function of the time-average wave setup at the shoreline and the total swash excursion (Stockdon et al., 2006):

$$R_{2\%} = 1.1\,\left(\langle\eta\rangle + \frac{S}{2}\right) \tag{2.18}$$

2.5 Swash zone morphodynamics

The swash zone is the highly dynamic part of the beach between the point where the bores collapse on the beachface and the maximum uprush limit (Hughes and Turner, 1999). In contrast to waves in the surf zone, and further offshore, which obey a certain relation between the wave length, peak period and wave height, the motions in the swash zone are much more dynamic and irregular. The period, or duration of a swash cycle (i.e. the time from the onset of the uprush until the end of the backwash), and the maximum run-up on the beachface are not simply related to offshore conditions, and are not constant under constant (nearshore) conditions. Due to its high variability, turbulent nature and the complex interactions within the swash zone, a measured swash event (in terms of duration and elevation) is not representative for a series of swash motions under the same wave conditions (Masselink and Puleo, 2006).

2.5.1 Hydrodynamics

Within a swash cycle, four stages can be distinguished (see Figure 2.5). Initially, when there is no wave motion in the swash zone, a bore is approaching the lower end of the swash zone. When the bore breaks on the shoreface, the uprush is rapidly accelerated (top left). As the uprush propagates up-slope, it decelerates quickly, and at the maximum uprush of the leading edge, the lower end of the up-rushing water is already moving seaward as backwash, causing a thinning of the swash lens (top right). As a consequence of the hydraulic head difference, a part of the flow infiltrates the beach as well, further enhancing the thinning of the wash lens. Subsequently, the flow reverses and the backwash gradually accelerates due to gravity (bottom left). During backwash, exfiltration through the surface may occur, and as the leading edge of the backwash (the seaward end) starts colliding with the next bore, the backwash decelerates (bottom right), potentially leading to the formation of a retrogressive bore (Masselink and Puleo, 2006).

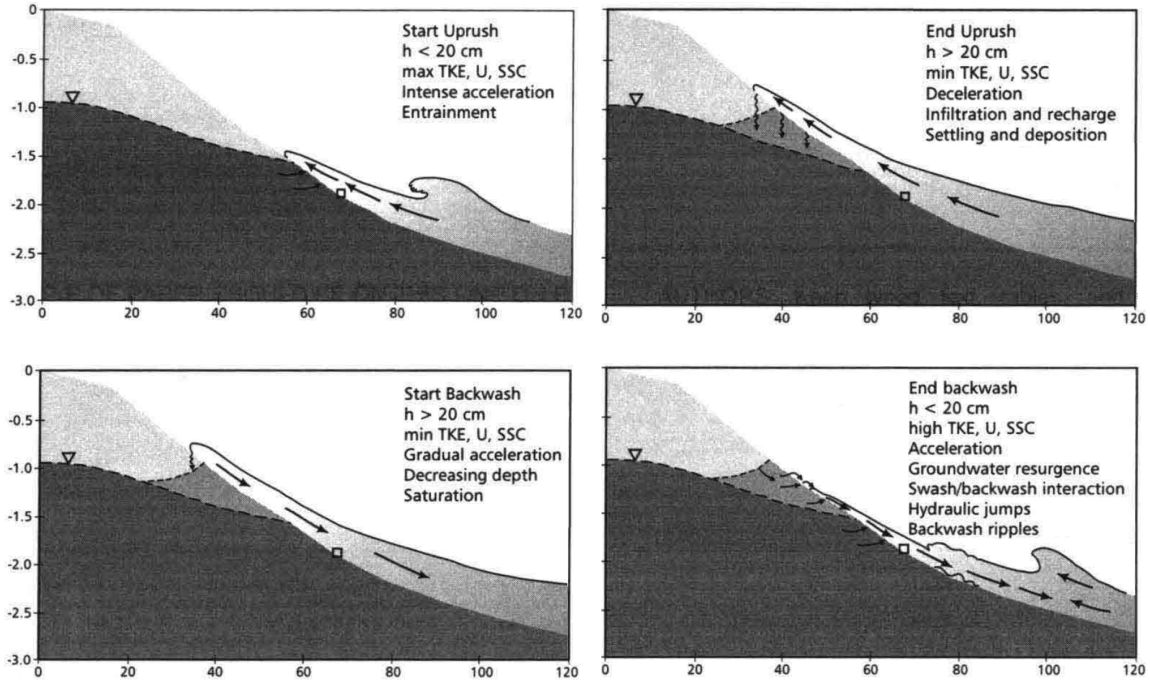

Figure 2.5: Illustration of the four stages of a swash cycle (from: Osborne and Rooker, 1997)

There is a clear difference between the hydrodynamics of the uprush and the backwash. Since the flow instantaneously accelerates at the onset of the uprush, and quickly decelerates as it propagates up-slope, the maximum uprush velocity is found at the start of the uprush. The acceleration of the backwash is much more gradual, and therefore the maximum velocity is found at the end of the backwash in the lower swash zone. The uprush duration is significantly shorter than the backwash, and peak uprush velocities are generally found to be slightly higher than backwash velocities (e.g. Hughes and Baldock, 2004).

This asymmetry in swash flow affects the gradient of the beachface (Bagnold, 1940), and a balance between the onshore (upward) swash asymmetry and the offshore (downward) gravity component yields a dynamic equilibrium of beachface (Hardisty, 1986). Hence, this asymmetry in the swash hydrodynamics is also translated to the morphological response, as discussed in the next section.

2.5.2 Sediment transport

Depending of the hydrodynamic conditions, sediment transport may occur in different modes. The main two modes are suspended sediment transport and bed load transport, but different sub-categories can also be distinguished. Wash load, for example, is a form of suspended transport that consists of very fine particles that are kept in suspension by molecular interaction rather than turbulence. Sheet flow sediment transport can be considered as bed load transport, occurring when a clear bed form is absent.

As a consequence of the highly dynamic water motion in the swash zone (as discussed in Section 2.5.1), the sediment transport is observed to occur in various modes. At the start of the uprush, bore-generated turbulence directly enhances sediment suspension, resulting in a high Suspended Sediment Concentration (SSC), nearly vertically uniform over the water column, concentrated in the leading edge of the uprush (Puleo et al., 2000). This suggests that suspended sediment transport is the dominant mode during uprush, but a rapid increase in bed shear stresses after the collapsing of the bore on the beachface also initiates sheet flow bed transport (Masselink and Puleo, 2006). Under the influence of gravity and bed shear, the uprush quickly decelerates, allowing the sediment to settle to the bottom and leaving the water clear at the time of flow reversal.

As discussed in Section 2.5.1, by the time the uprush has reached its most landward extent, the lower part of the flow has already returned offshore as backwash, resulting in a thinning of the swash lens (Figure 2.5 – top right). Adding to this, in- and exfiltration also affects the thickness of the uprush and backwash. After flow reversal, the backwash gradually accelerates, and therefore the maximum sediment suspension occurs at the end of the backwash. Although the backwash is less turbulent than the uprush, super-critical flow conditions may occur due to the thinning and accelerating flow at the end of the backwash (Osborne and Rooker, 1999). Observations show that the sediment suspension during backwash is mostly confined close to the bed, where strong vertical gradients in SSC exist (Puleo et al., 2000). This makes the dominant sediment transport mode during backwash bedload under sheet flow conditions, with suspended sediment transport also being important (Masselink and Puleo, 2006).

Baldock et al. (1997) found that swash motions can be described in two modes, being the individual bore collapsing on the beachface, and the wave group forcing, acting as standing waves. The dominant mode depends on the wave conditions, and the beach morphology, and can be determined with the surf-similarity parameter ξ (Guza and Inman, 1975)

2.5.3 Key swash zone processes

The swash motion on the beachface provides the principal mechanism for the exchange of sediment between the subaqueous and the subaerial part of the beach (Masselink and Hughes, 1998). The physical processes in the swash zone that are most important for the (net) onshore transport of sediment, and vertical growth of the berm are summarised in the present section.

Bore turbulence
Field measurements of swash zone processes indicated that bore-generated turbulence directly enhances sediment suspension (Puleo et al., 2000), and strong cross-shore gradients in SSC suggest that bore-derived turbulence may affect local sediment transport. Hsu and Raubenheimer (2006) also argued that their observations suggest that surface-generated turbulence at the breaking wave front penetrates to near the bed, and affects the onshore-directed sediment transport in the swash zone.

Settling and scour lag
During the uprush, there is a lag of the actual settlement of a particle to the bottom with respect to the deceleration of the uprush. This so-called settling lag – the time it takes for a particle to settle to the bed – provides the possibility for sediment to be transported higher up the beachface. During backwash, the flow accelerates more gradually, and hence the backwash needs more time to reach a velocity that ensures the entrainment of sediment. This lag in sediment entrainment with respect to the time of flow reversal is referred to as scour lag. Due to this combination of settling lag and scour lag, the (larger) particles that are deposited in the upper swash zone, can never be mobilised during backwash.

Onshore sediment transport might also be enhanced by the phase lags between the flow forcing and bed shear stresses (Hsu and Raubenheimer, 2006).

Infiltration and exfiltration
Turner and Masselink (1998) found that swash infiltration and exfiltration enhances the net up-slope sediment transport, by performing field measurements. The seepage forces exerted on the surface affect the effective weight of the sediment, and hence abate or enhance sediment mobilisation. Additionally, in- and exfiltration also causes a thinning or thickening of the boundary layer, which directly influences the velocity gradient, and hence the bed shear stress.

During uprush, the drag force on the particles due to infiltration stabilises the sediment, but on the other hand, the thinning of the boundary layer, and the associated higher velocity gradient exerts a larger shear stress on the bed. Reversely, the exfiltration during backwash makes the sediment more vulnerable to mobilisation, but the thickening of the boundary layer, and hence smaller velocity gradient weakens the shear stress.

Sediment advection
Masselink and Puleo (2006) state that the sediment transport asymmetry in the swash zone is strongly affected by sediment advection. Hence, the supply of suspended sediment from the surf zone might be of major importance for morphological changes in the swash zone. However, only very few field or laboratory experiments are performed to study this process, and knowledge on the role of sediment advection is very limited.

2.6 Morphodynamic beach states

Wright et al. (1979) were the first to distinguish the two extreme beach states based on morphodynamic as well as hydrodynamic features, being dissipative and reflective. Based on this work, Wright and Short (1984) developed the widely accepted concept of morphodynamic beach states, to imply the complete assemblages of depositional forms and coupled hydrodynamic process signatures. They identified six morphological beach states based on various observational studies. In between the dissipative and reflective extremes, identified by Wright et al. (1979), they classified four intermediate beach states.

The dissipative beach state is characterised by high-energy and long-period waves that break by spilling, and dissipate progressively as they cross the surf zone. Dissipative beaches have a wide surf zone with a low shore normal gradient, and little alongshore variations are typically present. As the incident wave energy is progressively dissipated towards the coast, the infragravity-related flow velocity increases, and dominates in the surf and swash zone (Wright et al., 1985). A typical dissipative beach profile is schematised in Figure 2.6 – left.

On the other end, reflective beaches are characterised by lower-energy waves that either surge or collapse on the steep beachface. The morphology of reflective beaches is dominated by incident waves, and wave breaking turbulence is confined to the upper swash zone. Infragravity waves mostly reflect, and hence their energy is considered to be negligible on reflective beaches, whereas incident waves run up high upon the beachface and dominate the surf (and swash) zone (Wright et al., 1979). A typical reflective beach profile is schematised in Figure 2.6 – right.

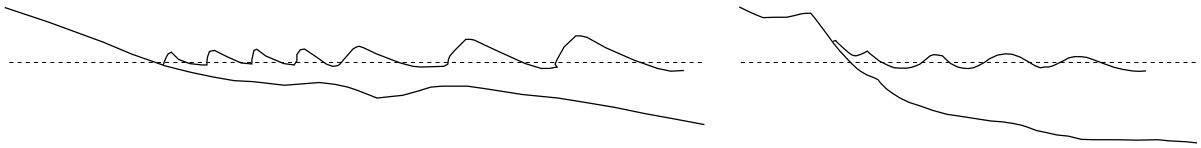

Figure 2.6: Schematisation of a dissipative (left) and reflective (right) beach profile.

From dissipative to reflective, the first intermediate morphodynamic beach state is Longshore Bar-Trough (LBT), still nearly alongshore constant. Next, the Rhythmic Bar-Beach (RBB) and Transverse Bar-Rip (TBR) both show significant alongshore variation in morphology and hydrodynamics. Finally, at the reflective end of the intermediate regime, Ridge-Runnel (RR) or Low-Tide Terrace (LTT) is again much more alongshore uniform. Typical plan views and profiles of the intermediate beach stages are illustrated in Figures 2.7 - 2.10 (modified from Wright and Short, 1984).

Figures 2.7 - 2.10 show that the profiles change considerably from dissipative to reflective, from wide and and mildly sloping to narrow and steep respectively. Furthermore the type of wave breaking changes with morphodynamic beach state, from spilling breakers in the dissipative extreme (Figure 2.6 – left) to surging in the reflective regime (Figure 2.6 – right). On intermediate beaches spilling, plunging, collapsing and surging breakers may all occur, depending on the alongshore position and the tide.

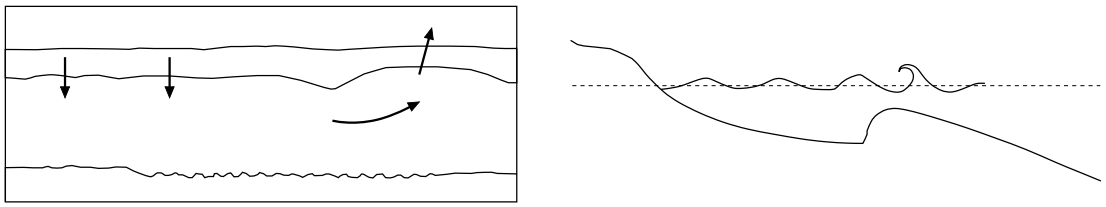

Figure 2.7: Schematisation of a Longshore Bar-Trough (LBT) beach profile. The plan view on the left hand side to visualise the (weak) 2D flow patterns.

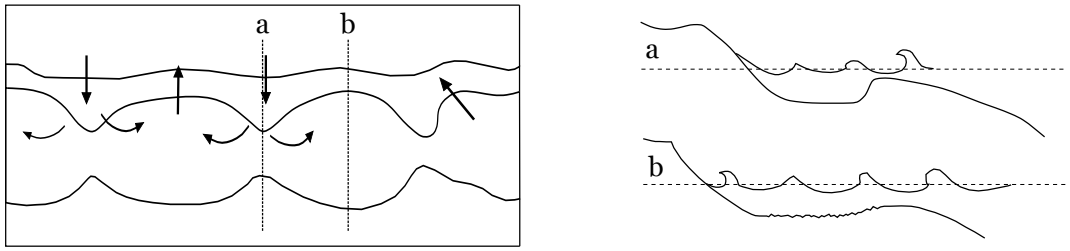

Figure 2.8: Schematisation of a Rhythmic Bar-Beach (RBB) beach profile. The plan view indicates the cross sections of a) the trough and b) the location of the rip.

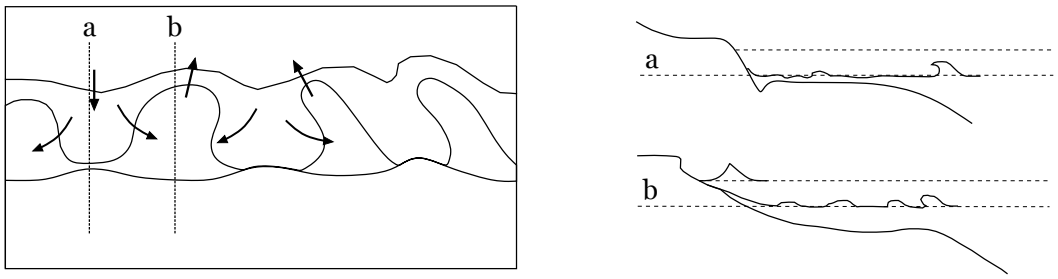

Figure 2.9: Schematisation of a Transverse Bar-Rip (TBR) beach profile. The plan on the left hand side indicates the cross sections of a) the transverse bar and b) the rip.

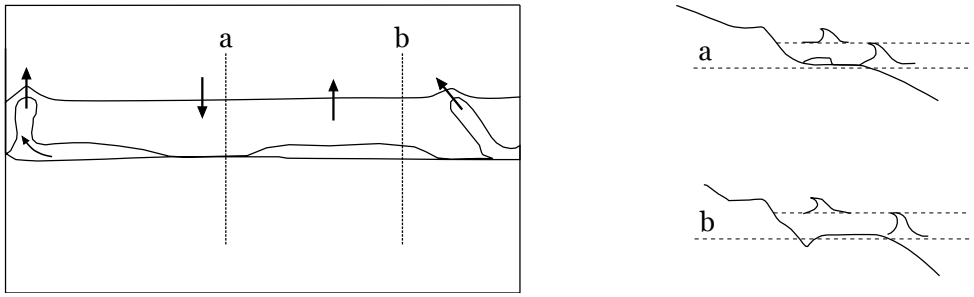

Figure 2.10: Schematisation of a Low-Tide Terrace (LTT) or Ridge-Runnel (RR) beach profile. A plan view is provided on the left hand side to visualise the locations of the cross sections, displayed in the right figure, with a) the LTT and b) the RR.

To take into account the profile shape and the type of wave breaking, the two extremes are distinguished based on the surf-similarity parameter (Guza and Inman, 1975):

$$\epsilon = \frac{a_b\,\omega^2}{g\,\tan^2(\beta)} \tag{2.19}$$

Which considers the wave conditions by means of the breaker amplitude a_b and wave frequency ω, as well as the steepness of the beachface β. Reflective behaviour (e.g. standing wave patterns, surging and resonance) is expected when $\epsilon \leq 1 - 2.5$ (Guza and Inman, 1975; Guza and Bowen, 1977), and the swash is dominated by incident wave bores. When $\epsilon > 2.5$ waves begin to plunge and dissipate energy, and when $\epsilon > 20$ spilling breakers occur (Galvin, 1972). This indicates the dissipative regime, where the swash is characterised by standing long wave motions and the runup is dominated by energy from the infragravity band frequency (Ruessink et al., 1998). Generally, as the value of ϵ increases the surf zone becomes wider and turbulent dissipation of incident wave energy increases (Wright and Short, 1984).

Several studies pointed out that the morphological beach state is also dependent on the sediment characteristics. On dissipative beaches, there is an abundance of fine material whereas reflective beaches consist of relatively coarse sediment. To include the sediment characteristics in their conceptual model of morphodynamic beach states, Wright and Short (1984) used a dimensionless fall velocity Ω (Dean, 1973) for the classification:

$$\Omega = \frac{H_b}{\bar{w_s}\,T} \tag{2.20}$$

Where H_b is the breaker height, $\bar{w_s}$ the fall velocity and T the wave period. Here, low values ($\Omega \leq 1$) correspond to the reflective regime, and $\Omega \geq 6$ defines the dissipative extreme. They argue that an equilibrium profile should exist for a certain set of conditions, and that deviation from this equilibrium enhances morphological changes.

Later, Wright et al. (1985) therefore defined a weighted mean dimensionless fall velocity $\bar{\bar{\Omega}}$ which is calculated based on the (recently) antecedent instantaneous values for Ω:

$$\bar{\bar{\Omega}} = \frac{\sum_{i=1}^{D} \Omega_i \cdot 10^{-i/\phi}}{\sum_{i=1}^{D} 10^{-i/\phi}} \tag{2.21}$$

Where i is the number of days prior to the observation, D the number of days considered to determine the weighted mean and ϕ [days] a measure for the rate of memory decay of the system. $\bar{\bar{\Omega}}$ can therefore be considered as a time-varying equilibrium fall velocity, taking into account antecedent wave and morphology conditions.

Wright and Short (1984) argue the rate of change in beach state depends on the degree of deviation from the equilibrium wave conditions, as well as the wave energy that is available. Morphological change is dependent on antecedent wave conditions (beach state) during calm, reflective conditions (Lippmann and Holman, 1990). However, during energetic conditions the prevailing wave conditions determine the change in beach state (Short and Aagaard, 1993).

2.7 Coastal modelling

Knowledge of the impacts of environmental conditions on the coastline is of fundamental importance for coastal managers. Much research is devoted to gain a better understanding of the physical processes that drive shoreline change, and a wide range of numerical coastal models have been developed to predict the morphological response of coasts to storm events.

Numerical models that are developed to simulate coastal morphodynamics can generally be categorised into three main types, being coastline models, profile models and area models (Roelvink and Reniers, 2012). Coastline models (e.g. Bosboom et al., 1997; Davidson et al., 2013) assume an alongshore uniform cross-shore profile, and hence expresses morphological change in coastline retreat or progradation. Profile models (e.g. Larson and Kraus, 1989) calculate the cross-shore processes and profile change, and aerial models (e.g. Roelvink et al., 2009) compute 2D processes and bed level changes.

There are different approaches to apply these types of models. Process-based models (e.g. XBeach, Roelvink et al., 2009) aim to describe the processes through solving momentum and mass balance equations. Empirical models (e.g. Kriebel and Dean, 1993) describe morphological change based on empirical relations derived from field and/or laboratory measurements. Equilibrium models (e.g. Davidson et al., 2013; Splinter et al., 2014) relate coastline change to deviations from a certain equilibrium.

2.7.1 Equilibrium models

The potential magnitude of shoreline change is influenced by the incident wave power and the degree of disequilibrium. Davidson et al. (2013) defined this degree of disequilibrium as deviation of the instantaneous dimensionless fall velocity Ω for the time-evolving equilibrium dimensionless fall velocity $\bar{\bar{\Omega}}$ (as defined by Wright et al., 1985, see Equation 2.21).

$$\Delta\Omega = \bar{\bar{\Omega}} - \Omega \tag{2.22}$$

The degree of disequilibrium $\Delta\Omega$ dictates the direction and magnitude of the change of shoreline position.Splinter et al. (2014) also used the approach of Davidson et al. (2013) to validate their equilibrium model on 12 sites, and found a high performance of the model (BSS = 0.85).

2.7.2 Empirical models

Bagnold (1962) introduced the energetics-based approach for modelling sediment transport in the swash zone. He proposed a model that related the sediment transport over a swash event to the fluid power ω. Initially he only considered the bed transport, but later he expanded the formula to also account for suspended sediment.

$$I_b = \frac{\varepsilon_b \, \omega}{\tan(\phi) - \tan(\beta)} \tag{2.23}$$

Where ε_b is a calibration factor. Butt et al. (2005) performed field measurements and compared the observations with the energetics model, originally described by Bagnold (1962, 1966). They expressed the fluid power ω as the product of the bed shear stress and the velocity. Since the

bed shear stress is proportional to the velocity squared, the fluid power is proportional to the velocity cubed:

$$I_b = \frac{\frac{1}{2}\,\varepsilon_b\,\rho\,c_f\,u^2\,|u|}{\tan(\phi) - \tan(\beta)} \tag{2.24}$$

Butt et al. (2005) concluded that for steep beaches, the Bagnold-type model performs less well compared to gently sloping beaches. They suggest that this can be attributed to the fact that bore-turbulence plays an important role on steeper beaches, which is not included in this model. The study suggests that a Bagnold-type model would need to be modified in order to account for extra processes like bore turbulence, which is particularly apparent on steep beaches. Puleo et al. (2000) found a higher correlation between bore-generated turbulence and suspended sediment transport than a Bagnold-type formulation and suspended sediment transport, and question the validity of sediment transport models in the vicinity of the bore.

Also Hughes et al. (1997) compared the Bagnold-type model to observations, and found $\mathrm{r}^2 = 0.78$ for a steep beach. They used a bedload transport model for the swash zone proposed by Hardisty et al. (1984), which was based on the Bagnold model:

$$I_b = \frac{k\bar{u}^3 T_u}{\tan(\phi) + \tan(\beta)} \tag{2.25}$$

Where I_b is the immersed weight of the bedload transported during the uprush, $k = 1.37 \pm 0.17$ is a coefficient [kg $\mathrm{m}^{-4}\mathrm{s}^2$], $\bar{u}$ the time-averaged uprush velocity, T_u the uprush duration, ϕ the internal angle of friction of the sediment and β the beach slope.

2.7.3 Conceptual beach recovery models

Baldock et al. (2007) argue that extensive swash overtopping of a low beach berm was associated with rapid berm aggradation (i.e. vertical growth), but with little horizontal progradation of the beachface, and no significant profile steepening of flattening. The rapid accretion of the berm crest could be considered as a sediment sink, which was supplied by the surf zone. Hence, the surf zone was functioning as a sediment source.

Masselink and Short (1993) studied the effect of the tide range on the morphodynamics of the beach, and found a correlation between beach state and the Relative Tide Range (RTR). Weir et al. (2006) also recognised the importance of the phase within a tidal cycle in the development of their conceptual model for the cross-shore distribution of sediment transport. They documented two different modes of berm development, being vertical growth due to wave overtopping and horizontal growth due to the formation of a neap berm further seaward of the principal berm. Phillips (2018) later also concluded that the spring-neap tidal cycle plays an important role in the recovery process after a storm impact, and the various modes in which this happens.

Weir et al. (2006) derived sediment transport shape functions, which were relations between the normalised sediment transport rate and normalised swash height (relative to the maximum transport rate and runup height, respectively). Larson and Kraus (1995) derived a cross-shore distribution function for the sediment transport as function of this normalised swash height:

$$\frac{q}{q_s} = \left(1 - \frac{\Delta h}{R}\right)^{3/2} \frac{\tan(\beta)}{\tan(\beta_s)} \tag{2.26}$$

Beach slope

Many conceptual models and empirical formulations relate processes (e.g. runup height, sediment transport, type of wave breaking) to the beach slope. The beach slope depends on the wave conditions (Wright and Short, 1984; Wright et al., 1985), grain size (Bagnold, 1940), sediment sorting and rate of percolation (Komar, 1976) and heavy mineral content (Dubois, 1972). The beach slope is affected by motions in the swash zone as well as the surf zone (Wright et al., 1982), and may vary with the spring-neap tidal cycle (Masselink and Short, 1993; Weir et al., 2006; Phillips, 2018).

While on dissipative beaches, the beach slope is more or less constant throughout the surf zone, on intermediate and reflective beaches there is a significant cross-shore variability in beach gradient. The definition of the beach slope is therefore, in contrast to in a laboratory setup, not straight-forward. Bascom (1951) for example defined the beach slope as the gradient around the mid-tide level, while Dubois (1972) considers the part of the beach from the lower limit of the backwash to the upper limit of the uprush. Inconsistencies with respect to the definition of the beach slope should be taken into consideration when interpreting field investigations (Masselink and Puleo, 2006).

Chapter 3

Study site – Narrabeen Beach

3.1 Introduction

The present chapter provides a description of Narrabeen Beach, and more specifically an analysis of the recovery of Narrabeen Beach following a storm that struck the coast in April 2015. A description of the study site and its environmental conditions is presented in Section 3.2. The extensive monitoring that is carried out at Narrabeen Beach during the past 4 decades is briefly discussed in Section 3.3, highlighting the implications and importance of the dataset. Next, the beach recovery process following the April 2015 storm event is analysed in Section 3.4. Finally, a brief literature review on conceptual models for beach recovery is discussed in Section 2.7.3.

3.2 Site description

The south-eastern coast of Australia consists of over 700 relatively short sandy beaches with an average length of ~1.3 km, separated by rocky headlands (Short, 2007). Narrabeen Beach is a 3.6 km long coastal embayment, situated approximately 20 km north of Sydney (see Figure 3.1), and refers to the stretch of sandy beach between the Narrabeen head (north) and Fisherman's Beach (south). Near the northern end of the beach, a lagoon behind the beach is connected to the sea via a small (approximately 50 m-wide) intermittently opening inlet (Morris and Turner, 2010), also referred to as an Intermittently Opening and Closing Lagoon (ICOL). Along the entire beach, the sediments consist of fine to medium quartz sand ($D_{50} \simeq 0.3$ mm) with ~30 % carbonate fragments. Since there is only minimal sediment exchange between Narrabeen beach, the lagoon and adjacent beaches, the sediment contained within the embayment can be considered a closed system (Harley et al., 2011a).

The Narrabeen coastline, and its surrounding region, is classified as a wave-dominated coastline (Short, 2007) and experiences semi diurnal, micro-tidal conditions with a mean spring tidal range of 1.25 m (Short, 1984). The region is classified as an East Coast Swell environment (Davies, 1973), characterised by long-period ($T_p \simeq$10 s) swell waves form the south south-east (SSE) and a mean significant wave height of $H_s \simeq 1.6$ m (Short and Trenaman, 1992).

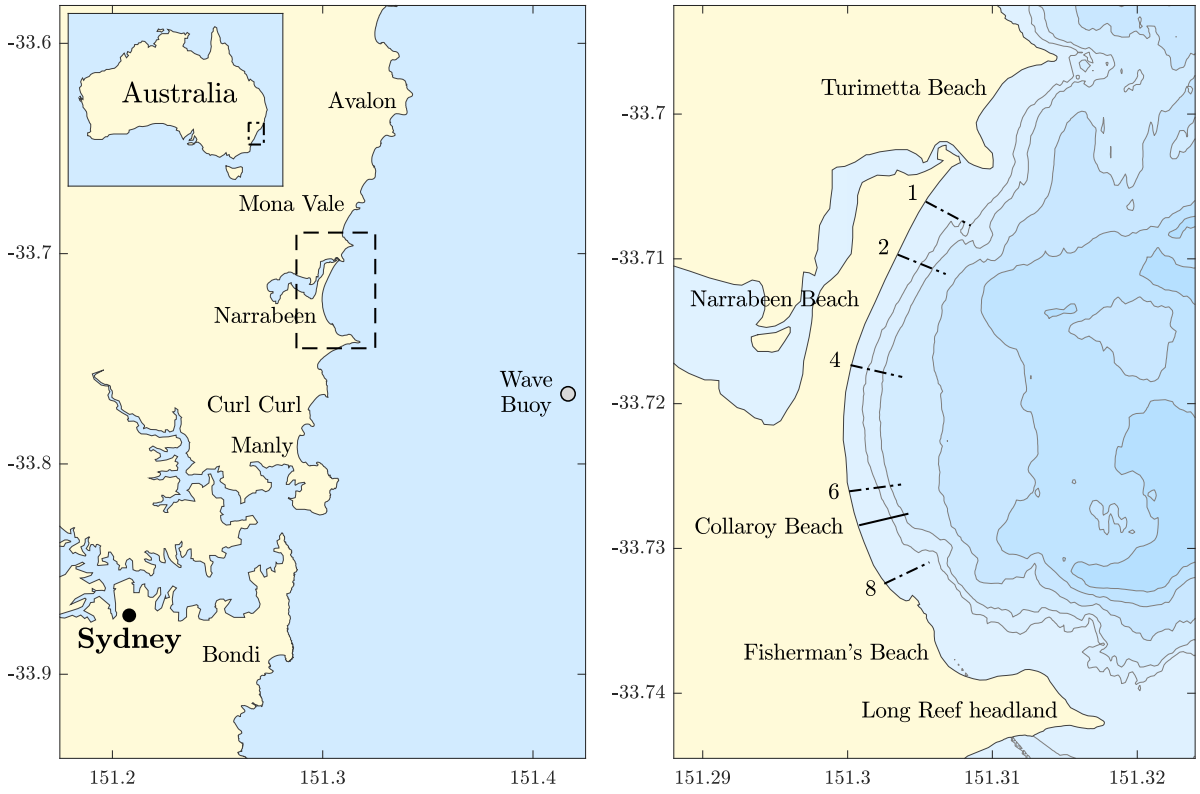

Figure 3.1: Location of Narrabeen Beach (left), with the 5 cross-sections indicated with the dashed-dotted lines, and the Lidar-measured transect indicated by the solid line (right).

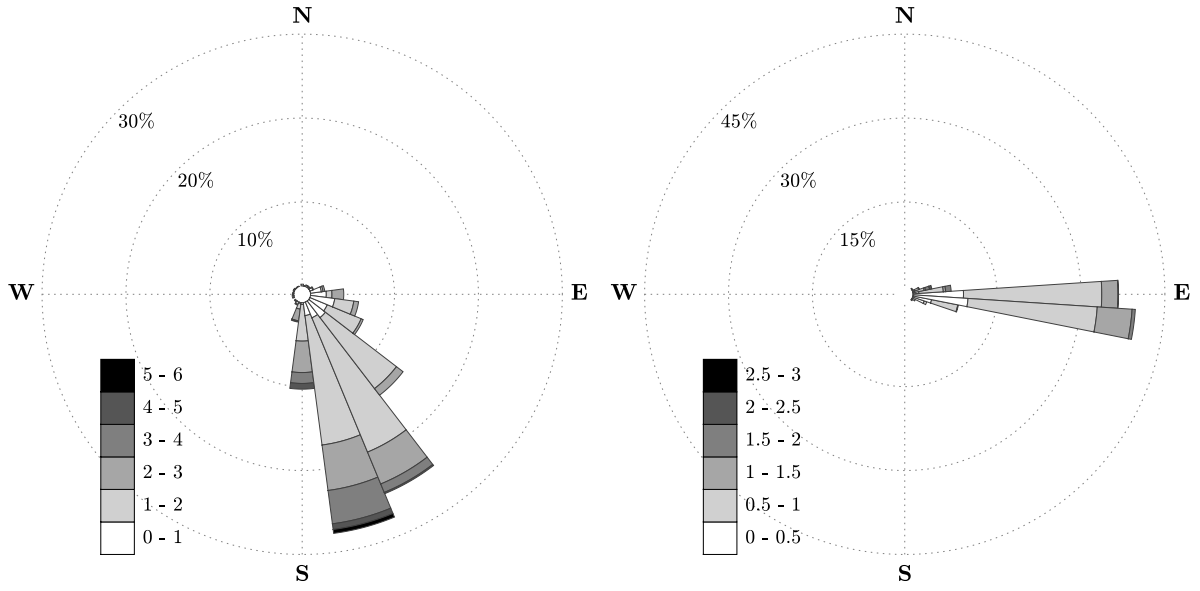

Figure 3.2: Offshore significant wave height and direction (left), obtained from the wave buoy measurements (see Figure 3.1 – left) and calculated nearshore wave height and direction at the 20 m depth contour (right), using the wave transformation model MIKE21 (DHI, 2014).

Superimposed on the swell are offshore generated storms, derived from different sources and directions. A storm event the considered region is generally defined as the period in which the offshore significant wave height exceeds the threshold of 3 m, which corresponds to an exceedance of 5% (Harley et al., 2010). Tropical cyclones are formed in the coral sea, and reach the region from the north-east typically during the summer months (Short and Trenaman, 1992). From the south, intensified extra-tropical cyclones are formed and East Coast Lows (ECLs) origin from the east. ECLs usually occur during Austral winter months and are the most damaging events (e.g. Harley et al., 2016, 2017), which can lead to offshore significant wave heights that exceed 8 m (Shand et al., 2011).

The curvature of the embayment, and the presence of headlands north and south of the beach causes sheltering and induces alongshore gradients in nearshore wave exposure (Harley et al., 2011a, 2015). Especially the Long Reef headland at the southern end of the embayment provides a significant degree of sheltering from incoming wave energy. The offshore wave height of 1.6 m translates to a nearshore wave height of 1.1 m in the north and 0.8 m in the south of the Narrabeen embayment. As a consequence, the beach morphology state (as defined by Wright and Short, 1984, see Section 2.6) also varies along the coast from more dissipative towards the north to more reflective in the more sheltered southern end.

3.3 The Narrabeen dataset

3.3.1 Monitoring

At Narrabeen, an extensive monitoring program has been carried out since 1976 (Turner et al., 2016). During the first few years, the monitoring program comprised of 14 cross-shore profile surveys using the Emery method (Emery, 1961) – a simple but labour-intensive method using poles and tape. Later it was decided to focus on five representative cross-shore profiles in order to make a monthly survey more feasible and efficient. The locations of these five representative cross-shore transects are indicated in Figure 3.1 – right (dashed-dotted lines), where the labelling corresponds to the original profile numbering. In 2004, RTK-GPS technology was introduced and extensively validated during a period of 16 months (Harley et al., 2011b) before it completely replaced the original Emery method in May 2005.

In early 2004 an Argus coastal imaging station (Holman and Stanley, 2007) was installed on top of an appartment building in the southern region of the embayment (solid black line in Figure 3.1 – right), capturing hourly images of the swash and surf zone. The Argus camera captures images of the the minimum and maximum shoreward extent of the swash edge, as well as timex (20 minute averaged) images, during day times. Since 2011, a total of 17 hydrographic surveys have been carried out, using a variety of methods (e.g. jetski- and boat-mounted measurement systems), to complement the historical subaerial profiles with the subaqueous bathymetry.

The monitoring program at Narrabeen further expanded when a fixed scanning Lidar was installed on the rooftop of the same beach side apartment building as the Argus coastal imaging station in 2014. An illustration of the Lidar setup is presented in Figure 3.3. Ever since its deployment, it is continuously scanning the beach transect (see Figure 3.1 – right, solid black line, for the transect) at a high frequency (5 Hz). The Lidar measures the subaerial beach profile at angular increments of 0.25 degrees, corresponding to spatial resolution ranging from of 0.2 m (on top of the berm) to 2 m (in the surf zone), and has a maximum range of approximately 130 meters (Phillips, 2018).

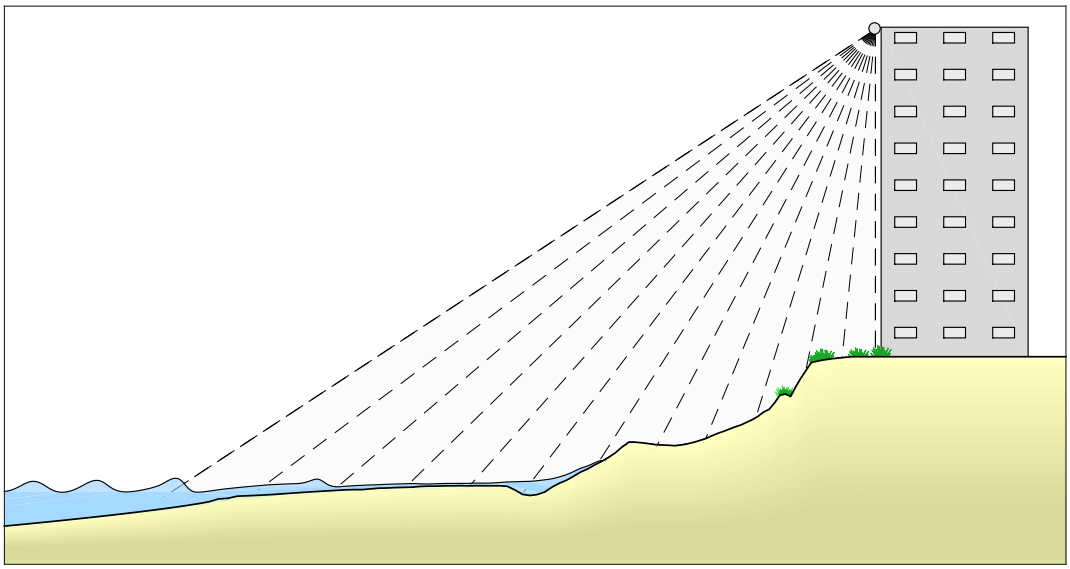

Figure 3.3: Setup of the continuously scanning Lidar at the rooftop of a 44-m high building aside the beach (see Figure 3.1 for the alongshore position).

3.3.2 Waves and tides

Approximately 11 km offshore, the Sydney waverider buoy records the hourly wave characteristics in a water depth of 80 m (see Figure 3.1 – left). Since 1992, measurements of the offshore significant wave height H_S, peak period T_p and wave direction θ_0 are collected and publicly available. The offshore wave data have been transformed to nearshore wave data by means of a lookup table. This lookup table was constructed based on 1573 model runs for a wide range of combinations of H_S, T_p and θ_0, using the wave model SWAN (Booij et al., 1999). To complement the offshore (and nearshore) wave data, time-series of the astronomical tide are derived from a nearby tide gauge at 15-minute intervals.

The historical monthly subaerial profiles, dating back to 1976, subaqueous bathymetry surveys, astronomical tide data, and offshore and nearshore wave data are all publicly available and can be downloaded freely from `http://narrabeen.wrl.unsw.edu.au`. For a full description of the multi-decade dataset is referred to Turner et al. (2016).

3.3.3 Applications of the dataset

This unique dataset has contributed greatly to our understanding of important physical processes in beach morphodynamics, and helped in the development and validation of numerous conceptual and numerical models (Splinter et al., 2018). The beach profiles and wave data greatly contributed to the current knowledge on embayment rotation (e.g. Short et al., 2000; Harley et al., 2011a, 2015) and the conceptual model of the distinction between various beach morphology states (Wright and Short, 1984) and further elaborations and new insights regarding this concept (e.g. Wright et al., 1985; Masselink and Short, 1993).

Aarninkhof (2003); Aarninkhof et al. (2003) used video-based observations of the surf zone at Narrabeen Beach from the Argus camera to derive the nearshore bathymetry. The high-frequency Lidar data has been used to develop a conceptual model for the beach recovery

following a storm event (Phillips, 2018), which is discussed in more detail in the next section. For a more inclusive overview of the research that is carried out using this dataset is referred to Splinter et al. (2018).

For the present study, the bathymetry surveys and high-frequency Lidar data are used to analyse the storm erosion and subsequent recovery towards pre-storm conditions (Section 3.4). The wave data, subaerial beach profiles and bathymetry surveys are used to set up a numerical model (Chapter 4). The observed subaerial beach profiles are used to to assess the performance of the model, in terms of subaerial beach profile and volume evolution (Chapter 5). The Lidar data is also used to analyse the swash motions, and hence provides information on the total runup height on the beachface. This runup data is used to develop an empirical model to predict the runup height, which is implemented in the XBeach model formulation (Chapter 6).

3.4 Post-storm beach recovery

On April 20 – 22, Narrabeen Beach (and the surrounding coastline) was impacted by an intense ECL, leading to an offshore significant wave height of 8.1 m. This corresponded to a peak nearshore significant wave height of 3.7 m around the 10 m depth contour, and coincided with spring tide. As a consequence, the Lidar recorded a Total Water Level (TWL) – the summation of the ocean water level and the runup on the beach – of up to 3.7 m above Mean Sea Level (MSL). The storm lasted for approximately 48 hours and resulted in a total erosion of 199,600 m^3, corresponding to an embayment-averaged erosion of 55 m^3/m and a shoreline retreat of 19 m (Harley et al., 2016). At the Lidar transect (see Figure 3.1 – right), the storm resulted in an erosion volume of approximately 52 m^3/m (see Figure 3.5 – top), and a shoreline retreat of over 30 meters. The effect of the storm on the beach profile is illustrated in Figure 3.4 – left.

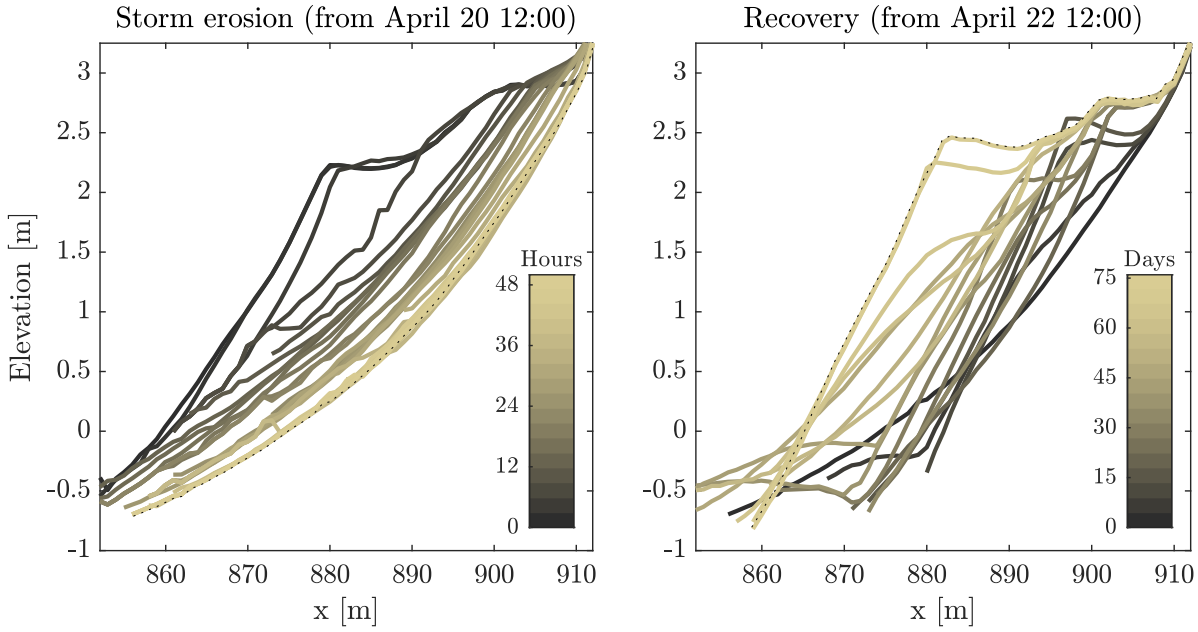

Figure 3.4: The April 2015 storm erosion (left, colours indicate hours after April 20th 12:00) and subsequent recovery (right, colours indicate days after April 22nd). The last profile of both figures is indicated with a dotted black line.

Following the storm erosion, the beach recovered towards its pre-storm conditions in terms of subaerial volume and vertical growth of the berm over a period of 76 days (see Figure 3.4 – right). In contrast to the profile evolution during the storm event (a progressively eroding profile can be observed in Figure 3.4 – left), there is no continuously accreting trend in profile evolution during the subsequent recovery. This is due to the variability in wave conditions, which together with phase of the spring-neap tidal cycle affects the behaviour of the berm (Phillips et al., 2019). The subaerial beach volume during the recovery period (right axis) is compared to the dimensionless fall velocity (left axis) in Figure 3.5.

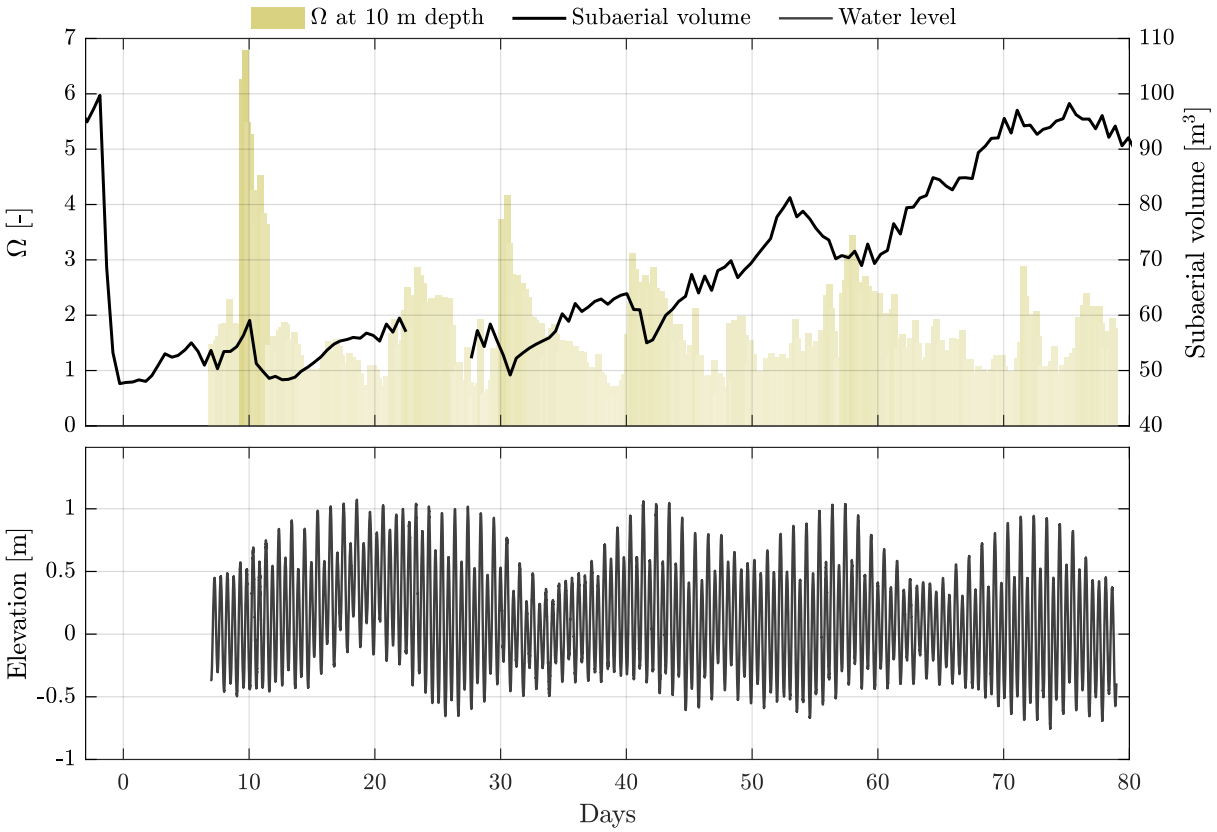

Figure 3.5: Subaerial beach volume development obtained from the low tide profiles (black line, right axis), with the dimensionless fall velocity Ω indicated in beige (left axis).

3.4.1 Modes of beach recovery

By analysing low tide subaerial beach profiles, derived from the continuously scanning Lidar, Phillips (2018) was able to identify four different behavioural modes during the recovery of the subaerial beach, over a period of ∼ 2.5 months following the April 2015 storm event (see Figure 3.6). The different modes are classified based on the four different combinations of volume change of the beachface (i.e. seaward of the primary berm crest) and the berm (landward of the berm crest). Firstly is distinguished between beachface erosion or progradation. Subsequently, for both classifications is verified whether vertical berm aggradation occurs or not.

The volume changes between two consecutive low tide profiles of the beachface (indicating beachface erosion or progradation) are plotted against the volume changes of the berm (indicating berm aggradation, i.e. vertical growth) in Figure 3.7, illustrating the definition of the four classifications. Beachface progradation without berm aggradation (Mode 1) is illustrated in green, and red corresponds to beachface progradation with berm aggradation (Mode 2). Beachface erosion in combination with berm aggradation (Mode 3) is indicated in cyan, and beachface erosion without berm aggradation (Mode 4) in blue.

The different behavioural modes that are observed during the recovery of the subaerial beach are illustrated in Figure 3.6, where the days following the start of recovery period are indicated with the shading of the line colours. The first profile within the evolution that is displayed in each panel is indicated in black and evolves into the colour corresponding to each mode.

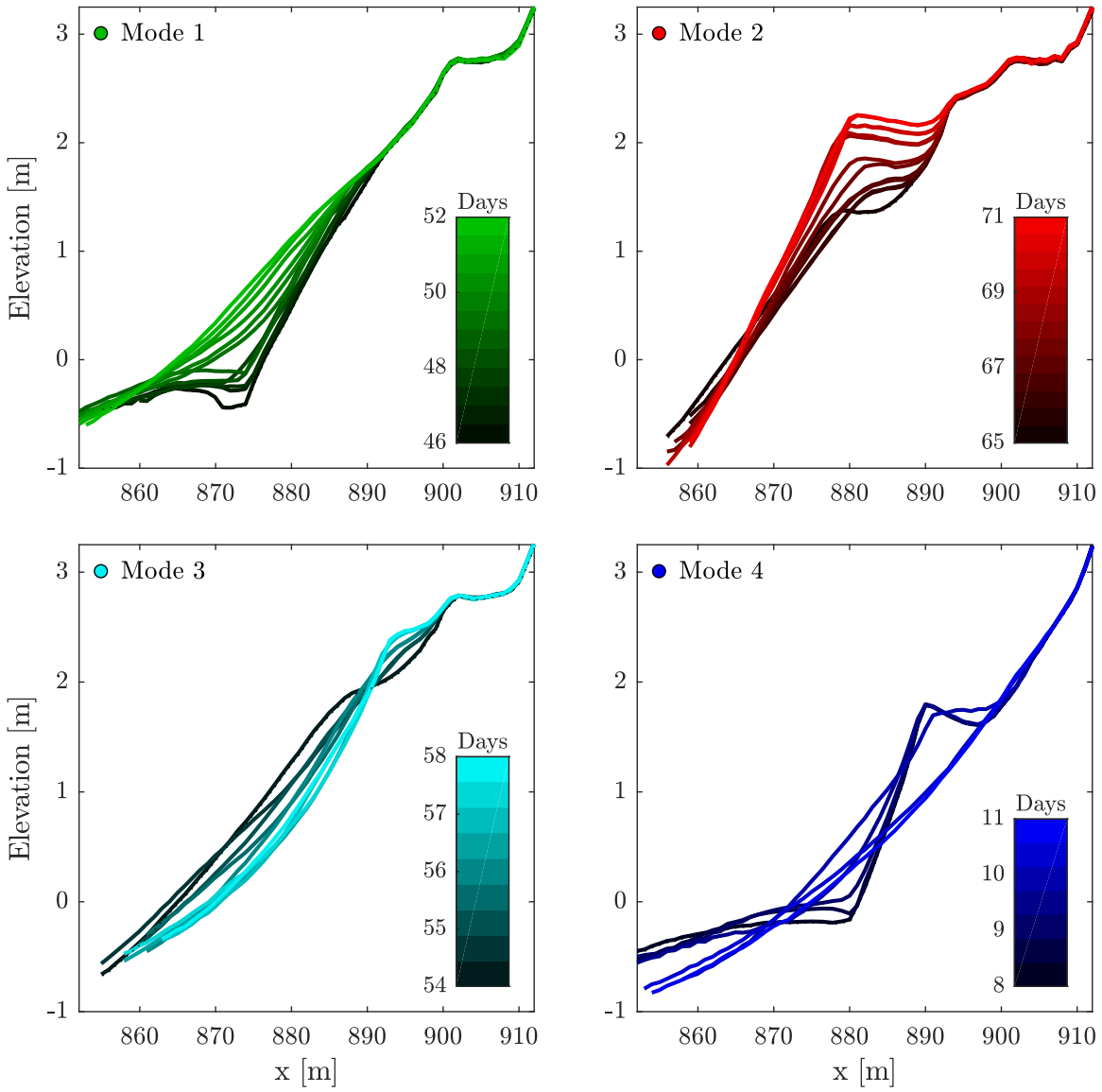

Figure 3.6: Four different behavioural modes during the beach recovery after a storm event. The colours indicate the day after the storm, where the first day within each panel is indicated in black, and the line colour evolves (over time) into the colour corresponding to each mode.

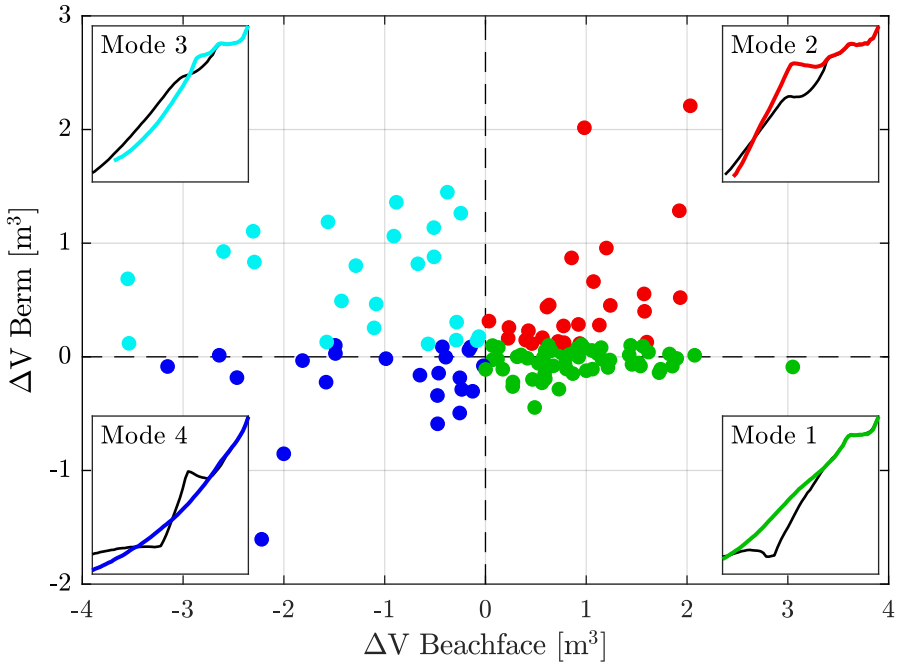

Figure 3.7: Definition of the four behavioural modes in terms of beachface and berm volume change. The colours correspond to the different behavioural modes.

Mode 1 – Beachface progradation without berm growth.
Mode 1 is defined as the seaward progradation of the beachface where no vertical growth of the berm occurs (see Figure 3.6 – panel 1), and is observed when the swash does not exceed the berm crest. This is generally the case during mild wave conditions and a decreasing tidal range (i.e. the transition from spring tide to neap tide). As the tidal range decreases, the upper swash gradually deposits sediment lower and lower on the beachface, causing a gradual spreading over the beachface.

Mode 2 – Beachface progradation with berm aggradation.
Mode 2 is defined as the horizontal and vertical growth of the subaerial beach, and is generally associated with an increasing tidal range (i.e. the transition from neap tide to spring tide). Around neap tide, the upper swash zone has been more or less concentrated at a certain elevation on the beachface, allowing for the formation of a neap berm. The subsequent days of increasing tidal range, the TWL rises and the upper swash processes progressively deposit sediment higher up the beachface. This is illustrated in Figure 3.6 – panel 2.

Mode 3 – Beachface erosion with berm aggradation.
Mode 3 is defined as beachface erosion with vertical berm growth, and is often accompanied with high water levels and profile steepening (Figure 3.6 – panel 3). When the water level is high, the onshore transport of sediment on the lower beachface might be more limited due to a lower bed shear stress. As a consequence, the beachface erodes, and as the upper swash exceeds the berm crest, sediment is deposited on top of the berm.

Mode 4 – Beachface erosion without berm aggradation
Mode 4 is defined as erosion of the beachface (and potentially the berm) without vertical growth, and is observed during moderate to energetic wave conditions. Under similar conditions as for Mode 3, but in the absence of swash exceedance, the profile becomes steeper and more concave, and sediment is transported offshore, and no vertical growth occurs (Figure 3.6 – panel 4).

The growth in subaerial beach volume, together with the temporal evolution of the different recovery modes throughout the recovery period is illustrated in Figure 3.8. The colours of the markers indicate the behavioural mode, as explained earlier (see e.g. Figures 3.6 & 3.7).

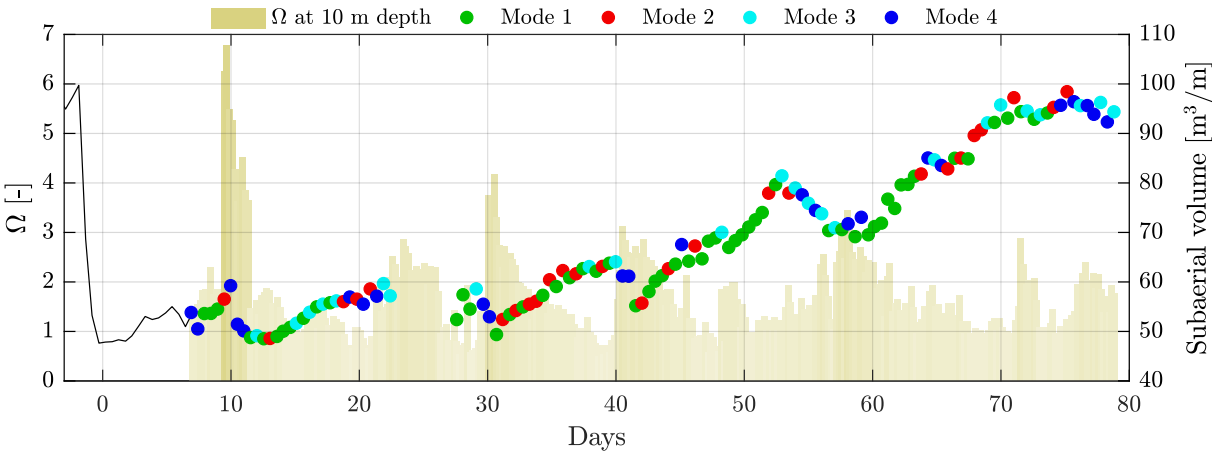

Figure 3.8: The evolution of the four different behavioural modes and subaerial beach volume throughout the recovery following the April 2015 storm. The markers indicate the behavioural modes (see Figure 3.6). The dimensionless fall velocity Ω is indicated in beige (left axis).

This present analysis of the recovery of the subaerial beach following the April 2015 storm will be used to assess the model's performance (Chapter 5). The model results will be analysed and compared to the observations on the following aspects:

- *Profile evolution* – The predicted subaerial beach profiles will be compared to the observed profiles. Besides the accuracy of the predicted post-recovery profile, the behaviour of the subaerial beach profile is also compared to the observations.
- *Subaerial beach volume* – The modelled subaerial beach volume will be compared to the observed evolution throughout the whole recovery period, to assess the ability of the model to predict the response to variable wave conditions.
- *Behavioural modes* – Finally, the ultimate goal of this study is to develop a model that predicts the various modes of beach recovery (e.g. Figure 3.6). The evolution of the predicted modes throughout the recovery period will be compared to the observed evolution of the behavioural modes (i.e. Figure 3.8).

Chapter 4

XBeach model

Model description and parameter sensitivity

4.1 Introduction

XBeach (eXtreme Beach behaviour) is an open-source numerical model that was initially developed by Roelvink et al. (2009) to simulate the morphological response to extreme storm events. The model is validated on a range of laboratory settings (e.g. Palmsten and Splinter, 2016) as well as field studies (e.g. Splinter and Palmsten, 2012; Van Dongeren et al., 2013; Stockdon et al., 2014), and aims to model relevant processes in each of the four storm impact regimes, being the swash, collision, overwash and inundation regimes (Sallenger, 2000).

The model can be used as a profile model in 1D (e.g. Pender and Karunarathna, 2013), or as an area model in 2D (e.g. McCall et al., 2010), and today, there are three modes in which the hydrodynamics can be resolved in XBeach, being:

- *Stationary* – All wave group variations, and thereby all infragravity motions, are neglected, and only the mean motions are included. This type can be applied for modelling morphological changes under moderate wave conditions;
- *Surfbeat* – This in-stationary, hydrostatic mode, is wave group resolving, and is hence also applicable when one is interested in the swash zone processes; and
- *Non-hydrostatic* – The non-linear shallow water equations are solved, and hence individual short wave propagation and transformation is resolved.

Since the initial launch of the model (Roelvink et al., 2009), it has been expanded to allow for modelling of the hydrodynamics in lagoons, and around reefs, groundwater flow, and recently, a non-hydrostatic model development allows for the modelling of the hydrodynamics on gravel beaches (McCall et al., 2014, 2015). Over the past decade, many developments have been made by numerous researchers, MSc students and PhD students, and has made XBeach a well established numerical model in the field of coastal engineering.

Considering the time scales associated with beach recovery, and the importance of swash processes, the XBeach Surfbeat model is the obvious choice.

A brief model description is provided in Section 4.2, where the focus is on the processes and parameters that are relevant for this study. The general model setup is discussed in Section 4.3. The parameter sensitivity of the model is discussed in Section 4.4.

4.2 Model description

The model description presented in this section is largely based on the publication of Roelvink et al. (2009) and the XBeach user manual. The present section focusses on hydrodynamics, sediment transport and wave non-linearity. A behavioural Bermslope module (Roelvink and Costas, 2017) that is developed to account for sediment transport in the upper swash zone, and allow for the simulation of berm growth in XBeach, is also described. Finally, the boundary conditions are discussed. The full model description is included in the XBeach manual.

4.2.1 Hydrodynamics

The wave action balance is solved to obtain the wave forcing:

$$\frac{\partial A}{\partial t} + \frac{\partial c_x A}{\partial x} + \frac{\partial c_y A}{\partial y} + \frac{\partial c_\theta A}{\partial \theta} = -\frac{D_w}{\sigma} \tag{4.1}$$

Where A is the wave action, c the wave propagation speed (where the subscripts refer to the x- and y-directions, and θ-space), θ is the angle of incidence, D_w the wave energy dissipation per directional bin and σ the intrinsic wave frequency. The wave action is given by:

$$A(x, y, t, \theta) = \frac{S_w(x, y, t, \theta)}{\sigma(x, y, t)} \tag{4.2}$$

In which the S_w is the wave energy density per directional bin. The total wave energy E_w is obtained by integration of the wave energy density S_w over all directional bins:

$$E_w = \int_0^{2\pi} S_w(x, y, t, \theta)\ \mathrm{d}\theta \tag{4.3}$$

The distribution of the total wave energy dissipation $\bar{D_w}$ over all directional bins is calculated proportional to the energy density distribution as follows:

$$D_w(x, y, t, \theta) = \frac{S_w(x, y, t, \theta)}{E_w(x, y, t)} \bar{D_w}(x, y, t) \tag{4.4}$$

The total wave energy dissipation is calculated using a method described by Roelvink (1993) as the product of the dissipation per breaking event and the fraction of broken waves Q_b. The energy dissipation per wave breaking event is assumed to take place over half of the representative wave

period T_{rep}, resulting in the following expression for the total, directionally integrated, wave energy dissipation:

$$\bar{D_w} = \alpha \frac{2}{T_{rep}} Q_b E_w \tag{4.5}$$

Where α is a calibration factor and E_w the total wave energy (Equation 4.3). The fraction of breaking waves Q_b is estimated from a Rayleigh distribution (Battjes and Janssen, 1978):

$$Q_b = 1 - \exp\left(-\left(\frac{H_{rms}}{H_{max}}\right)^n\right) \tag{4.6}$$

Where the root-mean-square wave height H_{rms} is calculated from the wave energy E_w, and the maximum wave height H_{max} is calculated using the breaker index γ_b (the ratio between the breaking wave height and the water depth, usually given the value 0.88, see Section 2.4.1):

$$E_w \sim \tfrac{1}{8}\rho g H_{rms}^2 \qquad \Rightarrow \qquad H_{rms} = \sqrt{\frac{8 E_w}{\rho g}}, \qquad H_{max} = \gamma_b h \tag{4.7}$$

This closes the set of equations for the wave action balance (Equation 4.1). From the wave energy, the wave-induced radiation stresses can be determined using linear wave theory.

Similar to the wave action balance, a roller balance is solved and coupled to the wave energy balance, where the wave energy dissipation forms a source of energy in the roller balance. The roller-induced radiation stress is calculated and together with the wave-induced radiation stress they are used to calculate the wave forcing:

The flows are calculated using a depth-averaged formulation of the shallow water equations, taking into account wave-induced mass flux and return flows. This Generalized Lagrangian Mean (GLM) formulation uses Lagrangian velocities (Andrews and McIntyre, 1978):

$$\frac{\partial u^L}{\partial t} + u^L\frac{\partial u^L}{\partial x} + v^L\frac{\partial u^L}{\partial y} - fv^L - v_h\left(\frac{\partial^2 u^L}{\partial x^2} + \frac{\partial^2 u^L}{\partial y^2}\right) = \frac{T_{sx}}{\rho h} - \frac{T_{bx}^E}{\rho h} - g\frac{\partial \eta}{\partial x} + \frac{F_x}{\rho h} \tag{4.8}$$

$$\frac{\partial v^L}{\partial t} + u^L\frac{\partial v^L}{\partial x} + v^L\frac{\partial v^L}{\partial y} + fu^L - v_h\left(\frac{\partial^2 v^L}{\partial x^2} + \frac{\partial^2 v^L}{\partial y^2}\right) = \frac{T_{sy}}{\rho h} - \frac{T_{by}^E}{\rho h} - g\frac{\partial \eta}{\partial y} + \frac{F_y}{\rho h} \tag{4.9}$$

$$\frac{\partial \eta}{\partial t} + \frac{\partial u^L h}{\partial x} + \frac{\partial v^L h}{\partial y} = 0 \tag{4.10}$$

Where the Lagrangian velocity components (denoted by the superscript L) are the superposition of the Eulerian velocity and the Stokes' drift velocity:

$$u^L = u^E + u^S \qquad \text{and} \qquad v^L = v^E + v^S \tag{4.11}$$

4.2.2 Sediment transport

The sediment transport is modelled with a depth-averaged advection-diffusion equation (Galappatti and Vreughenhil, 1985):

$$\frac{\partial(h\,C)}{\partial t} + \frac{\partial(h\,C\,u^E)}{\partial x} + \frac{\partial(h\,C\,v^E)}{\partial y} + \frac{\partial}{\partial x}\left(D_h\,h\,\frac{\partial C}{\partial x}\right) + \frac{\partial}{\partial y}\left(D_h\,h\,\frac{\partial C}{\partial y}\right) = \frac{h\,(C_{eq} - C)}{T_s} \quad (4.12)$$

With C the sediment concentration, D_h the horizontal diffusion coefficient, C_{eq} the equilibrium sediment concentration and T_s a factor to account for settling lag – the time it takes for a particle to settle to the bed:

$$T_s = \max\left(0.05\,\frac{h}{w_s}, 0.2\right) \quad (4.13)$$

The sediment fall velocity w_s is calculated using a formulation proposed by Ahrens (2000). The entrainment or deposition of sediment is determined based on the deviation from the equilibrium concentration (source term on the right hand side of Equation 4.12). A surplus of sediment means local deposition, and a lack of sediment yields local erosion. The equilibrium sediment concentration is calculated using a formulation proposed by Soulsby (1997), also known as the Soulsby-Van Rijn formulation:

$$C_{eq} = \frac{A_{sb} + A_{ss}}{h}\left(\left(|u^E|^2 + 0.018\frac{u_{rms}^2}{C_d}\right)^{0.5} - u_{cr}\right)^{2.4}(1 - \alpha_b\,m) \quad (4.14)$$

Where a distinction is made between the bed load sediment transport (denoted by the subscript sb), and the suspended sediment transport (denoted by the subscript ss). The equilibrium concentration is then used to determine whether the flow contains a surplus or lack of sediment, which acts as a source (or sink) in the advection-diffusion equation for sediment transport Equation 4.12. Subsequently, the bed updating is performed, which is calculated based on the gradients in sediment transport rates q_x and q_y.

$$\frac{\partial z_b}{\partial t} + \frac{f_{mor}}{1-p}\left(\frac{\partial q_x}{\partial x} + \frac{\partial q_y}{\partial y}\right) = 0 \quad (4.15)$$

Where z_b is the bed level, f_{mor} a morphological acceleration factor to reduce the computational time (e.g. Roelvink, 2006; Ranasinghe et al., 2011; Reniers et al., 2004) and p the sediment porosity. The sediment transport rates are calculated as follows:

$$q_x = \frac{\partial\left(h\,C\,u^E\right)}{\partial x} + \frac{\partial}{\partial x}\left(D_h\,h\,\frac{\partial C}{\partial x}\right) \quad (4.16)$$

$$q_y = \frac{\partial\left(h\,C\,v^E\right)}{\partial y} + \frac{\partial}{\partial y}\left(D_h\,h\,\frac{\partial C}{\partial y}\right) \quad (4.17)$$

4.2.3 Wave non-linearity

Grasso et al. (2011) showed that the wave-induced sediment transport caused by the wave skewness and asymmetry is the main process that drives onshore sediment transport. However, XBeach does not resolve the individual short waves in Surfbeat mode, and hence does not calculate the actual wave shape. The skewness- and asymmetry-induced sediment transport is therefore accounted for by means of an additional velocity term u_a (Van Thiel de Vries, 2009). In Equation 4.12, the Eulerian velocity components u^E and v^E are replaced by $u^E - u_a \sin(\theta_m)$ and $v^E - u_a \cos(\theta_m)$ respectively, with:

$$u_a = (f_{Sk}\, Sk - f_{As}\, As)\; u_{rms} \tag{4.18}$$

Where f_{Sk} and f_{As} are factors for the magnitude of wave skewness Sk and wave asymmetry As respectively. The wave skewness and asymmetry can be derived from the wave data as follows:

$$Sk_u = \frac{\overline{u_w^3(t)}}{\sigma_{u_w}^3} \qquad \text{and} \qquad As_u = \frac{\overline{H(u_w)^3(t)}}{\sigma_{u_w}^3} \tag{4.19}$$

Where u_w is the amplitude of the velocity, σ is the standard deviation, the overline represents a time average and H denotes the Hilbert transform, inducing a phase shift of 90 degrees. However, this post-processing technique cannot be used to predict the wave skewness and asymmetry.

Ruessink et al. (2012) developed a parametrisation to express the wave skewness and asymmetry in terms of the Ursell Number (see Doering and Bowen, 1995), based on over 30,000 field observations. Van Thiel de Vries (2009) combined this parametrisation with a wave shape model proposed by Rienecker and Fenton (1981), to construct a lookup table from which non-linear components can be interpolated.

$$Sk = \frac{0.79}{1 + \exp\frac{-0.61 - \log U_r}{-0.35}} \cos\left(-\frac{\pi}{2} + \frac{\pi}{2}\tanh\left(\frac{0.64}{U_r^{0.60}}\right)\right) \tag{4.20}$$

$$As = \frac{0.79}{1 + \exp\frac{-0.61 - \log U_r}{-0.35}} \sin\left(-\frac{\pi}{2} + \frac{\pi}{2}\tanh\left(\frac{0.64}{U_r^{0.60}}\right)\right) \tag{4.21}$$

These components are then substituted in Equation 4.18 to represent a non-linear contribution to the velocity that affects the sediment transport. Subsequently, Equation 4.18 is substituted in the advection-diffusion equation Equation 4.12.

It is however important to note that Ruessink et al. (2012) state that the use of this parametrisation is not recommended on bed slopes that are steeper than 1/30, which makes the accuracy of this method in XBeach questionable for this study. Van Rooijen (2011) also concluded that the by XBeach predicted (magnitude and direction of) sediment transport in the swash zone is questionable, especially on reflective beaches.

4.2.4 Bermslope model

On (semi-)reflective beaches, incident band swash becomes more important, and swash hydrodynamics and sediment transport are governed by complex processes like bore collapsing, high turbulence intensities, flow acceleration, swash flow asymmetry and in- and exfiltration (see Section 2.5), which are currently not accounted for in the XBeach model formulation. To account for the effect of these processes on the onshore sediment transport, berm growth, and profile shape, a behavioural Bermslope model is implemented in XBeach that adjusts the calculated (process-based) sediment transport in the swash zone (Roelvink and Costas, 2017). This Bermslope model calculates a sediment transport correction, based on the deviation of the instantaneous swash slope from the prescribed equilibrium *bermslope*:

$$q_{bermslope,x} = f_{bermslope}\, c^u\, v_{mag}^u\, h^u \left(\frac{\mathrm{d}z_b}{\mathrm{d}x} - bermslope \right) \tag{4.22}$$

Where $q_{bermslope}$ is the sediment transport correction, $f_{bermslope}$ a calibration factor, c the sediment concentration, v_{mag} the velocity magnitude, h the water depth, the superscript u denotes u-points, $\frac{\mathrm{d}z_b}{\mathrm{d}x}$ the instantaneous local bed slope and *bermslope* the prescribed equilibrium (target) swash slope. This $q_{bermslope,x}$ transport term is added to the calculated sediment transport q_x in Equation 4.15 to perform the bed updating.

4.2.5 Boundary conditions

At the offshore boundary, a time series of the water level is imposed, as well as the wave forcing. The wave forcing is calculated based on a JONSWAP spectrum, and a random wave spectrum is calculated at the prescribed temporal interval based on the following set of parameters:

Parameter	Description
H_{m0}	The significant wave height;
T_p	The peak period of the spectrum;
$\overline{\theta}$	Main wave angle of incidence;
γ_{jsp}	Peak enhancement factor; and
s	Measure for the directional spreading.

Table 4.1: Parameters used for the JONSWAP spectrum definition.

The peak enhancement factor γ_{jsp} is a measure for the range in frequencies, and hence the spreading/width of the spectrum. A high value corresponds to a sharp/peaked (narrow-banded) frequency spectrum, a value of 1 corresponds to a Pierson Moskowitz spectrum (Pierson and Moskowitz, 1964) and a value of 3.3 (default) corresponds to a standard JONSWAP spectrum (Hasselmann et al., 1973). The spectrum includes the infragravity wave component, which is calculated based on a method described by Van Dongeren et al. (2003).

4.3 Model setup

For the present study, a 1D numerical model will be used to predict the recovery of the subaerial beach following a storm event. The 1D XBeach model requires the following model input:

- Initial condition (bathymetry);
- Offshore water level (tide);
- Wave conditions (H_s, T_p and θ_0); and
- Sediment characteristics (i.e. D_{50}).

The initial condition of the bed level is constructed from the combined measurements of the subaerial beach (obtained from the Lidar measurements), swash zone (RTK-GPS measurement carried out by the WRL) and nearshore bathymetry (up to a depth of 16 m, obtained by a jetski survey). The data (discussed in Section 3.3) is interpolated and combined, and linearly extended up to a depth of 20 m. The resulting cross-shore profile is resented in Figure 4.1 – left, and a close-up of the surf and swash zone is provided in the right figure, indicating the tidal range in gray.

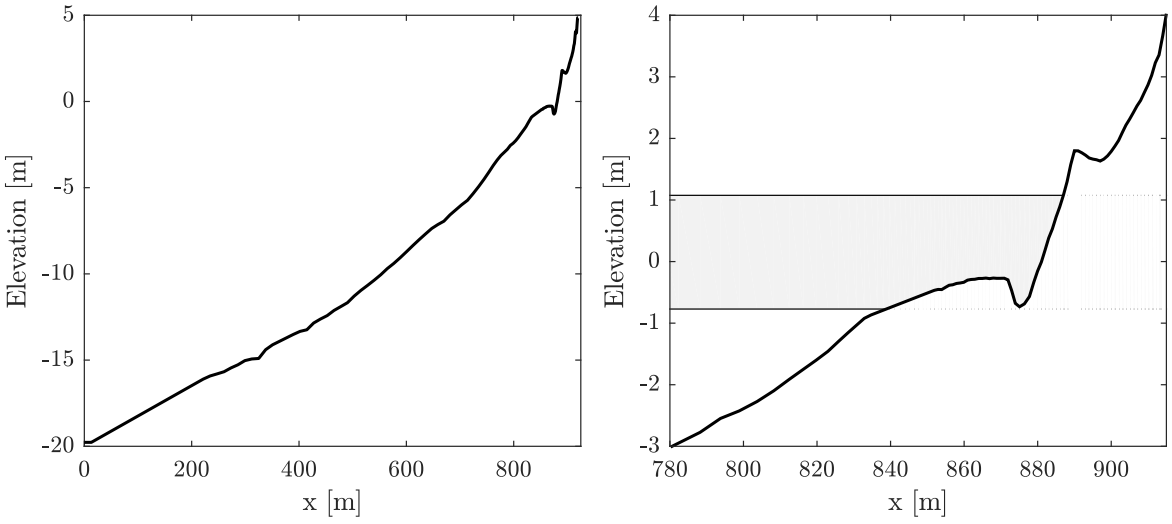

Figure 4.1: Initial condition of the bed level, based on measurements from April 29th 2015. The range of the tide is indicated in gray in the right figure.

The data from the wave buoy (see Figure 3.1 – left) is used to construct a time series of the water level, which is imposed at the offshore boundary (at 20 m water depth). The offshore wave data is also used to the nearshore wave characteristics using the wave transformation model MIKE21 (DHI, 2014). This wave data is used to calculate a random JONSWAP spectrum at each hour of computation, which is imposed at the offshore boundary.

Sediment characteristics are specified in the input file, by assigning a median grain diameter $D_{50} = 0.3$ mm (Section 3.2). It is also possible to model a certain grain size distribution and account for sediment sorting. This is however not considered for the present study. The input file required specification of more parameters, which is discussed in Section 4.4 and Section 5.2.

4.4 Parameter sensitivity

For the calibration of the XBeach Surfbeat model, some parameters are believed to be more important or sensitive than others. Following the literature review in Chapter 2, the onshore sediment transport turns out to be the main source of the sediment that needs to be deposited on the beachface, to ensure both the vertical and horizontal growth of the berm. Wave non-linearity was found to be very effective for the net onshore transport of sediment in the surf zone. Furthermore, processes in the swash zone that appeared to be relevant for the sediment transport in the upper swash zone were turbulence and in- and exfiltration. This section identifies and discusses the relative importance of the following processes on the model results:

- *Wave non-linearity* – The effect of wave non-linearity on the sediment transport is accounted for by an additional velocity term u_a in the advection-diffusion equation (Equation 4.12). This velocity term includes the contribution of wave skewness and wave asymmetry (Equation 4.18), and is calibrated with the factors f_{Sk} and f_{As} respectively.
- *Turbulence-induced sediment stirring* – There are 3 models to translate the turbulence at the surface to the near-bed turbulence. The near-bed turbulence affects the sediment concentration, and hence the sediment transport.
- *Groundwater flow* – A groundwater flow module is implemented in XBeach, which can be turned on to take into account groundwater flow and infiltration on the beachface.
- *Dilatancy* – Dilatancy refers to the reduction in sediment mobilisation during overwash conditions as high uprush velocities cause a stabilisation of the grains. Therefore dilatancy affects the onshore sediment transport and potentially "limits" vertical growth of the berm.

These processes listed above are accounted for in the XBeach model formulation through the parameters that are summarised in Table 4.2. The table presents the default values, and shows the range of tested values to assess their sensitivity on the model results.

Parameter		Value	
Symbol	Description	Default	Tested range
f_{Sk}	Wave skewness factor	0.10	0.13 - 0.27
f_{As}	Wave asymmetry factor	0.10	0.10 - 0.16
$Turb$	Turbulence-induced sediment stirring model	bore-averaged	BA/WA/none
$gwflow$	Groundwater flow module	0	0 - 1
$dilatancy$	Dilatancy module	0	0 - 1

Table 4.2: Overview of the free parameters that are varied for the sensitivity analysis.

The complete parameter setting of the simulations that were carried out for this parameter sensitivity analysis is presented in Appendix A. Furthermore, an overview of the different model simulations that were performed is presented in Table A.2.

4.4.1 Summary

The parameter sensitivity is described in Appendix A. The key findings are summarised here.

The effect of wave skewness and asymmetry are accounted for by means of two calibration factors f_{Sk} and f_{As}, which both enhance onshore sediment transport. The effect of f_{As} is more prominent closer to the beachface, whereas f_{Sk} has more influence slightly further offshore, which agrees with the theory discussed in Section 2.3. The wave skewness acts more in the shoaling zone and is found to drive onshore bar migration (e.g. Walstra et al., 2007), and the asymmetry becomes more important in shallower water in the breaker and swash zone. Especially wave asymmetry is effective for the exchange of sediment between the inner surf zone and the subaerial beach. However, to ensure enough sediment supply from the surf zone, the wave skewness factor should tweaked as well.

The turbulence model has a major effect on the magnitude of the sediment transport in the surf zone and swash zone. The bore-averaged model results in the highest near-bed turbulent intensities, and hence the largest magnitude of sediment transport. As a consequence, the beach is unrealistically dynamic, even under very moderate wave conditions, leading to several meters of shoreline progradation and retreat within one tidal cycle. The wave-averaged formulation results in a much more stable beach profile, and gives a slightly smoother berm profile. Not taking into account the effect of surface-generated turbulence on the near-bed turbulent intensity yields the lowest magnitude of sediment transport.

Groundwater flow modelling takes into account the effect of in- and exfiltration, and affects the stability of the grains on the beachface. Turning on the groundwater flow module slightly enhances the onshore transport of sediment, and vertical growth of the berm.

As expected, dilatancy limits the mobilisation of sediment during uprush, and hence reduces the onshore and more importantly up-slope sediment transport. Therefore, the dilatancy module should not be used when one is interested in simulating berm growth.

Chapter 5

Model results

5.1 Introduction

The previous chapter provided a brief introduction to the XBeach model (largely based on Roelvink et al., 2009). The model setup was discussed and a small sensitivity analysis was carried out and presented to highlight the parameters that are relevant for the calibration of the model. The present chapter presents the results of two types of model runs, being the traditional XBeach surfbeat model and the recently developed Bermslope model (Roelvink and Costas, 2017, see Section 4.2.4).

First, Section 5.2 describes the model calibration process and explains how the model skill is assessed. The results of the standard XBeach model (i.e. without Bermslope model) are presented in Section 5.3. Next, Section 5.4 presents the results of the Bermslope model. The results and shortcomings of the two modelling approaches are discussed in Section 5.5, highlighting the need for additional model development.

5.2 Model calibration

Calibration of a numerical model is carried out by optimising the combination of (a subset of) the free parameters of the model's input to achieve the best model performance. The free parameters are systematically varied during the calibration process, and the the performance is verified for each simulation until it converges towards an optimum.

The performance, or skill, of a numerical model can be verified on different aspects, and quantified in a number of different ways. For the present study, the model's skill will be assessed by taking into consideration the bed level changes and volume changes of the subaerial beach. Furthermore, the accuracy of the predicted total runup height on the beachface is verified through comparison with observations. Finally, the profiles are used to determine the behavioural modes throughout the recovery period (as defined by Phillips, 2018, see Section 3.4.1). The model's ability of representing the observed behaviour is assessed by comparing the predicted and observed modes.

Subaerial beach profile evolution
With respect to modelling bed level changes, many coastal modelling studies assess the model skill through the Brier Skill Score (BSS). The BSS assigns the model skill based on the relative error between the prediction and observation, with respect to the observed changes:

$$\mathrm{BSS} = 1 - \frac{\left\langle |Z_o - Z_p|^2 \right\rangle}{\left\langle |Z_o - Z_b|^2 \right\rangle} \tag{5.1}$$

Where Z_p is the predicted bed elevation, Z_o the observed bed elevation and Z_b the baseline bed level elevation (i.e. the bed level at the start of the simulation) of the subaerial beach. The angle brackets $\langle\rangle$ denote domain-averaged, and $||$ refers to the absolute (non-negative) value. A BSS $= 1$ yields perfect model skill (Sutherland et al., 2004), and a BSS ≥ 0.6 is considered to indicate "good" predictive skill (Van Rijn et al., 2003).

Subaerial beach volume
When one is interested in different processes than bed level changes, other indicators for the model skill are for example the Mean Squared Error (MSE), or the correlation between predictions and measurements. Another method to assess the model skill is by means of the Relative Mean Absolute Error (RMAE) (Van Rijn et al., 2003):

$$\mathrm{RMAE} = \frac{\langle |V_o - V_p| \rangle}{\langle |V_o| \rangle} \tag{5.2}$$

Where, in the present study, V_o is the observed subaerial beach volume and V_p the predicted subaerial beach volume.

Runup height
The prediction of the runup height is assessed by calculating the correlation between the observed and predicted $R_{2\%}$ runup height. Furthermore, following Van der Westhuysen et al. (2012), the Relative BIAS (Rel. BIAS) and Scatter Index (SCI) are computed. The BIAS is the difference between a population mean of the results and an accepted reference or true value (e.g. Bainbridge, 1985). The Rel. BIAS is therefore a measure for the overall over- or under-estimate of the predicted value, relative to the observations (after Van der Westhuysen et al., 2012):

$$\text{Rel. BIAS} = \frac{\sum_{i=1}^{N} \left(\psi_p^i - \psi_o^i\right)}{\sum_{i=1}^{N} \psi_o^i} \tag{5.3}$$

Where ψ_p^i is the predicted quantity and ψ_o^i the observed quantity. The SCI is a measure for the amount of scatter and is computed as follows (Van der Westhuysen et al., 2012):

$$\mathrm{SCI} = \frac{\sqrt{\left\langle (\psi_p - \psi_o)^2 \right\rangle}}{\langle \psi_o \rangle} \tag{5.4}$$

Behavioural modes

The model's ability in predicting the correct behavioural mode is verified by comparing each predicted mode (between two consecutive low tide profiles) to the observed mode. The accuracy can be expressed by constructing a confusion matrix (Pearson, 1904), which displays the number of correct and incorrectly assigned modes. An example of a confusion matrix is presented in Figure 5.1, where the predicted coastline change (vertical axis) is compared to the observed coastline change (horizontal axis).

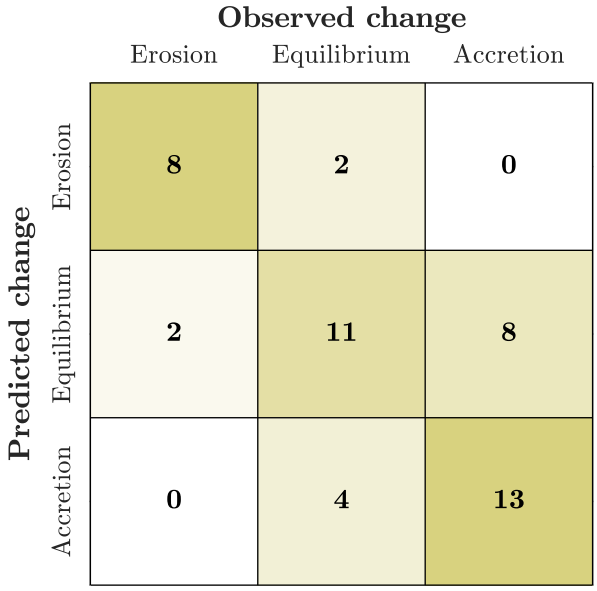

Figure 5.1: Confusion matrix (Pearson, 1904) illustrating the accuracy of a model in predicting shoreline change. The predicted shoreline change (left axis) is compared to the observed shoreline change (top axis) and the shading and numbers indicate (in)correct predictions.

In this example, the model predicts erosion 10 times, of which 8 times correctly and 2 times incorrectly (Figure 5.1). The shading indicates the accuracy (i.e. the fraction of correctly predicted changes) and hence, a diagonal with high values indicates good predictive skill.

To summarise, in the present study, the XBeach model performance will assessed by taking into consideration the following aspects:

- *Profile evolution* – The model's capability of predicting the observed profile evolution throughout the recovery period can be assessed using the BSS. However, the shape of the profile is also visually compared to the observations.
- *Subaerial beach volume* – The predicted subaerial beach volume (the dry beach, i.e. above Mean Sea Level (MSL)) is compared to the observations through the RMAE.
- *Recovery mode* – The behavioural mode is determined as explained in Section 3.4.1. The model's capability in predicting the right behavioural mode is assessed by means of a confusion matrix (Pearson, 1904) of which an example is provided in Figure 5.1.
- *Runup height ($R_{2\%}$)* – The total runup height on the beachface is compared to the observations by firstly calculating the $R_{2\%}$ values of the observed and predicted runup height. Consequently, the correlation, Rel. BIAS and SCI are computed to assess the accuracy of the predicted runup height.

5.3 Results standard XBeach

5.3.1 Calibration

The "standard" XBeach model (i.e. without the Bermslope transport correction) is calibrated by varying the parameters summarised in Table 5.1. The optimal parameter setting is determined based on optimising the accuracy of the predicted subaerial volume development throughout the recovery period as well as the subaerial beach profile. The parameters in Table 5.1 are varied systematically, towards an optimum. First, f_{Sk} and f_{As} were increased alternately to get to the right amount of subaerial beach volume growth. Subsequently, in an attempt to improve the profile shape, groundwater flow modelling, various turbulence models and D_{50} values were tested. Finally f_{mor} was reduced in an attempt to improve the results. The final parameter setting resulting from the model calibration is presented in the right column (Table 5.1), and an overview of all model simulations is presented in Table B.2 (see Section B.2).

Parameter		Value		
Symbol	Description	Default	Range	Final
D_{50}	Grain diameter [m]	0.0002	0.0002 - 0.0008	0.0003
f_{Sk}	Wave skewness factor	0.10	0.10 - 0.5	0.45
f_{As}	Wave asymmetry factor	0.10	0.10 - 0.35	0.35
$Turb$	Turbulence-induced sediment stirring model	BA	BA/wA/none	BA
f_{mor}	Morphological acceleration factor	1.0	1.0 - 10	10
$gwflow$	ground water flow module	0	0 - 1	1

Table 5.1: Overview of the free parameters that are varied during the model calibration.

The grain diameter was found to have very little effect on the predicted profile evolution as well as on the subaerial beach volume change throughout the modelled recovery period, and is therefore set to the initial value based on literature (Short, 2007, see Section 3.2). Relatively high values for the calibration factors f_{Sk} and f_{As} are required to force enough onshore sediment transport and the right magnitude of subaerial beach growth. Using a different turbulence model did affect the (magnitude of) the erosion, however, it did not improve the shape of the beach profile and was therefore set to the default setting "bore-averaged".

5.3.2 Results

The predicted profile evolution throughout the simulated recovery period is compared to the observed profiles in Figure 5.2. For 12 days within the recovery period, the predicted beach profile (solid black line) and the observed beach profile (dashed black line) are plotted, together with the post-storm (dotted gray line) and the post-recovery (dashed-dotted gray line) beach profile. The profiles are presented for each $\sim 6^{\text{th}}$ day, which is indicated in the bottom right corner of each panel. Note that day 24 is missing, due a not functioning Lidar for 4 days (days 22-27), for which no data is available.

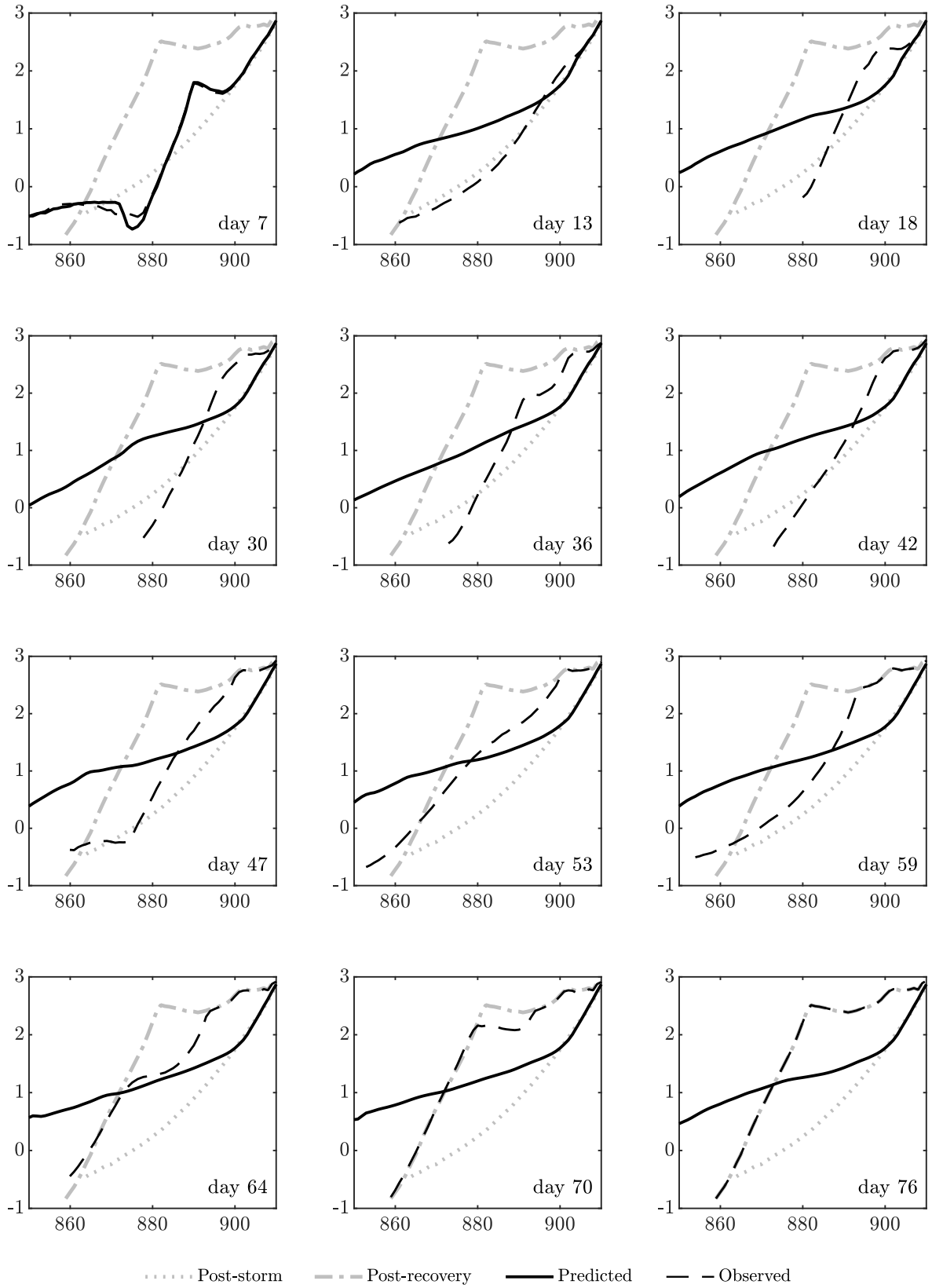

Figure 5.2: The predicted (solid) vs the observed (dashed) profile evolution during recovery. The post-storm and post-recovery profiles are indicated with a gray dotted and dashed-dotted line, respectively.

The model quickly predicts a dissipative beach profile with a much flatter slope than observed (Figure 5.2). Furthermore, the berm that is present from day 18 onward is also absent in the predicted beach profile throughout the remaining recovery period. The model obtains a BSS = 0.32 at the end of the recovery (day 76) which is considered "reasonable/fair" ($0.3 \leq$ BSS ≤ 0.6) according to Van Rijn et al. (2003). However, by simply looking at the difference between the two profiles it is concluded that the performance is rather poor. Furthermore, throughout the recovery period, the model obtains a BSS < 0 for 80% of the time, indicating poor model skill. The BSS throughout the recovery period is presented in Figure 5.4 in dark gray.

The subaerial beach volume is calculated as the volume between MSL and MSL + 3.25 m. This threshold is chosen to cover a spatial domain that is spanned in all the available low tide profiles throughout the considered recovery period. Figure 5.3 presents the predicted subaerial beach volume (solid black line) compared to the observed subaerial beach volume (dashed black line). The dimensionless fall velocity Ω is calculated at the 10 m depth contour, in line with the study of Phillips et al. (2019). Ω is indicated in beige and can be read from the left axis.

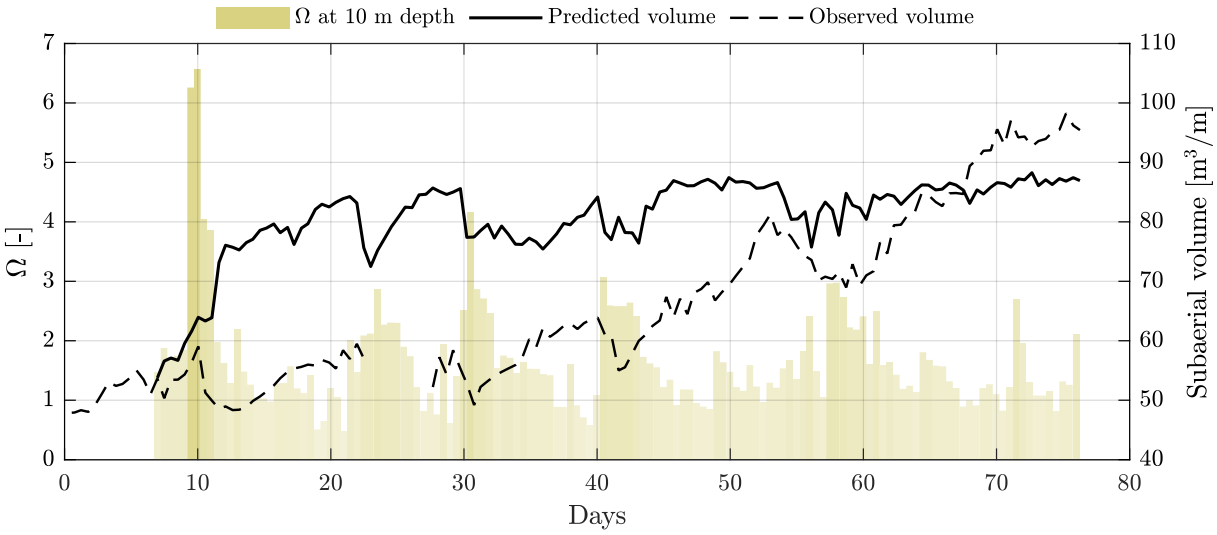

Figure 5.3: The predicted (solid) vs the observed (dashed) subaerial volume change during the 76-day recovery period (right axis). The dimensionless fall velocity Ω (see Equation 2.20) is indicated in beige (left axis).

The predicted subaerial beach volume approaches the observed volume towards the end of the recovery period. However, the accretion in the beginning of the simulation is way too rapid, and the reset event around day 10 is not captured by the model (Figure 5.3). Furthermore, the general rate of subaerial beach volume change basically approaches zero towards the end of the considered period, while the observed rate of volume change is highest (e.g. days $60 - 70$). The model obtains a RMAE = 0.09 at the end of the recovery period, which is considered to be "good". However, throughout the simulation the model performs poorer with occasionally RMAE ≥ 0.5 and a simulation time-averaged RMAE = 0.24. The RMAE is calculated throughout the entire recovery period, and is illustrated in Figure 5.4 in light gray.

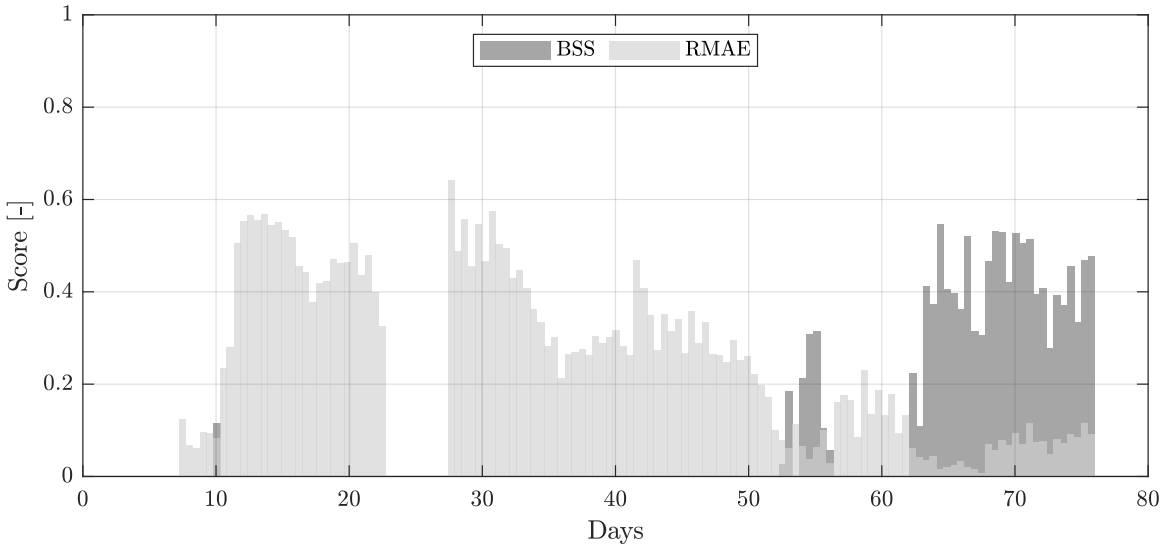

Figure 5.4: The model performance in terms of BSS (dark gray) and RMAE (light gray) throughout the entire recovery period.

5.3.3 Conclusion

The standard XBeach model is not capable of capturing the observed behaviour during the recovery of the subaerial beach. This is possibly because XBeach is developed for dissipative beaches which are characterised by a wide surf zone with a gradual slope. Reflective beaches are morphodynamically very different from dissipative beaches, and have a much steeper beach slope. Oliveira (2014) also reported that XBeach needs significantly more calibration for morphodynamic modelling on a reflective beach compared to dissipative beaches.

5.4 Results XBeach Bermslope

5.4.1 calibration

To account for swash processes that are important for berm growth and not captured by the process-based modelling approach, the behavioural Bermslope module (Roelvink and Costas, 2017) is turned on (see Section 4.2 for a description). The Bermslope model applies a sediment transport correction in the swash zone, and hence operates in the same region as the wave skewness and asymmetry. Furthermore, the formulation introduces a number of additional free parameters, which need to be calibrated as well. Therefore, a new model calibration is carried out, of which the final parameter setting and the range of tested values for these parameters are presented in Table 5.2. The simulations that are carried out during the model calibration, as well as the full parameter setting are presented in Section B.3.

Parameter		Value		
Symbol	Description	Default	Range	Final
f_{Sk}	Wave skewness factor	0.10	0.15 - 0.30	0.27
f_{As}	Wave asymmetry factor	0.10	0.05 - 0.20	0.14
$Turb$	Turbulence-induced sediment stirring model	BA	WA/none	none
f_{mor}	Morphological acceleration factor	1.0	1.0 - 10	10
$gwflow$	ground water flow module	0	0 - 1	1
$bermslope$	Equilibrium swash slope	0.10	0.15 - 0.24	0.24
$f_{bermslope}$	Calibration factor	15	10 - 15	10

Table 5.2: Overview of the free parameters that are varied during the model calibration of the XBeach Bermslope model.

As explained earlier, the Bermslope model acts in the swash zone and therefore overlaps with the effect of the wave skewness and asymmetry. Therefore, values for f_{Sk} and especially f_{As} are significantly lower using this modelling approach. The parameter $bermslope = 0.24$ corresponds to the observed swash slope at Narrabeen beach during calm conditions. High values of $f_{bermslope}$ forced the profile too quickly and resulted in unrealistically high onshore sediment transport rates, and the formation of a submerged berm in the swash zone as a consequence. The final value of 10 was found to be just enough to ensure the profile attains the prescribed slope.

5.4.2 Results

The predicted subaerial beach profile evolution (solid black line) throughout the recovery period is compared to the observations (dashed black line) in Figure 5.5, where the post-storm (dotted line) and post-recovery (dashed-dotted line) profiles are indicated in gray.

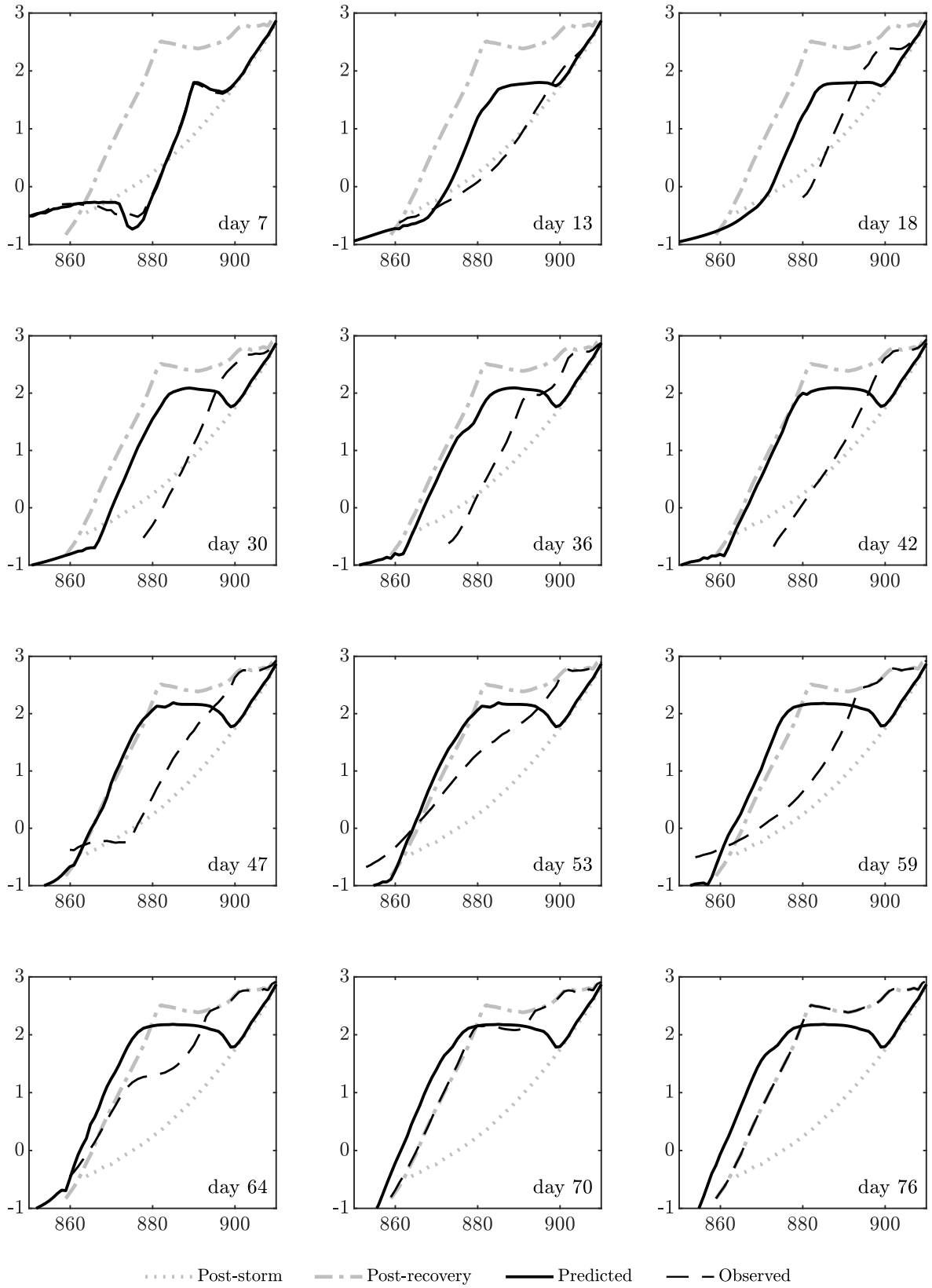

Figure 5.5: The predicted (solid) vs the observed (dashed) profile evolution during recovery. The post-storm and post-recovery profiles are indicated with a gray dotted and dashed-dotted line, respectively.

The profile evolution (Figure 5.5) shows that berm growth is represented much better by the Bermslope model (solid black line) than standard XBeach model (discussed in Section 5.3). The swash slope is much steeper and attains the right cross-shore gradient during reflective conditions (e.g. days 70 and 76 in Figure 5.5). However, during storm conditions the predicted profile is characterised by the same steep swash slope, while the observations indicate erosion and profile flattening (e.g. days 13 and 59 in Figure 5.5). Hence, reset events caused by high-energy waves are not captured by the Bermslope model. Although the model obtains a BSS = 0.78 at the end of the recovery which is indicative for "good" predictive skill, the BSS is mostly negative throughout the recovery period. The BSS is calculated throughout the entire recovery period, and is presented in Figure 5.7 in dark gray.

A comparison between the predicted (solid black line) and the observed (dashed black line) subaerial beach volume throughout the recovery period is presented in Figure 5.6, where the dimensionless fall velocity Ω is indicated in beige (left axis).

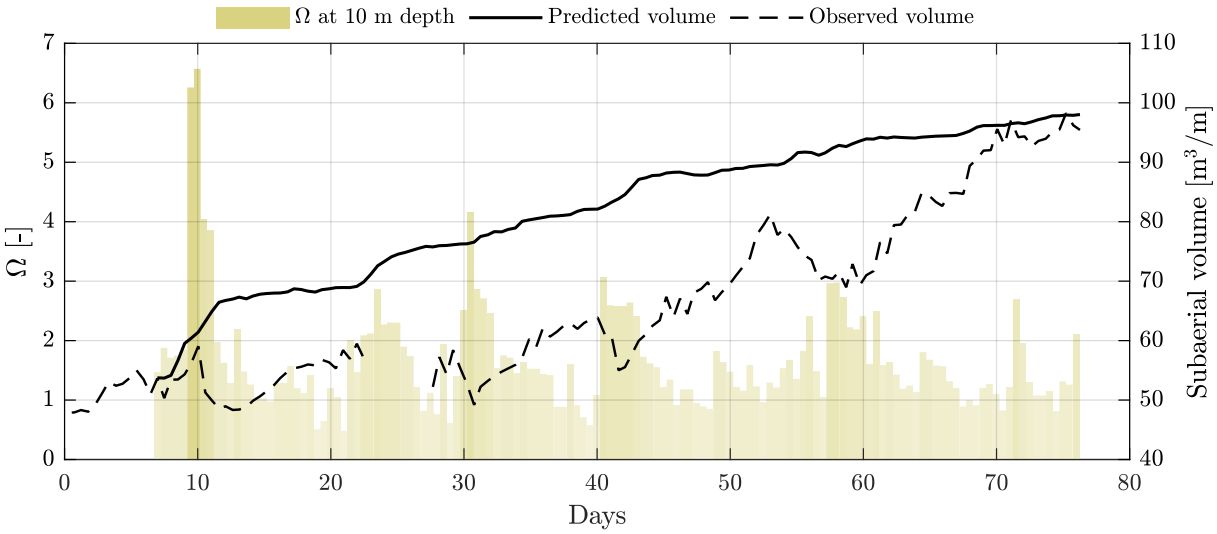

Figure 5.6: The predicted (solid) vs the observed (dashed) subaerial volume change of the berm during the recovery period (right axis). The dimensionless fall velocity Ω (see Equation 2.20) is indicated in beige (left axis).

The total recovery in terms of subaerial beach volume (i.e. after 76 days) is predicted well by the model (Figure 5.6). Throughout the recovery period, however, the predicted subaerial beach volume is persistently much larger than observed. It is striking that during storm conditions (i.e. high Ω values), the predicted subaerial beach volume increases more rapidly than during calm conditions, while the observed subaerial beach volume indicated erosion, and hence reset events are not captured by the model. While the model obtains a RMAE = 0.03 at the end of the recovery, RMAE $\geq$ 0.5 occasionally occurs in the preceding period. The recovery-averaged RMAE = 0.24, indicating poor model skill. The RMAE throughout the entire recovery period is presented in Figure 5.7 in light gray.

The different behavioural modes throughout the recovery period (see Figure 3.6) are classified as explained in Section 3.4.1 (after Phillips et al., 2019). The evolution of the predicted modes is presented in terms of subaerial beach volume change throughout the recovery in Figure 5.8. Throughout the recovery, the dominant mode appears to be Mode 1, and is generally related to gradual subaerial beach volume growth (Figure 5.8). During more energetic conditions, Mode 2 and 3 (vertical growth) are observed, accompanied by rapid volume increase (e.g. day 10).

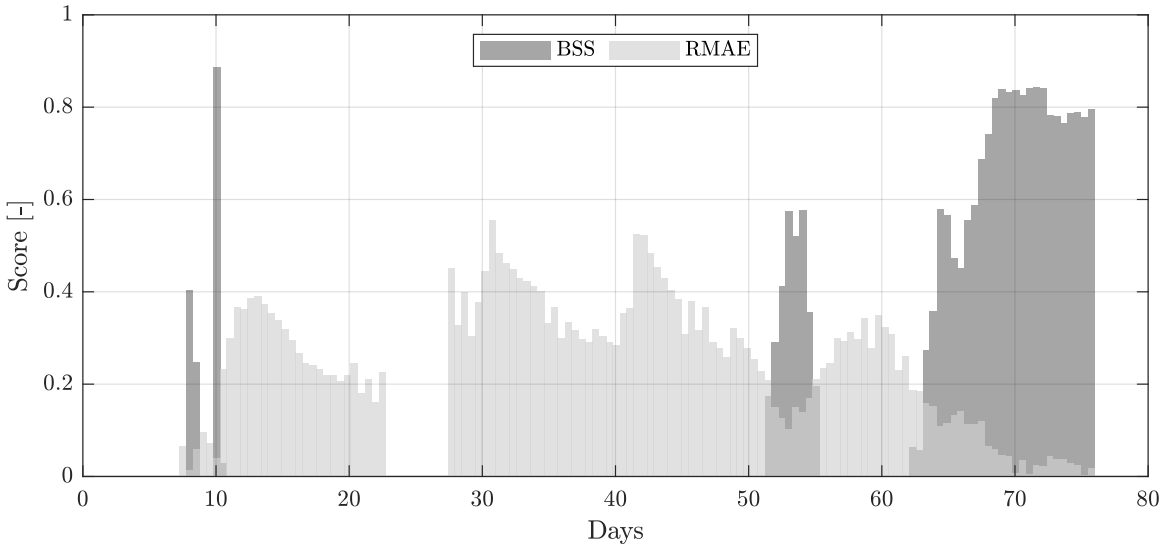

Figure 5.7: The model performance in terms of BSS (dark gray) and RMAE (light gray) throughout the entire recovery period.

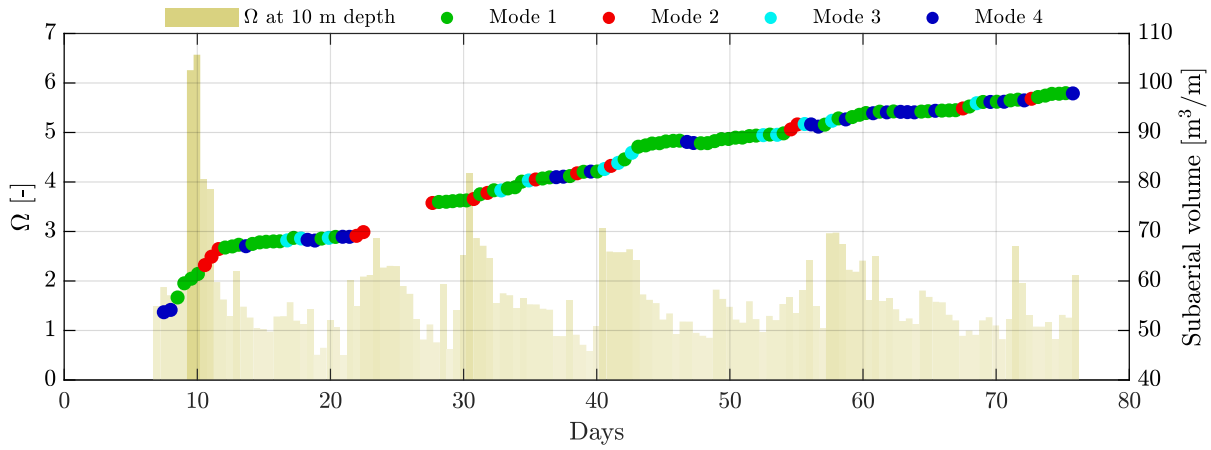

Figure 5.8: The evolution of the four different behavioural modes (as defined in Section 3.4.1) and subaerial beach volume. The dimensionless fall velocity Ω is indicated in beige (left axis).

This evolution of modes is compared to the observed evolution (see Figure 3.8) to assess the model's ability in predicting the correct behavioural mode. For each predicted mode is verified which mode was actually observed, and the model's accuracy is displayed by means of a confusion matrix in Figure 5.9. The predicted modes (left axis) are compared to the observed modes (top axis). The numbers in the shaded panels represent the number of coincidences between predicted and observed modes, and the fractions (between brackets) and shading indicate the accuracy.

Mode 1 is the most frequently, and accurately (62% correct) predicted mode throughout the simulation (Figure 5.9). It was however predicted too frequently (76 times instead of 57 times). Mode 2 is predicted very poorly by the model with only 20% of the instances predicted correctly, and falsely assigned Mode 4 for almost 50% of the time. Also Mode 4 is poorly predicted with only 22% accuracy. Mode 1 and 3 are best represented by the model.

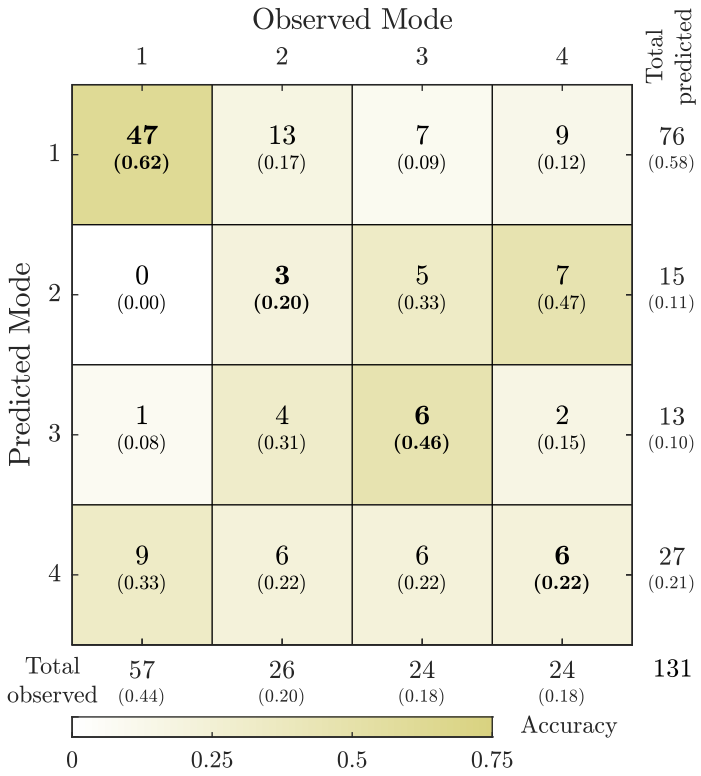

Figure 5.9: Confusion matrix to assess the model's accuracy in assigning the various modes of recovery. The predicted modes (left) are plotted against the observed modes (top). The colours indicate the accuracy (fraction of coincidence).

The runup time-series of the XBeach results were analysed, and compared to the observed runup time-series (measured by the high-frequency Lidar). From the time-series, $Z_{2\%}$ runup heights were determined, and compared in Figure 5.10.

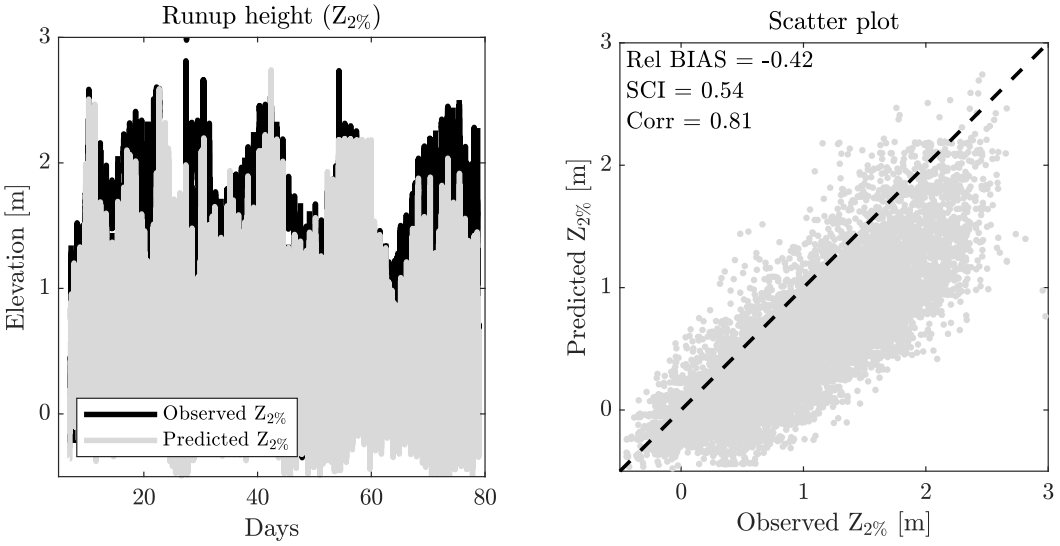

Figure 5.10: The $Z_{2\%}$ runup height predicted by XBeach (gray) is compared to the observed $Z_{2\%}$ runup height (black) in the left figure. The right figure shows a scatter plot.

It appears that the maximum runup height is under-predicted, as well as the amplitude of the swash excursion on the beachface (Figure 5.10). The Rel. BIAS = -0.42, which is the main reason for the under-predicted vertical growth of the berm. Furthermore, there is a very large scatter between the predicted and observed runup height (SCI = 0.54).

5.4.3 Conclusion

The XBeach Bermslope model predicts the post-recovery subaerial beach profile as well as the volume growth well. The shortcoming of the model is however that the observed erosion under energetic conditions is not represented, due to the continuous "correction" of the swash zone sediment transport.

Furthermore, it can be concluded from the results above that the vertical extent of sediment transport (and deposition) is under-estimated in XBeach (i.e. day 76 in Figure 5.5). The predicted vertical growth of the berm is lower than the observed berm height after the recovery. Also the fact that Mode 2 and Mode 3 (both vertical growth of the berm) are not well predicted by the model, indicates that the predicted sediment transport lacks in vertical extent.

5.5 Discussion

The standard XBeach model needs a lot of skewness and asymmetry to ensure sufficient onshore-directed sediment transport and hence subaerial beach volume growth. The beach profile is however very poorly represented by the model. The beachface is much flatter, and the berm, which is characteristic for Narrabeen Beach, is not predicted by the model. As a consequence, no behavioural modes could be defined, and the model results indicate that this model is not applicable to beach recovery (modelling) studies.

The Bermslope model on the other hand, does a much better job in predicting the post-recovery beach profile, and the total beach recovery in terms of subaerial beach volume. The post-recovery profile is characterised by a steep beachface and matches well with the observations (BSS = 0.78).

However, the shortcoming of the Bermslope model is that the steep slope is present throughout the entire simulation, regardless of the wave conditions. Even during storm conditions, the slope is steep ($\sim 1/4$), and the model predicts accretion instead of erosion. This asks for modification of the current Bermslope model formulation. The response of the beachface to storm conditions could be improved by introducing a certain wave-dependency of (the magnitude of) the sediment transport correction carried out by the Bermslope model.

Furthermore, the predicted vertical growth of the berm is lower than the actual observed growth (Figure 5.5). This is likely to be the consequence of using the surfbeat approach, where the wave groups are resolved, but not the individual short waves. Therefore, the incident band runup is not accounted for, which is dominant over infragravity wave runup on reflective beaches (e.g. Wright et al., 1979). This highlights the need for additional model development in order to take into account incident band swash-induced sediment transport in the upper swash zone, which is not resolved in XBeach Surfbeat.

These two major shortcomings of the model are addressed in the next chapter, where two model innovations will be discussed.

Chapter 6

Model development

6.1 Introduction

Chapter 5 highlighted the shortcomings of the current model, and stressed the need for additional development of the model. The Bermslope model forces the onshore transport too much during storm conditions, while erosion is observed. Furthermore, the wave runup in XBeach lacks the contribution of incident waves and therefore under-estimates the vertical extend of the deposition (and erosion) of sediment. For modelling storm erosion, this problem is addressed by means of an avalanching module, but this does not solve the issue for the deposition on top of the berm.

Section 6.2 introduces a new formulation of the Bermslope transport model, which allows for erosion during storm conditions, and only teases the profile towards a certain prescribed slope during calm, accretive conditions. The results of this model are presented in Section 6.3. Next, Section 6.4 describes how short wave runup is determined using an empirical formulation, and proposes a method to re-distribute sediment over the upper swash zone. The results of this swash zone sediment transport model are presented in Section 6.5.

6.2 Wave-dependent Bermslope

The Bermslope module (discussed in Section 4.2.4) is implemented in order to be able to simulate berm growth, and tries to force the beach slope towards a certain prescribed value by adjusting the sediment transport based on the deviation from this prescribed slope:

$$q_{bermslope,x} = f_{bermslope} \underbrace{c^u \, v_{mag}^u \, h^u}_{|q|} \left(\frac{\mathrm{d}z_b}{\mathrm{d}x} - bermslope \right) \tag{6.1}$$

Where $f_{bermslope}$ is a calibration factor, c the sediment concentration, v_{mag} the velocity magnitude, h the water depth, $|q|$ is the sediment transport magnitude and $bermslope$ the prescribed equilibrium (target) swash slope.

While Section 5.4 shows that the Bermslope model predicts the post-recovery beach profile, as well as the total subaerial beach volume growth, the model should also be able to predict erosion during storm conditions. For example, the storm conditions around day 10 result in approximately 10 m^3/m erosion of the subaerial beach (Figure 5.6) and a flatter beach profile (see Figure 5.5, day 13) which is not represented by the model.

From Equation 6.1 becomes evident that the magnitude of the sediment transport correction in the swash zone is a direct function of the sediment concentration c, which is considerably higher during energetic conditions. As a consequence, the onshore-favouring transport correction becomes stronger for more energetic conditions, while in the beachface is in fact eroding. This asks for a modification of the formulation to allow erosion during storm conditions.

6.2.1 Introducing wave-dependency

The first approach was to develop a formulation for the equilibrium beach slope as a function of the (antecedent) wave conditions. A thorough calibration process, however, did not lead to a model that was capable of predicting the beach slope to a reasonable extent throughout the entire content of the data set. Hence, another approach was required to improve the applicability of the Bermslope model.

Rather than deriving an expression for the beach slope as a function of the (antecedent) wave/tide conditions, a response factor is introduced that depends on the wave conditions and allows for erosion during energetic conditions.

Section 2.6 introduced the concept of morphodynamic beach states (Wright and Short, 1984). Reflective beaches ($\Omega \leq 1$) are characterised by a steep beachface, an abundance of sediment and low wave energy. Dissipative beaches ($\Omega \geq 6$) on the other hand have a very flat slope, little sediment and exist in high-energy wave conditions. Wright and Short (1984) found a relation between the morphodynamic beach state and the dimensionless fall velocity Ω. An equilibrium exists between the beach state and Ω, and deviation from the equilibrium wave conditions leads to a change in beach state (Wright et al., 1985). Hence, an obvious approach is to link the magnitude of the Bermslope sediment transport correction to the dimensionless fall velocity Ω.

During calm (equilibrium) conditions, the model teases the beach slope towards the corresponding prescribed target *bermslope*. However, for increasingly energetic conditions, a certain degree of dis-equilibrium forces morphodynamic change and hence a departure from the equilibrium beach state and slope. The magnitude of the Bermslope sediment transport correction should therefore decay with increasing departure from equilibrium conditions (i.e. when $\Omega \geq \Omega_{eq}$). Looking at Equation 6.1 again, the obvious parameter to account for this dependency is the parameter $f_{bermslope}$, which is in fact a measure for the responsiveness of the sediment transport correction. If this "response factor" would decrease with increasing wave energy, it would represent the decay in sediment transport correction during storm conditions.

6.2.2 Formulation

To implement this in the Bermslope model formulation, an alternative bermslope factor fac_{BS} is introduced that is dependent on the wave conditions through the dimensionless fall velocity Ω (Dean, 1973, see Equation 2.20). For calm (reflective) conditions (low Ω values) the formulation is as proposed by Roelvink and Costas (2017) (i.e. $fac_{BS} = f_{bermslope}$). For (extreme) storm conditions (high Ω values), the transport correction is not performed (i.e. $fac_{BS} = 0$). For intermediate conditions, the value of fac_{BS} decreases progressively as Ω increases.

In this intermediate Ω domain, a sinusoidal decay function is proposed with the following proportionality (Equation 6.2) and boundary conditions (Equation 6.3):

$$fac_{BS} \sim \cos(\alpha\,\Omega_i + \beta) \tag{6.2}$$

$$fac_{BS}(\Omega \leq \Omega_{min}) = f_{bermslope} \qquad \text{and} \qquad fac_{BS}(\Omega \geq \Omega_{max}) = 0 \tag{6.3}$$

Where Ω_{min} defines the threshold value for reflective (accretive) conditions that correspond to the prescribed equilibrium *bermslope*, and Ω_{max} the threshold for storm conditions that correspond to (severe) erosion and profile flattening. After a sequence of algebraic operations, the following expression is derived:

$$\alpha\,\Omega_{min} + \beta = 0, \qquad \alpha\,\Omega_{max} + \beta = \pi \tag{6.4}$$

$$\alpha = \frac{\pi}{\Omega_{max} - \Omega_{min}}, \qquad \beta = \frac{\Omega_{min}\,\pi}{\Omega_{max} - \Omega_{min}} \tag{6.5}$$

$$fac_{BS,i} = \frac{f_{bermslope}}{2}\left[\cos\left(\frac{\Omega_i - \Omega_{min}}{\Omega_{max} - \Omega_{min}}\,\pi\right) + 1\right] \tag{6.6}$$

The effect of this formulation, for a range of values and combinations of Ω_{min} and Ω_{max}, is illustrated in Figure 6.1. The fraction of fac_{BS} relative to $f_{bermslope}$ (on the vertical axis) is a function of the dimensionless fall velocity Ω (on the horizontal axis).

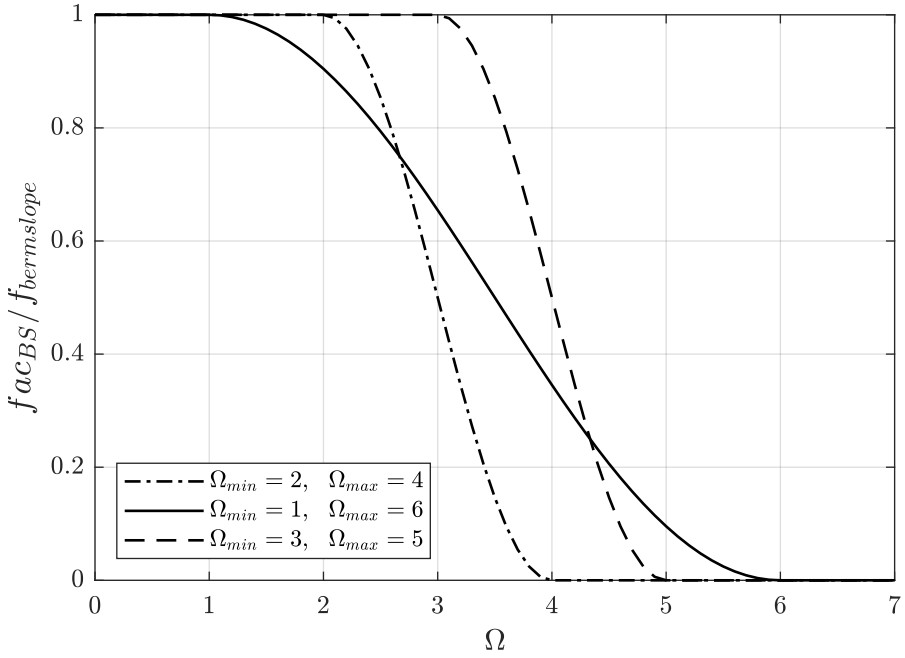

Figure 6.1: Illustration of the sinusoidal decay formulation for the bermslope (or response) factor within the bermslope transport module as a function of Ω. A value of 1 corresponds to the original Bermslope formulation, and a value of 0 corresponds to no Bermslope transport updating.

The dimensionless fall velocity used in this formulation is a weighted average value, determined based on a method similar to Wright et al. (1985). To prevent fast oscillations, first a smoothed value $\overline{\Omega}_i$ is determined, taking into account 600 antecedent numerical time steps ($\sim$ 60 seconds, hence filtering out short wave height variation within a wave group). Then, to account for the asymmetrical response to changing wave conditions (as described in Section 2.6), a second weighted averaging is applied. It is well-known that the morphodynamic beach state rapidly responds to increasing wave energy, but slowly changes back towards a more reflective state under subsequent calm conditions due to the lack of available energy (e.g. Wright and Short, 1984; Wright et al., 1985). In other words, during energetic conditions (high Ω values), morphological change is dependent on prevailing Ω (Lippmann and Holman, 1990), while during calm conditions (low Ω values) the antecedent Ω values are important (Short and Aagaard, 1993), see Section 2.6. This is taken into account by introducing a 5^{th} power weighted average dependency on the antecedent conditions ($D = 9,000$ time steps):

$$\overline{\overline{\Omega}}_i = \left(\frac{\sum_{j=1}^{D} \overline{\Omega}_j^5 \cdot 10^{-j/\phi}}{\sum_{j=1}^{D} 10^{-j/\phi}} \right)^{1/5} \tag{6.7}$$

As a result, when the prevailing Ω significantly increases, the weighted average responds quickly, but also high values of Ω that occurred "long" before, but still within the considered time frame, weigh stronger than more recent low values. The effect of this weighted average formulation is illustrated in Figure 6.2, where the smoothed $\overline{\Omega_i}$ is compared to the weighted average $\overline{\overline{\Omega_i}}$.

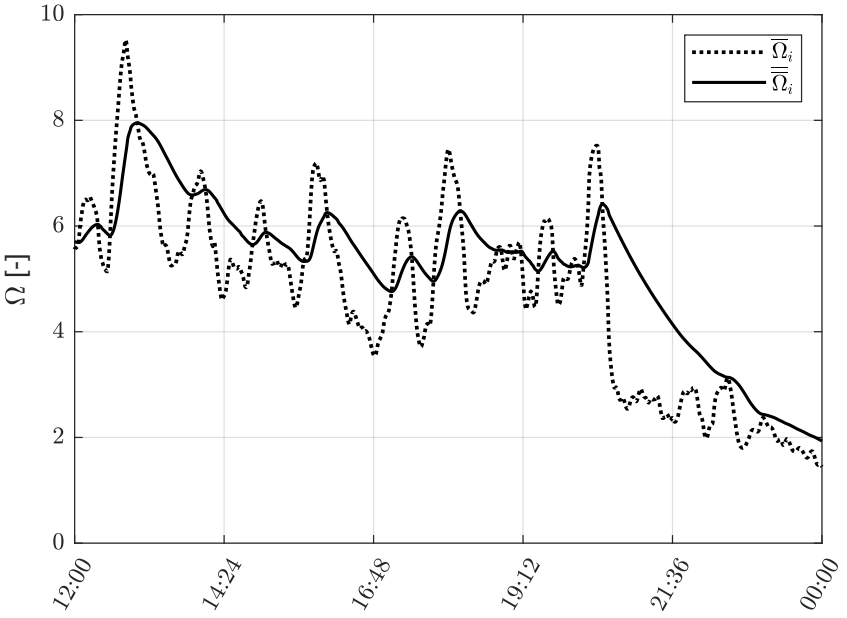

Figure 6.2: Illustration of the difference between the weighted average dimensionless fall velocity formulations $\overline{\Omega}_i$ and $\overline{\overline{\Omega}}_i$ (Equation 6.7).

6.3 Results adapted bermslope formulation

The concept of a wave-dependency of the Bermslope model is described in Section 6.2, and a new Bermslope model formulation was proposed. The implementation of this formulation introduces two new free variables, Ω_{min} and Ω_{max}, which need to be calibrated. Furthermore, the decaying magnitude of the Bermslope transport correction affects the overall onshore sediment transport, and hence the parameters related to this (i.e. f_{Sk}, f_{As}, $bermslope$ and $f_{bermslope}$) need to be fine-tuned again as well. A new model calibration is carried out, of which the final parameter setting and the range of tested values for these parameters are (briefly) presented in Table 6.1. The simulations that are carried out during the model calibration, as well as the full parameter setting are presented in Section B.4.

Parameter		Value		
Symbol	Description	Default	Range	Final
f_{Sk}	Wave skewness factor	0.10	0.20 - 0.30	0.28
f_{As}	Wave asymmetry factor	0.10	0.10 - 0.14	0.13
$Turb$	Turbulence-induced sediment stirring model	BA	-	none
f_{mor}	Morphological acceleration factor	1.0	1.0 - 10	10
$bermslope$	Equilibrium swash slope	0.10	0.24 - 0.28	0.24
$f_{bermslope}$	Calibration factor	15	-	10
Ω_{min}	Threshold Ω value for equilibrium conditions	999	-	2.0
Ω_{max}	Threshold Ω value for storm conditions	999.9	-	4.0

Table 6.1: Overview of the free parameters that are varied during the model calibration of the wave-dependent Bermslope model.

The threshold values $\Omega_{min} = 2.0$ and $\Omega_{max} = 4$ were chosen based on the analysis of (Phillips, 2018), who defined "mild conditions" as $\Omega \leq \Omega_{avg}$ (12-year site averaged Ω) and "storm conditions" as $\Omega \geq 4$ (corresponding to significant wave heights exceeding the 5% exceedance level for a period of at least 12 hours).The implementation of the wave-dependent Bermslope formulation has little effect on the final parameter setting. It does however slightly affect the optimal combination of f_{Sk} and f_{As}, due to the overlap with the sediment transport correction carried out by the Bermslope model in the swash zone.

6.3.1 Results

The predicted profile evolution (solid black line) throughout the recovery period is compared to the observations (dashed black line) in Figure 6.3, where the post-storm (dotted line) and post-recovery (dashed-dotted line) profiles are indicated in gray. The results of the standard Bermslope model are indicated with black dotted lines.

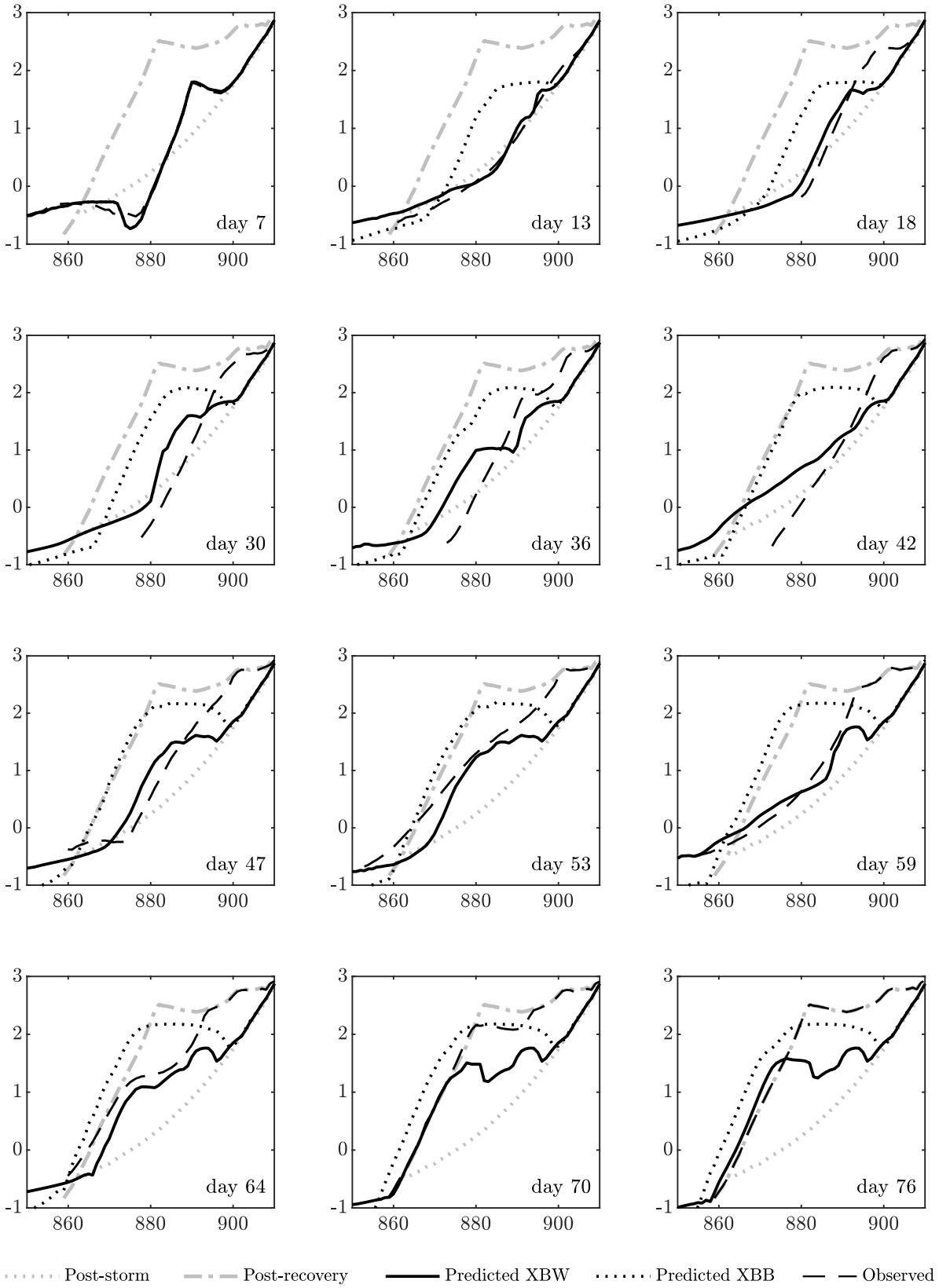

Figure 6.3: Profile evolution predicted by the wave-dependent Bermslope model ("XBW" – solid line) vs the original Bermslope model ("XBB" – dotted line) compared to observations (dashed line). The post-storm and post-recovery profiles are indicated with a gray dotted and dashed-dotted line, respectively.

The wave-dependent Bermslope model predicts the behaviour of the beachface much better compared to the traditional Bermslope formulation (discussed in Section 5.4). The predicted profile evolution (see Figure 6.3) generally follows the observed profiles as it flattens during storm conditions (e.g. day 13) and subsequently becomes steeper during reflective conditions (e.g. day 18). The formation and vertical growth of a secondary berm is also predicted (e.g. days 64, 70, 76). The vertical elevation of the berm grotwh, however, is still under-predicted. At the end of the recovery period, the model obtains a BSS = 0.71, but throughout the recovery period, higher model skill is also accomplished (e.g. BSS = 0.90 around day 13). The BSS is calculated for the entire recovery period, and is illustrated in Figure 6.5 in dark gray.

A comparison between the predicted (solid black line) and the observed (dashed black line) subaerial beach volume throughout the recovery period is presented in Figure 6.4, accompanied by the dimensionless fall velocity Ω on the left axis in beige, indicating the wave conditions. The results of the standard Bermslope model are indicated with black dotted lines.

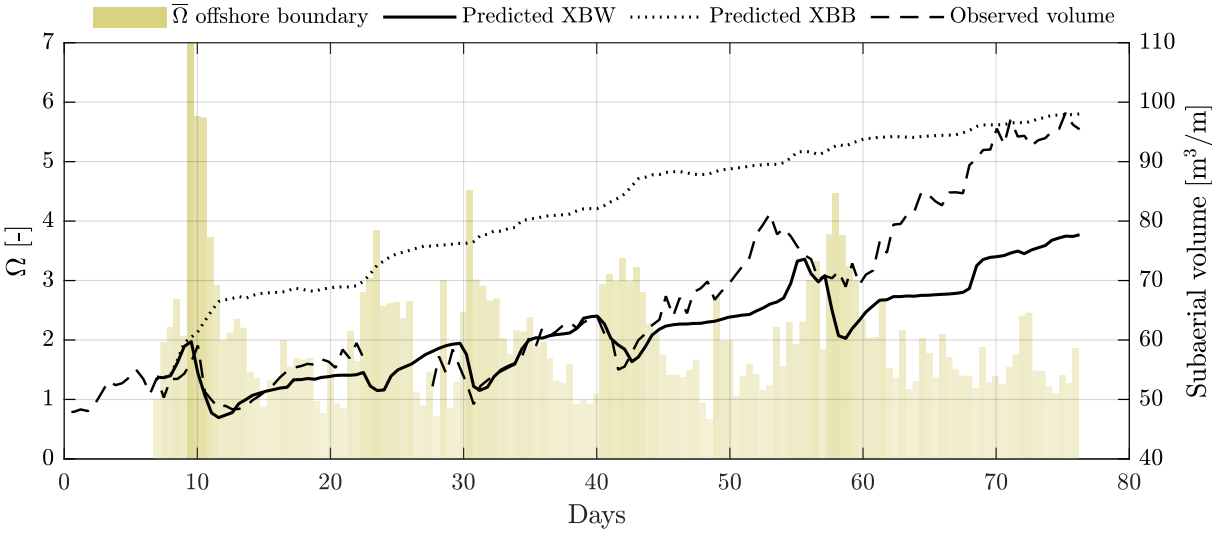

Figure 6.4: Subaerial beach volume predicted by the wave-dependent Bermslope model ("XBW" – solid line) vs the original Bermslope model ("XBB" – dotted line) compared to observations (dashed line). The dimensionless fall velocity Ω is indicated in beige (left axis).

The subaerial beach volume growth throughout the simulated recovery period is predicted well by the model (Figure 6.6), however, the post-storm volume after 76 days is still under-estimated. In contrast to the persistent accretive behaviour of the traditional Bermslope model (dotted line), the present model innovation shows a major improvement in predicting the response to energetic conditions (Figure 6.4). During calm conditions the subaerial beach volume increases, but during energetic conditions (e.g. around day 10, 30, 43, and 60) the model predicts subaerial beach erosion in the same order as the observations. During the first 50 days within the recovery, the model attains a RMAE $\leq$ 0.10, but due to the lack of vertical berm growth this increases towards RMAE = 0.19 towards the end of the simulation. The recovery-averaged RMAE = 0.09, indicating reasonable model skill. The RMAE is presented in Figure 6.5 in light gray for the entire recovery period.

The different behavioural modes throughout the recovery period (see Figure 3.6) are classified as explained in Section 3.4.1 (after Phillips et al., 2019). The evolution of the predicted modes is presented in terms of subaerial beach volume change throughout the recovery period in Figure 6.6. The dimensionless fall velocity Ω is indicated in beige (left axis).

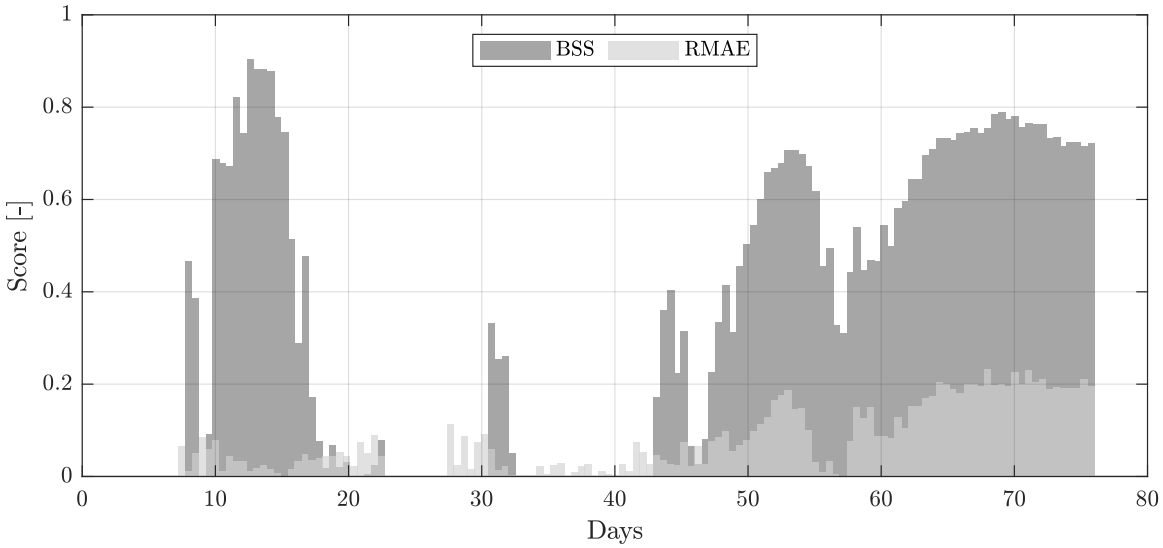

Figure 6.5: The model performance in terms of BSS (dark gray) and RMAE (light gray) throughout the entire recovery period.

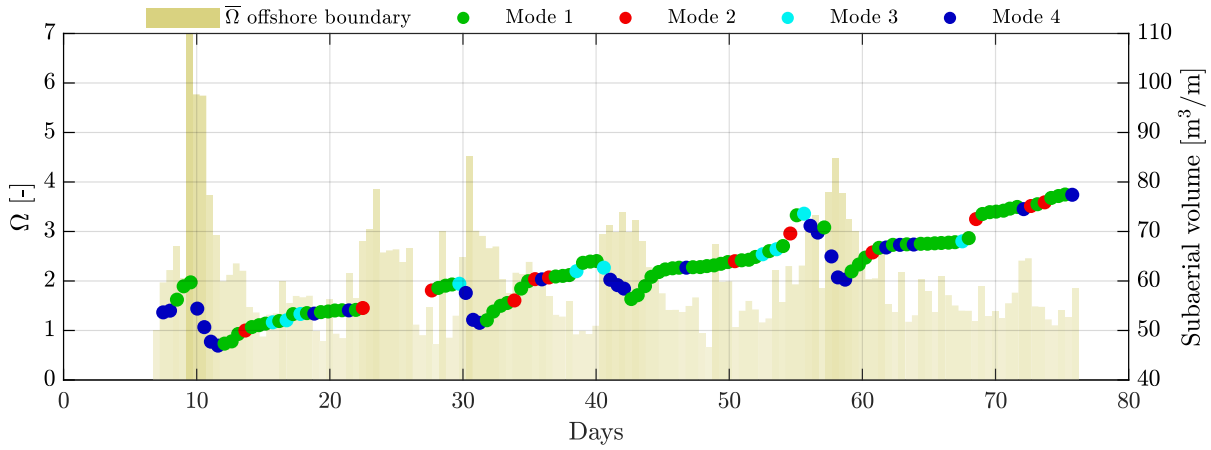

Figure 6.6: The evolution of the four different behavioural modes (as defined in Section 3.4.1) and subaerial beach volume. The dimensionless fall velocity Ω is indicated in beige (left axis).

The evolution of behavioural modes (Figure 6.6) displays that only Mode 4 is assigned during periods of erosion. Although Mode 3 is also defined as beachface erosion, the net volume change appears to be positive (i.e. vertical berm growth compensates for beachface erosion). Mode 3 and 4 are both predicted during energetic conditions, which agrees with observations (Section 3.4.1).

This evolution of modes is compared to the observed evolution (see Figure 3.8) to assess the model's ability in predicting the correct behavioural mode. The model's accuracy in predicting the observed mode is presented by means of a confusion matrix in Figure 6.7.

Mode 1 is again dominant throughout the recovery period, and is predicted 81 times, which is nearly twice as frequently as observed. Despite this over-estimated classification of Mode 1, the confusion matrix shows that the wave-dependent Bermslope model reasonably predicts the various observed modes, since the diagonal contains the highest fractions (Figure 6.7).

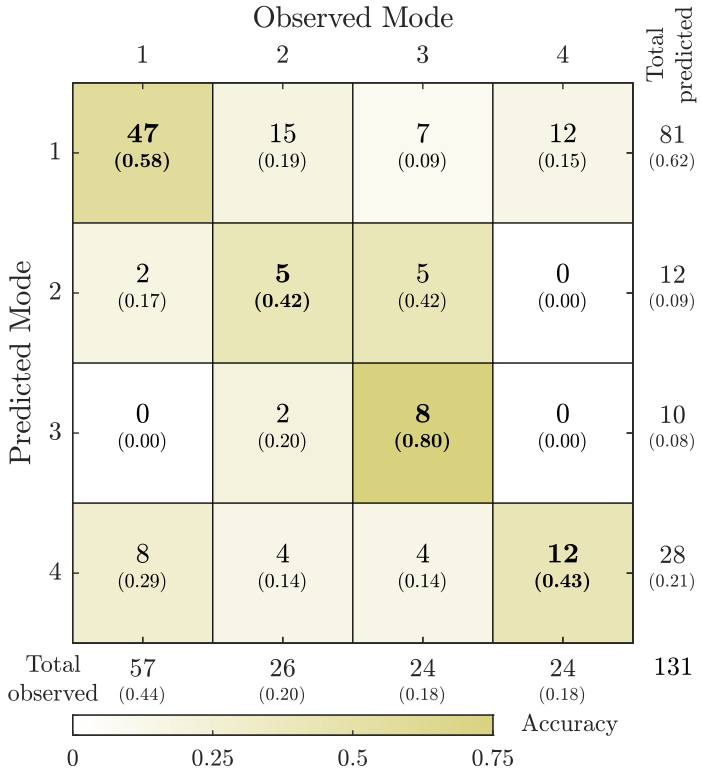

Figure 6.7: Confusion matrix to assess the model's accuracy in assigning the various modes of recovery. The predicted modes (left) are plotted against the observed modes (top). The colours indicate the accuracy (fraction of coincidence).

This means that for each predicted mode, the largest fraction was assigned correctly to the observed mode. Modes 2 and 3 are predicted less frequently than observed (less than half of the observed instances), however, especially for Mode 3, the model was very accurate when it was assigned (80% predicted correct).

6.3.2 Conclusion

The post-recovery profile predicted by the wave-dependent Bermslope model shows good agreement with the observed post-recovery profile (BSS = 0.71). The response to episodic energetic conditions is well represented by the model – in terms of profile evolution (occasionally BSS $\geq$ 0.8) as well as subaerial beach volume (average RMAE = 0.09). Under more energetic conditions, the model predicts erosion of the subaerial beach and profile flattening, followed by accretion and profile steepening under subsequent calm conditions.

This improved "behaviour" of the beach also improved the model's capability in predicting the modes of beach recovery (see Section 3.4.1). Each predicted mode was predominantly assigned correctly to the observed mode.

However, despite the major improvements of introducing a wave-dependency in the Bermslope formulation, the vertical growth is still under-estimated. This results in a under-predicted vertical berm growth, and post-recovery subaerial beach volume that is 20% less than observed. The sediment is distributed over a limited vertical range due to the limited runup height, and

therefore tends to over-predict the horizontal progradation of the beachface. To minimise the inaccuracy with respect to the shoreline position, the predicted subaerial beach volume is inevitably less than observed.

This lack of vertical extent of the wave runup is also directly related to the under-predicted Mode 2 and Mode 3 classification. Due to the limited elevation of sediment transport, sediment deposition does not exceed the berm crest, and hence beachface progradation (Mode 1) is predicted frequently instead of Mode 2 or Mode 3.

This shortcoming with respect to the under-predicted wave runup was identified already in Section 5.4. This shortcoming will be addressed in Section 6.4, where a model innovation is introduced that re-distributes the sediment transport in the upper swash zone, to account for the incident band swash-induced sediment transport, which is not resolved in Surfbeat mode, since infragravity band motions are resolved.

6.4 Swash zone sediment transport re-distribution

From Chapter 5 it became evident that the standard XBeach model, and the Bermslope model, lacked in vertical extend of the sediment transport. In XBeach Surfbeat, infragravity motions are resolved, and incident band waves are assumed to be dissipated by the time they reach the beachface. While this is valid on dissipative beaches, reflective beaches are dominated by incident band wave energy.

The present section describes the development of a model that uses empirical formulations to calculate the incident band runup height. Subsequently, the sediment transport is re-distributed over the upper swash zone, up to this calculated runup height, to account for incident band swash-induced sediment transport, which is not resolved in XBeach Surfbeat.

6.4.1 Methodology

For the development of the model formulation to improve the sediment redistribution up to the incident wave runup height, the empirical formulation of Stockdon et al. (2006) is used. Furthermore, to develop the formulation in terms of XBeach source code, the high-frequency model output of a simulation is used. The output parameters $z_b(x,t)$ (bed elevation), $\eta(x,t)$ (water level) and $Susg$ (suspended sediment transport rate in u-points) are used.

Stockdon et al. (2006) formulate the runup height ($R_{2\%}$ value) in terms of the wave setup $\langle\eta\rangle$ and the swash excursion S:

$$R = 1.1\left(\langle\eta\rangle + \frac{S}{2}\right) \tag{6.8}$$

Where the wave setup $\langle\eta\rangle$ and swash excursion S are both related to the beach slope β_f and the wave steepness, through the offshore wave height H_0 and wave length L_0. However, no distinction is made between the surf zone slope and the swash slope, while this is believed to be inaccurate, especially with respect to the wave setup. While the beachface and surf zone slope are approximately of the same magnitude on dissipative beaches, intermediate and reflective beaches are characterised by variable bar topography or a concave profile, making the definition of a beach slope very difficult (Holman and Sallenger Jr., 1985; Stockdon et al., 2006).

Holman and Sallenger Jr. (1985) argue that the presence of offshore bars influences the wave setup during low tide, indicating that the surf zone slope affects the setup process. Raubenheimer et al. (2001) state that the wave setup is affected by the surf zone topography due to complex radiation stress gradients, supporting the former hypothesis. Nielsen and Hanslow (1991) acknowledge that the beach slope of the entire surf zone influences the runup distribution. Stockdon et al. (2006) found that their empirical formulation for the wave setup was less accurate during low tide and found a correlation of 0.29, while the overall correlation was around 0.7. Since the beach slope is constant throughout the tidal cycle, whereas the surf zone slope varies considerably, this arguably also indicates that the beach slope is less determining for the wave setup, and indicates the importance of the surf zone slope. Replacing the swash slope by a surf zone slope, however, did not improve their overall predictive skill.

6.4.2 Definition of the beach slope

The approach of Stockdon et al. (2006) is followed and slightly adapted to take into account both the surf zone slope β_{sz} and the swash slope β_{sw} for the calculation of the setup and swash excursion. A distinction is made between the slope that drives the wave setup $\overline{\beta_{\langle\eta\rangle}}$, and the slope that determines the swash excursion $\overline{\beta_S}$. These characteristic slopes are calculated through a weighted average of β_{sz} and β_{sw} for which a weighting factor γ_β is introduced.

The surf zone slope β_{sz} is defined as the average slope of the subaqueous beach, reaching from the 1 m water depth contour (similar to a swash module in Delft3D, personal communication with M. van Ormondt) to the point where bed elevation is equal to the tide (to ensure a stable definition). The swash slope β_{sw} is defined as the average slope of the beach that reaches from the elevation of the tide to the estimated wave setup $\langle\eta\rangle$. The definition of these two slopes are indicated in Figure 6.8, illustrating their variability throughout a tidal cycle.

Following Holman and Sallenger Jr. (1985); Nielsen and Hanslow (1991), the wave runup / swash excursion is assumed to be less affected by the surf zone slope, and is more sensitive to the swash slope β_s. The wave setup, on the other hand, is also affected by the swash slope, but the surf zone slope is assumed to be dominant due to the shoaling process that leads to the wave setup. Hence, the following weighted averaging is applied:

$$\overline{\beta_{\langle\eta\rangle}} = \gamma_\beta\,\beta_{sz} + (1-\gamma_\beta)\beta_s \tag{6.9}$$

$$\overline{\beta_S} = (1-\gamma_\beta)\,\beta_{sz} + \gamma_\beta\beta_s \tag{6.10}$$

Where $\gamma_\beta = 0.75$ is the averaging factor, and $\overline{\beta_{\langle\eta\rangle}}$ and $\overline{\beta_S}$ are the representative beach slopes for the wave setup and swash excursion, respectively.

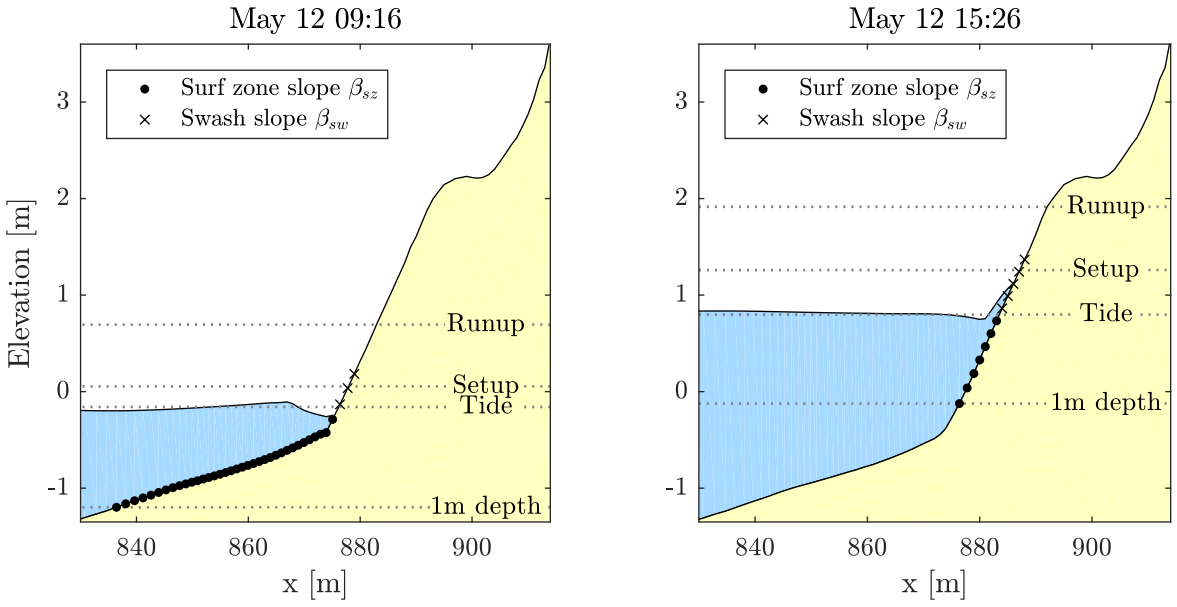

Figure 6.8: The definition of the surf zone slope β_{sz} and swash slope β_{sw} at low tide (left) and hight tide (right). The water level is indicated in gray and the vertical elevations corresponding to the definitions of the slopes are indicated with the dotted lines.

6.4.3 Runup formulation

The wave setup is calculated using Equation 2.12 (Stockdon et al., 2006, Eq. 10), replacing the foreshore slope β_f by the weighted average value $\overline{\beta_{\langle\eta\rangle}}$ (Equation 6.9). Furthermore, since the offshore wavelength is not explicitly calculated in XBeach, the deep water wave length L_0 is expressed in the peak period T_p using the linear dispersion relation (Equation 2.1):

$$\langle\eta\rangle = 0.35\,\overline{\beta_{\langle\eta\rangle}}\sqrt{\frac{H_0\,g\,T_p^2}{2\,\pi}} \tag{6.11}$$

In the same way, the swash excursion S is calculated using Equation 2.17 (Stockdon et al., 2006, Eq. 11-12), replacing β_f by the weighted average swash slope $\overline{\beta_S}$ (Equation 6.10):

$$S = \sqrt{0.563\,\overline{\beta_S}^2 + 0.004}\sqrt{\frac{H_0\,g\,T_p^2}{2\,\pi}} \tag{6.12}$$

H_0 is the offshore wave height, which is defined as a smoothed time-average value (5 times T_p) at the most offshore located grid point. The effect of the adapted formulation is illustrated in Figure 6.9. The $Z_{2\%}$ value of the measured total runup height is calculated, and plotted (horizontal axis) against the predicted $Z_{2\%}$ value (vertical axis) using the original formulation (Stockdon et al., 2006, left) as well as the adapted formulation (right).

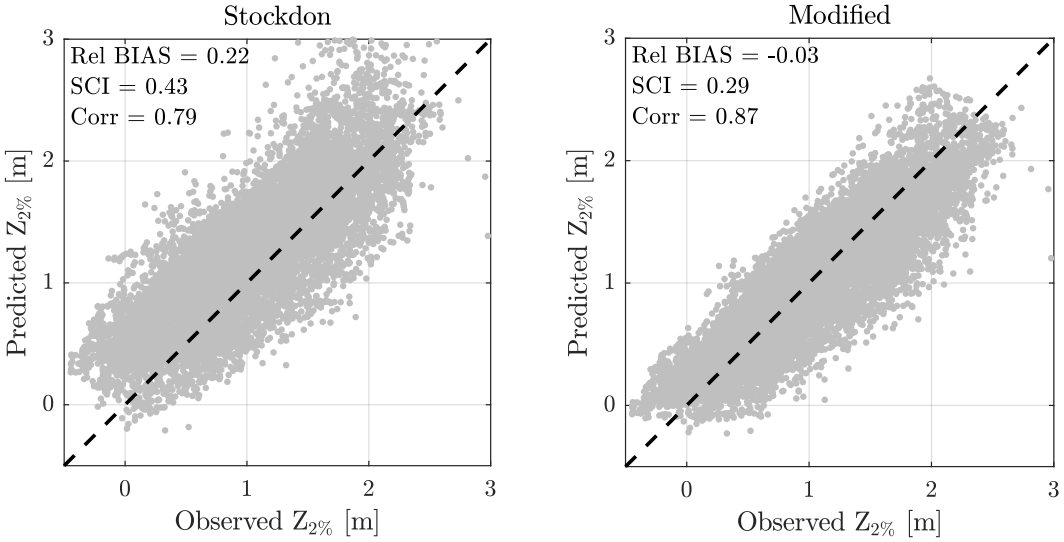

Figure 6.9: A scatter plot illustrating the improved accuracy of the adapted runup formulation (right) with respect to the original formulation (by Stockdon et al., 2006, left).

The adapted formulation improves the overall correlation between the observed and predicted runup height by 8%. Furthermore, the Rel. BIAS reduces from 0.22 to -0.03, and hence resolves the over-estimation of the original formulation. Finally, the SCI significantly reduces from 0.43 to 0.29. It is noted that the constants in the original formulation are not changed, and that the overall flatter slope causes a slight under-estimation (Figure 6.9 – right).

The effect of distinguishing between two characteristic slopes, to calculate setup and swash excursion separately, should be evident during low tide, since this potentially yields a large difference between the surf zone slope β_{sz} and the swash slope β_{sw} (see Figure 6.8). The scatter between the observed and predicted runup height during low tide is presented in Figure 6.10 for the original (left) and the adapted formulation (right).

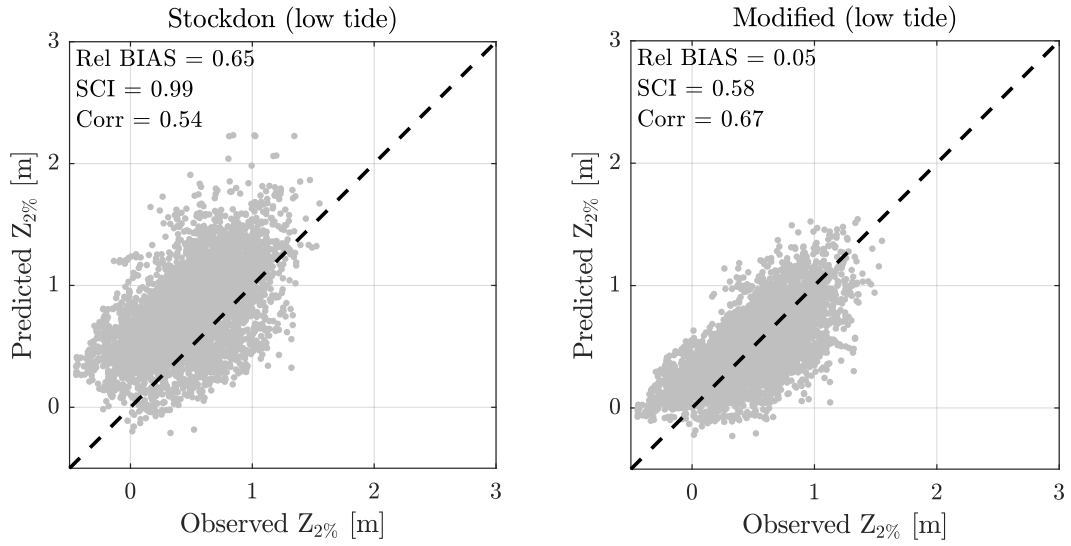

Figure 6.10: A scatter plot illustrating the improved accuracy of the adapted runup formulation (right) with respect to the original formulation (by Stockdon et al., 2006, left) during low tide.

During low tide, the adapted formulation improves the correlation by 13%, and reduces the Rel. BIAS and SCI by 60% and 41% respectively. However, the low tide criterion does not always correspond to a large difference between the surf zone and swash slope (e.g. during neap tide). Therefore, the scatter between the measured and predicted runup height, where $\beta_{sw} \geq 2\,\beta_{sz}$, is presented for the original (left) and adapted formulation (right) in Figure 6.11.

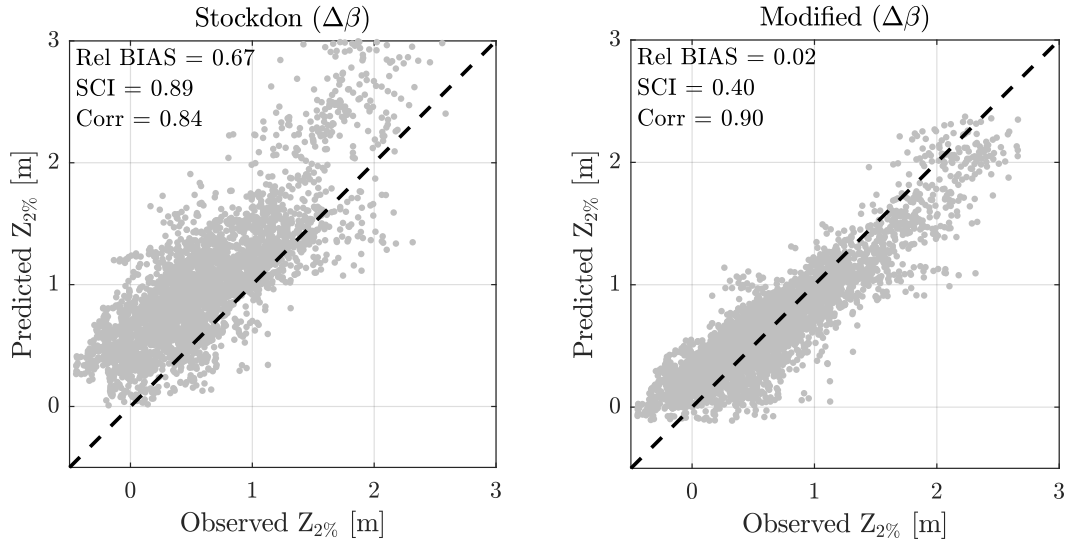

Figure 6.11: A scatter plot illustrating the improved accuracy of the adapted runup formulation (right) with respect to the original formulation (by Stockdon et al., 2006, left) where $\beta_{sw} \geq 2\,\beta_{sz}$.

For all cases where the swash slope is at least twice as steep as the surf zone slope (i.e. where $\beta_{sw} \geq 2\,\beta_{sz}$), the adapted formulation improves the correlation by 6%, and reduces the Rel. BIAS and SCI by 65% and 49% respectively (Figure 6.11). While the original formulation over-predicts the runup height, the adapted formulation shows a much better agreement.

Calibration (amplification) factor

The proposed formulation takes into account the surf zone slope β_{sz}, which is generally much flatter than the foreshore slope β_f (which was used in the original formulation by Stockdon et al., 2006). A thorough calibration of the empirical formulation is beyond the scope of this thesis and is not carried out, and the constants in the expression for the setup and swash excursion are not optimised (i.e. the factors 0.35 in Equation 6.11, and 0.563 and 0.004 in Equation 6.12).

Since these constants are not changed with respect to the original formulation, and the setup and swash excursion are calculated using a milder slope, they tend to be under-estimated (see Figure 6.9). To account for this, a single calibration (or amplification) factor γ_{slope} is introduced:

$$\langle \eta \rangle = 0.35\,\gamma_{slope}\,\overline{\beta_{\langle \eta \rangle}}\,\sqrt{\frac{H_0\,g\,T_p^2}{2\,\pi}} \tag{6.13}$$

$$S = \sqrt{0.563\,(\gamma_{slope}\,\overline{\beta_S})^2 + 0.004}\,\sqrt{\frac{H_0\,g\,T_p^2}{2\,\pi}} \tag{6.14}$$

This amplification factor is implemented in the XBeach model formulation as a free parameter, and can be specified by the user. The effect of this calibration factor on the correlation between the measured and predicted runup height is illustrated in Figure 6.12, where the original adaptation is presented in the left figure, and the inclusion of $\gamma_{slope} = 1.05$ in the right figure.

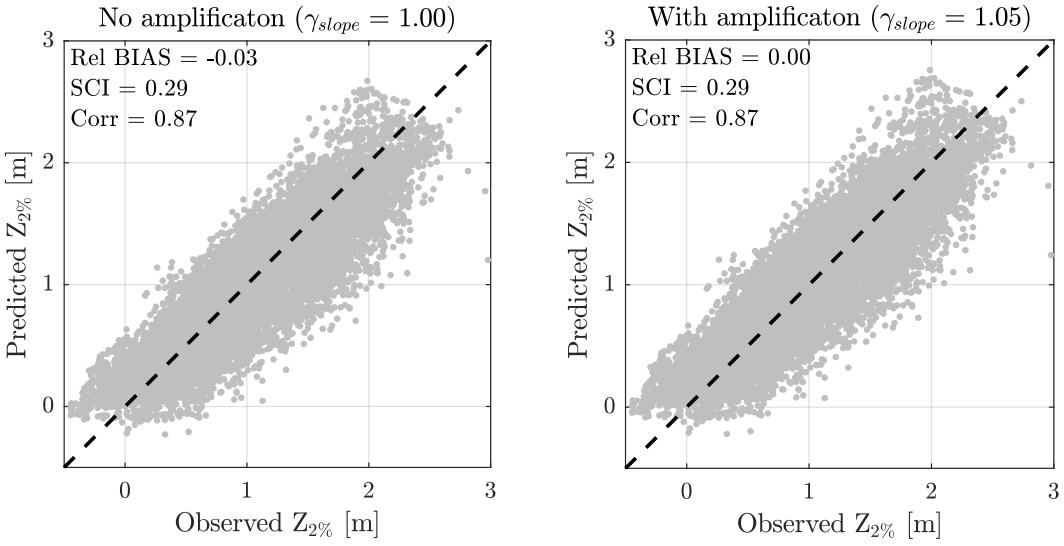

Figure 6.12: A scatter plot illustrating the effect of the introduced amplification factor (γ_{slope} = 1.05), which reduces the Rel. BIAS from -0.03 to 0.00.

The introduction of a calibration factor γ_{slope} potentially increases the scatter (and therefore also the SCI) when $\gamma_{slope} > 1$, and possibly slightly deteriorates the correlation between the measured and predicted runup height (Figure 6.12). However, the runup height is under-predicted to a smaller extent when using $\gamma_{slope} = 1.05$ (Figure 6.12 – right), with respect to no calibration factor (Figure 6.12 – left), and reduces the Rel. BIAS from -0.03 to 0.

The proposed empirical formulation for the total runup height, distinguishing between a setup-affecting slope $\overline{\beta_{\langle\eta\rangle}}$ and a swash-affecting slope $\overline{\beta_S}$, significantly improves the accuracy (Figures 6.9 - 6.11). This illustrates the validity of the hypothesis that the surf zone slope is important for the wave setup as well as the swash excursion (based on e.g. Wright et al., 1982; Holman and Sallenger Jr., 1985; Nielsen and Hanslow, 1991; Raubenheimer et al., 2001).

Now that an empirical formulation is developed, which reasonably predicts the total runup height throughout the entire recovery period, the sediment transport needs to be re-distributed up to this predicted runup height.

6.4.4 Sediment transport re-distribution

Incident band wave runup is not resolved in XBeach Surfbeat. Hence, the sediment transport needs to be re-distributed over the upper swash zone, up to the predicted runup height, to account for incident band swash-induced sediment transport. This section proposes a method to maintain shape of the the sediment transport rate that is calculated by XBeach, and "spread" this shape over the extended runup range, by means of linear interpolation.

The re-distribution of sediment over the upper swash zone is visualised in Figure 6.13, where the black solid line represents the calculated (process-based) sediment transport rate, and the re-distributed sediment transport rate is indicated with the black circles (right axis).

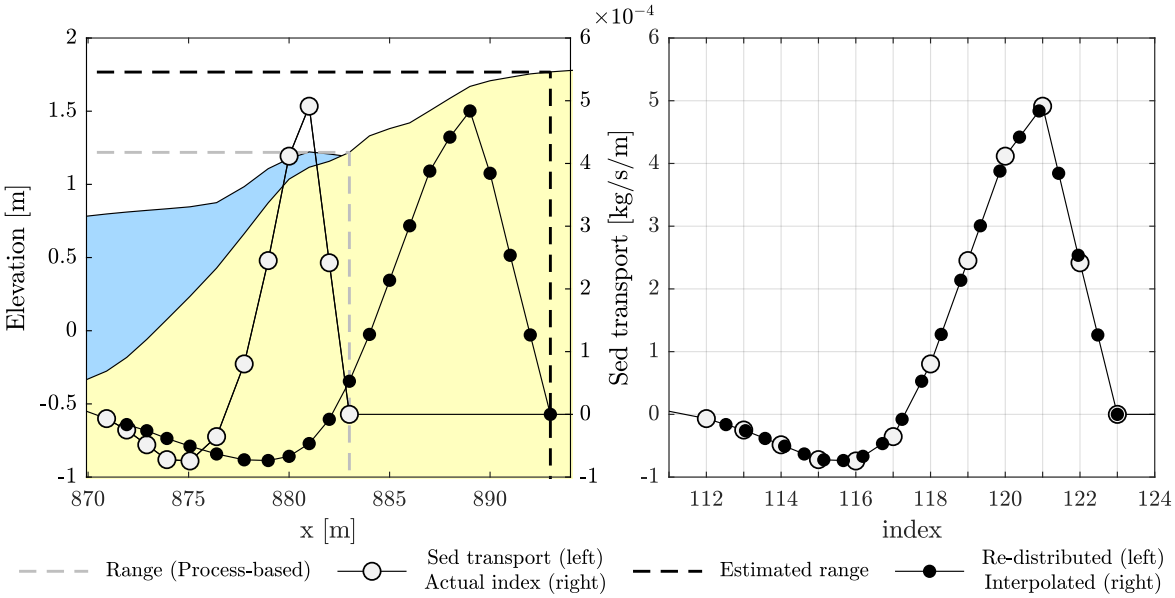

Figure 6.13: Left: Illustration of the re-distribution of the calculated (process-based) sediment transport (gray dots) of which the range is indicated with the gray dashed line. The estimated runup range is indicated with the black dashed line, and the re-distributed sediment transport is indicated with black dots. The interpolation between grid cells is illustrated in the right figure.

The calculated sediment transport rate (process-based), reaching from the 1 m depth contour until the last (landward) cell where sediment transport takes place, is used for the re-distribution over the upper swash zone. The area over which it is re-distributed reaches from the 1 m depth contour until the nearest cell that corresponds to the predicted runup height. The model determines the number of cells that are available for the re-distribution, and then counts the number of cells over which it needs to be spread.

For example, suppose that grid cell `x0` corresponds to the 1 m depth contour, cell `x1` corresponds to the last cell with sediment transport (`Sx`), and cell `x2` corresponds to the predicted total runup height. the model then calculates a linearly interpolated sediment transport rate distribution (`Sxi`) as follows:

```
for j=1:ny
    ...
    if  redistribute_Sx==.true.
        x0 = [...]
        x1 = [...]
        x2 = [...]
        Sxi= Sx
        for i=x0+1:x2
            xi=x0+(i-x0)/(x2-x0)*(x1-x0)
            for ii=x0:x1
                if  ii>xi
                    alpha=ii-xi
                    break
                end
            end
            Sxi(i,j)=(1-alpha)*Sx(ii,j)+alpha*Sx(ii-1,j)
        end
        Sx(x0:x2,j)=Sxi(x0:x2,j)
    end
    -> Bermslope transport correction...
end
```

Where `ny` corresponds to the number of y-cells (although the model in the present thesis is 1D, the formulation is made compatible for 2D simulations as well). `xi` is the intermediate value between two consecutive grid cells, and `alpha` a weighting factor for the linear interpolation to `xi`. After the re-distributed sediment transport rate `Sxi` is calculated, the original sediment transport rate `Sx` is overwritten in the upper swash domain (i.e. from `x0 - x2`).

Mass conservation

It is essential that this re-distribution of the calculated sediment transport does not affect the total amount of sediment erosion or deposition. To illustrate that the described method ensures conservation of mass, consider the volume change in the swash zone ΔV_{swash}, over a period Δt:

$$\frac{\Delta V_{swash}}{\Delta t} = \int_{swash} \frac{\Delta z_b(x)}{\Delta t} \, \mathrm{d}x \tag{6.15}$$

From Equation 4.15 it becomes evident that the bed level change is proportional to the sediment transport rate as follows (in a 1D simulation):

$$\frac{\partial z_b}{\partial t} = -\frac{f_{mor}}{1-p}\frac{\partial q_x}{\partial x} \qquad \Rightarrow \qquad \frac{\Delta V_{swash}}{\Delta t} = -\frac{f_{mor}}{1-p}\int\limits_{swash}\frac{\partial q_x}{\partial x}\,\mathrm{d}x \tag{6.16}$$

Firstly, the linear interpolation between the grid cells to get to the right number of cells does not change the total volume since the distribution of the sediment transport in the swash zone is not affected (the number of interpolated cells scales with the size of the "interpolated grid", see Figure 6.13 – right). Secondly, the subsequent spreading of the interpolated sediment transport shape does not affect the total volume either, because the stretching of Δx reduces the gradient of the sediment distribution shape. Hence, the product of the gradient and the grid size remains unchanged.

In terms of equations, the spreading of the interpolated sediment transport distribution increases the size of the grid cells by a factor r:

$$\Delta x_r = r\,\Delta x_i \qquad \text{with } r = \frac{x_2 - x_0}{x_1 - x_0} \tag{6.17}$$

The subscript r refers to the re-distributed shape, and i refers to the interpolated shape. Since the number of cells remains the same, the gradient of the sediment transport distribution decreases with the same factor r:

$$\frac{\partial q_{x_r}}{\partial x_r} = \frac{1}{r}\frac{\partial q_{x_i}}{\partial x_i} \tag{6.18}$$

Hence, integration of the product of the gradient of the sediment transport distribution and the grid size, over the entire swash zone is not affected by the spreading of the distribution:

$$\int\limits_{swash}\frac{\partial q_{x_r}}{\partial x_r}\,\mathrm{d}x_r = \frac{r}{r}\int\limits_{swash}\frac{\partial q_{x_i}}{\partial x_i}\,\mathrm{d}x_i \tag{6.19}$$

The Bermslope model applies a correction to the sediment transport rate, based on the deviation of the instantaneous swash slope from the prescribed target swash slope *bermslope*. The "corrected" sediment transport rate cannot be used for re-distribution over the upper swash zone, since the correction corresponds to the local deviation from the prescribed *bermslope*. Therefore it is of major importance that the sediment re-distribution is carried out before the Bermslope sediment transport correction is applied, because otherwise this correction might shift to a section higher on the beachface that is not eligible for the correction.

The empirical formulation for the runup height, and the (linear) re-distribution of the sediment transport rate over the upper swash zone are implemented in the XBeach model formulation. The next section discusses the model results, and performance of the proposed model innovation.

6.5 Results

A model development to account for incident band swash-induced sediment transport in the upper swash zone was described in Section 6.4. This proposed model innovation affects the calculated sediment transport rate, from the 1 m depth contour up to the total runup height, which coincides with the region where wave skewness and asymmetry and the Bermslope model affect the sediment transport. Furthermore, a calibration factor γ_{slope} was introduced. Therefore, a new calibration is carried out, of which the final parameter setting and the range of tested values are presented in Table 6.2. The simulations that are carried out during the model calibration, as well as the full parameter setting are presented in Section B.5.

Parameter		Value		
Symbol	Description	Default	Range	Final
f_{Sk}	Wave skewness factor	0.10	0.23 - 0.28	0.24
f_{As}	Wave asymmetry factor	0.10	0.10 - 0.14	0.12
$Turb$	Turbulence-induced sediment stirring model	BA	-	none
$bermslope$	Equilibrium swash slope	0.10	0.24 - 0.27	0.27
$f_{bermslope}$	Calibration factor	15	5 - 10	7.0
Ω_{min}	Threshold Ω value for equilibrium conditions	999	1.5 - 2.0	1.6
Ω_{max}	Threshold Ω value for storm conditions	999.9	4.0 - 5.0	4.5
γ_{slope}	Calibration factor runup height	1.0	1.0 - 1.3	1.25

Table 6.2: Overview of the free parameters that are varied during the model calibration of the swash zone sediment transport re-distribution model.

The threshold values $\Omega_{min} = 1.6$ and $\Omega_{max} = 4.5$ were optimised during the calibration. This "Ω domain" was enlarged to make the transition from equilibrium conditions to storm conditions more gradual. The response factor $f_{bermslope} = 7$ was decreased to make the sediment transport rate correction a bit more subtle, and as a consequence, the target $Bermslope = 0.27$ needed to be a bit steeper to obtain the observed swash slope. As a consequence, $f_{Sk} = 0.24$ and $f_{As} = 0.12$ were optimised again as well. A calibration factor $\gamma_{slope} = 1.25$ was found to give the best result with respect to the vertical growth of the berm.

6.5.1 Results

The predicted profile evolution throughout the recovery period is compared to the observations in Figure 6.14, where the post-storm (dotted line) and post-recovery (dashed-dotted line) profiles are indicated in gray. The results of the wave-dependent Bermslope model are indicated with the black dotted lines.

A comparison between the predicted (solid black line) and the observed (dashed black line) subaerial beach volume throughout the recovery period is presented in Figure 6.15, accompanied by the dimensionless fall velocity Ω on the left axis in beige, indicating the wave conditions. The results of the wave-dependent Bermslope model are again indicated with the black dotted lines.

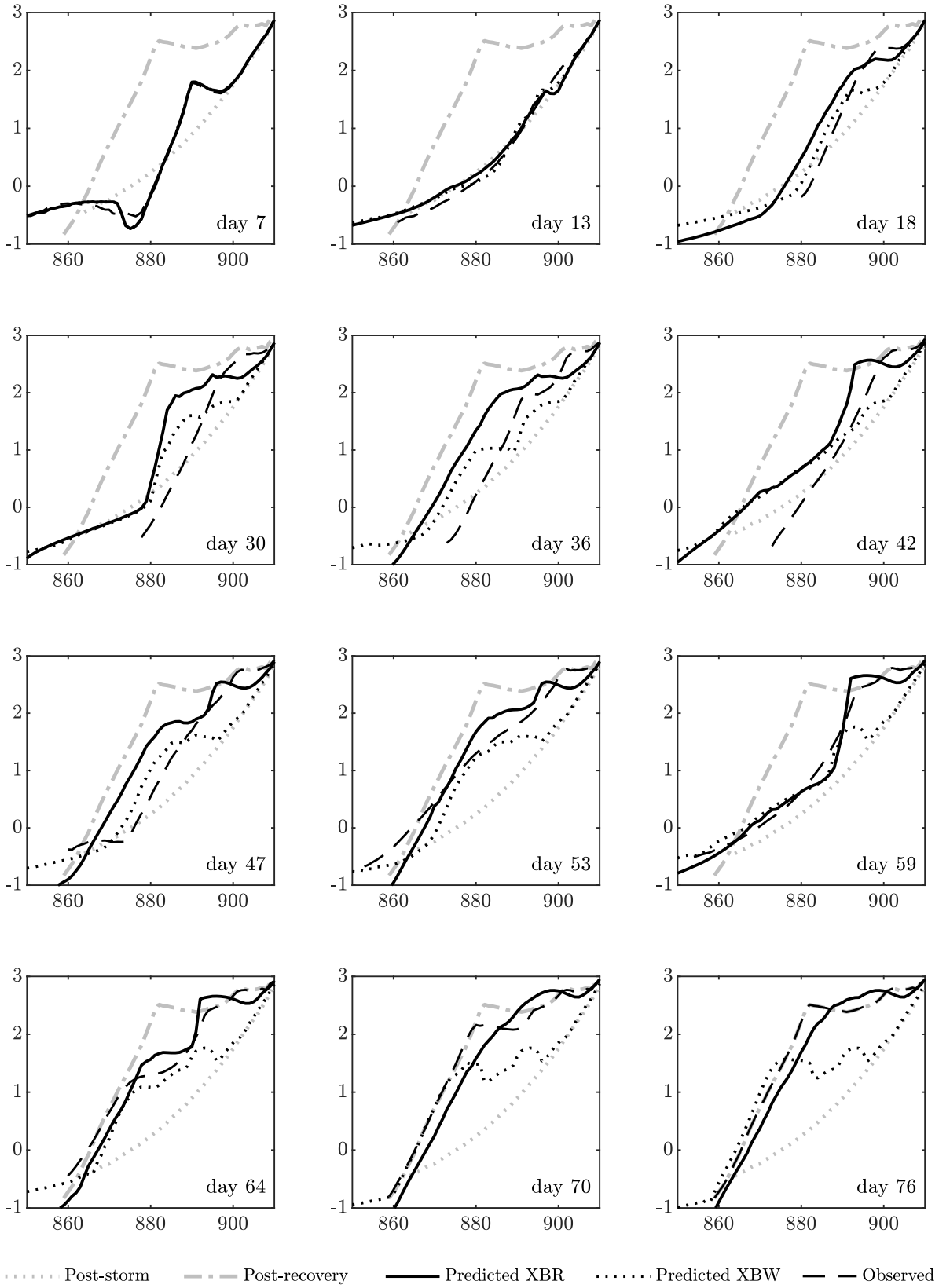

Figure 6.14: Profile evolution predicted by the swash zone sediment re-distribution model ("XBR" – solid line) vs the wave-dependent Bermslope model ("XBW" – dotted line) compared to observations (dashed line). The post-storm and post-recovery profiles are indicated with a gray dotted and dashed-dotted line, respectively.

The final model innovation reasonably predicts the behaviour of the beachface in response to the wave conditions, and the height of the berm growth is represented much better. During storm conditions (e.g. day 13) the berm is eroded and the profile becomes concave and flat. Subsequently, the profile start accreting again during calm conditions (day 18), up to a height which is closer to the observed growth compared to the wave-dependent Bermslope model ("Predicted XBW"). For days 30 - 47, the model performs poorer, and the profile has prograded far too much. However, following more energetic conditions, the profile is eroded again, and the resemblance of the predicted profile improves significantly from day 53 onward. Profile steepening (day 59) followed by the formation of a secondary berm (day 64) is also predicted. At the end of the recovery period, the model obtains a BSS = 0.96, although the skill is significantly poorer throughout the recovery period. The BSS is calculated for the entire recovery period, and presented in Figure 6.16 in dark gray.

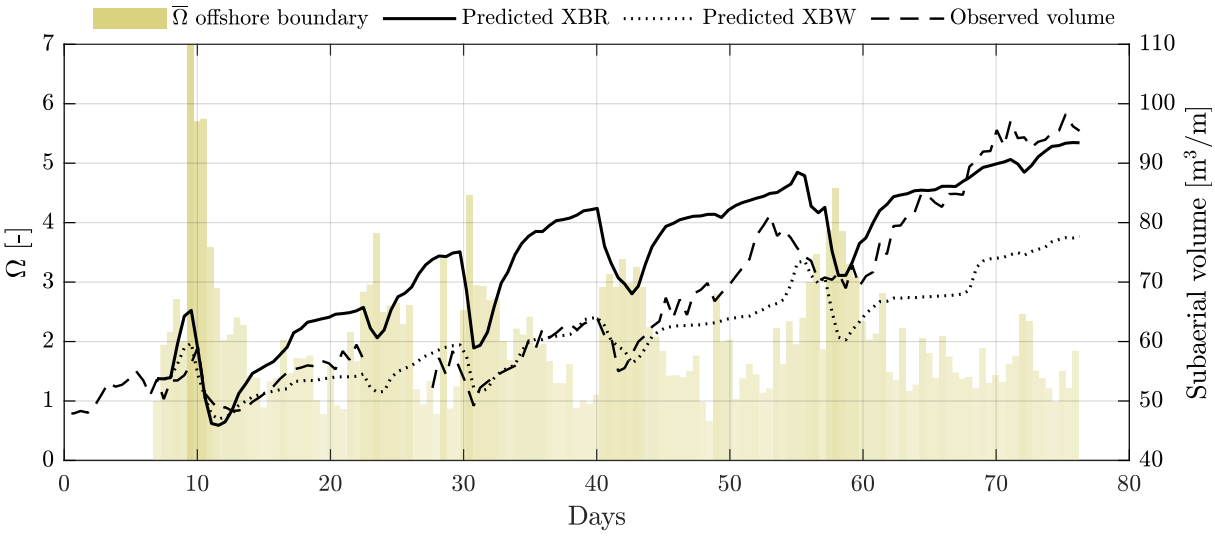

Figure 6.15: Subaerial beach volume predicted by the swash zone sediment re-distribution model ("XBR" – solid line) vs the wave-dependent Bermslope model ("XBW" – dotted line) compared to observations (dashed line). The dimensionless fall velocity Ω is indicated in beige (left axis).

The subaerial beach volume responds very well to the variation in wave conditions. During energetic conditions, the beach is eroded and during subsequent calm conditions, the beach starts to gain sediment again. Where the wave-dependent Bermslope model is more accurate during the first half of the simulation (in terms of RMAE), and lacks the volume growth towards the end of the recovery, the swash transport model over-predicts the growth in the beginning of the simulation (i.e. day 25 - 40 the rate of volume increase is too high) and approaches the observed volume during the second half of the simulation. At the end of the recovery period, the model obtains a RMAE = 0.021, which indicates good model skill. However, high relative errors (RMAE $\geq$ 0.3) are occasionally obtained throughout the recovery period. The simulation-averaged RMAE = 0.13. The RMAE is calculated for the entire recovery period, and presented in Figure 6.16 in light gray.

The different behavioural modes throughout the recovery period (see Figure 3.6) are classified as explained in Section 3.4.1 (after Phillips et al., 2019). The evolution of the predicted modes is presented in terms of subaerial beach volume change throughout the recovery period in Figure 6.17.

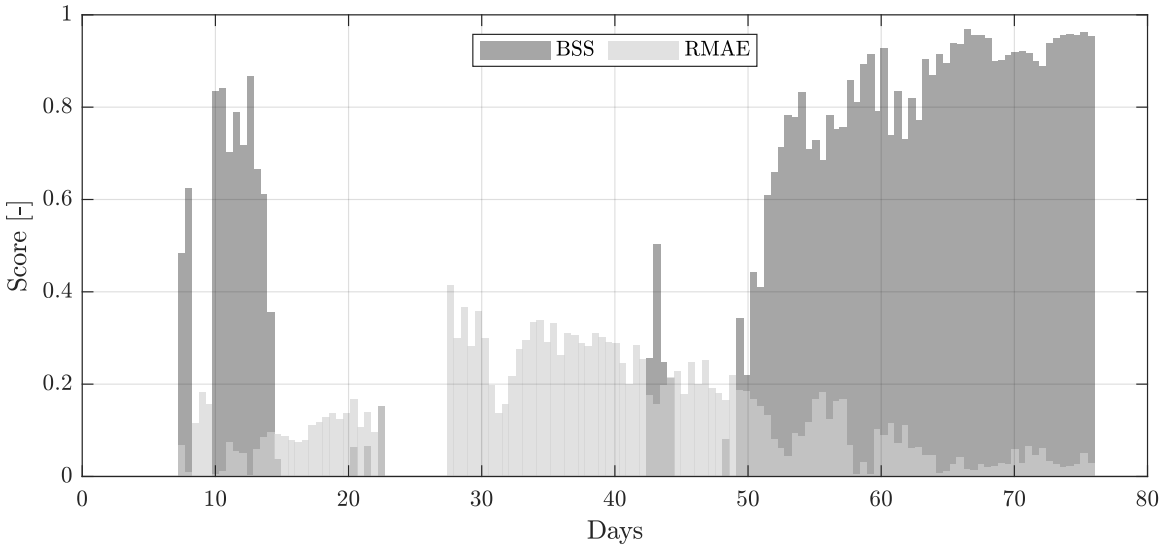

Figure 6.16: The model performance in terms of BSS (dark gray) and RMAE (light gray) throughout the entire recovery period.

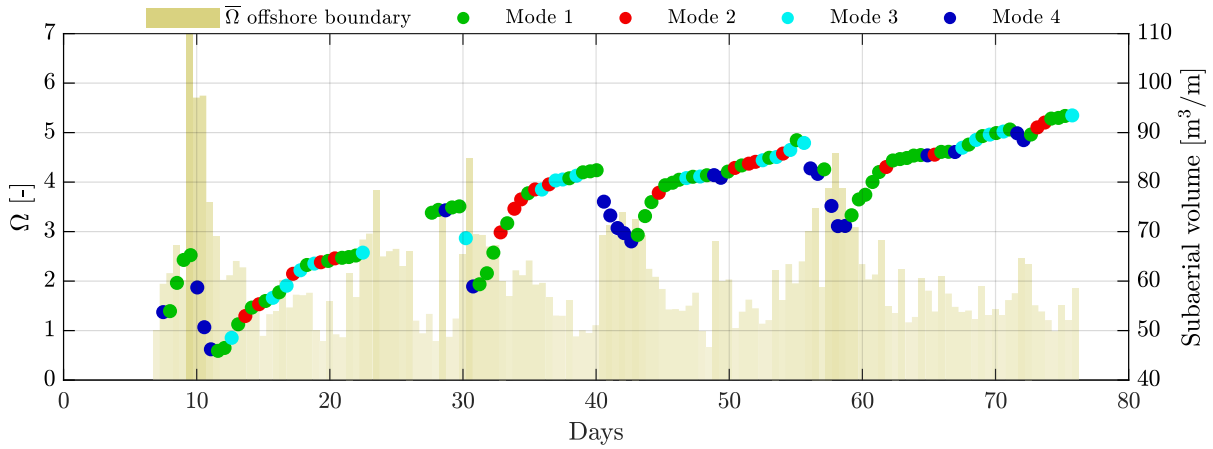

Figure 6.17: The evolution of the four different behavioural modes (as defined in Section 3.4.1) and subaerial beach volume. The dimensionless fall velocity Ω is indicated in beige (left axis).

The evolution of behavioural modes (Figure 6.17) is compared to the observed evolution (see Figure 3.8) to assess the model's ability in predicting the correct behavioural mode. The model's accuracy in assigning predicting the observed mode is presented by means of a confusion matrix in Figure 6.18.

The confusion matrix (Figure 6.18) clearly shows that the predicted behavioural modes are predominantly predicted correctly. Mode 1 is still the dominant mode, and was assigned 50% of the time in model output, while it was assigned 44% of the time in the observed profiles. This also highlights one obvious outlier in the top right block of the confusion matrix. The model incorrectly assigned Mode 1 13 out of 24 times when Mode 4 was actually observed (consider the right column). However, Mode 2 and Mode 3 are predicted significantly better by the model, and are assigned 19 times and 22 times respectively, while the wave-dependent Bermslope model only assigned these modes 12 times and 10 times, respectively, throughout the recovery period.

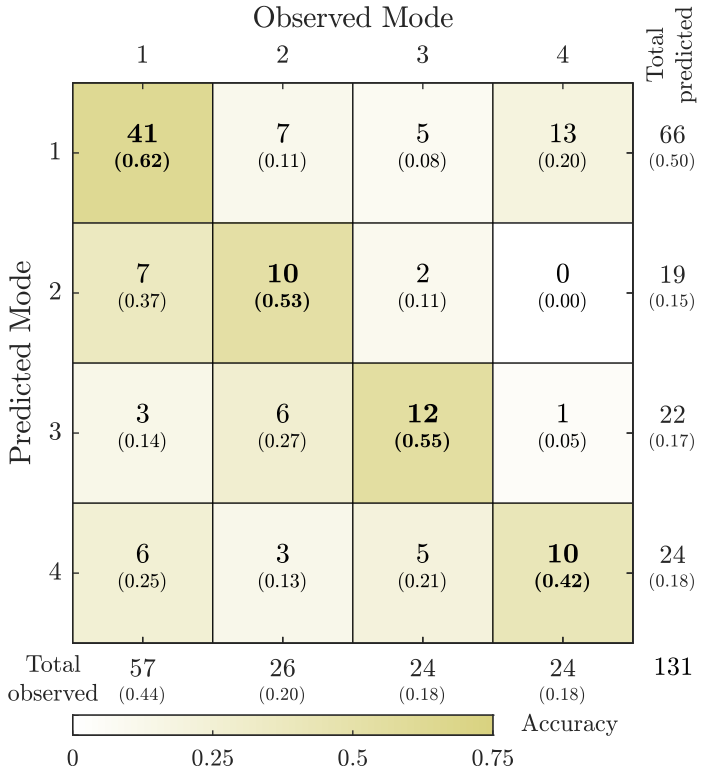

Figure 6.18: Confusion matrix to assess the model's accuracy in assigning the various modes of recovery. The predicted modes (left) are plotted against the observed modes (top). The colours indicate the accuracy (fraction of coincidence).

The $Z_{2\%}$ value of the observed runup height is calculated at the temporal resolution of the XBeach output, and is compared to the predicted runup height (see Section 6.4.3) in Figure 6.19.

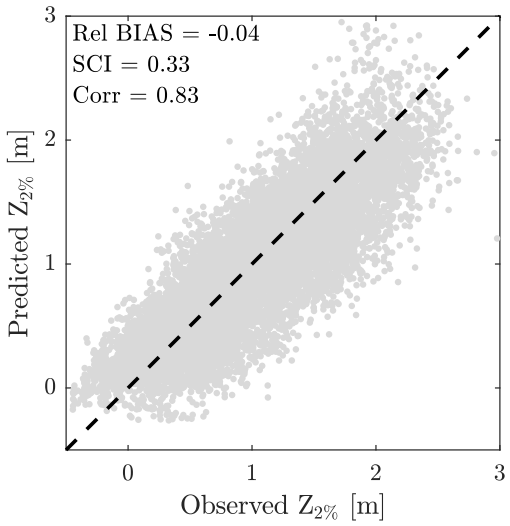

Figure 6.19: A scatter plot illustrating the accuracy of the runup formulation implemented in XBeach. The predicted runup height is retrieved from the XBeach model output.

6.5.2 Discussion

The post-recovery profile predicted by the wave-dependent Bermslope model shows excellent agreement with the observed post-recovery profile (BSS = 0.96) as well as the subaerial beach volume (RMAE = 0.021). The response to episodic energetic conditions is well represented by the model – in terms of profile evolution, as the behavioural modes are frequently assigned correctly. Furthermore, the subaerial beach volume responds well to the episodic short and subsequent calm conditions (average RMAE = 0.13). The formation and vertical growth of secondary berms, that eventually weld to the primary berm are also predicted.

This improved "behaviour" of the beach also improved the model's capability in predicting the modes of beach recovery (see Section 3.4.1). Each predicted mode was predominantly assigned correctly to the observed mode. There is however an obvious outlier: Mode 1 is frequently assigned incorrectly, instead of Mode 4. This is potentially because the model starts to predict accretion too rapidly under calm conditions following (storm) erosion. For example, the model predicts accretion between days 11 - 22, while the observed subaerial beach volume starts to increase approximately 2 days later (Figure 6.15).

6.6 Conclusions

The present chapter described two model innovations. Firstly, the concept of morphodynamic beach states was used to incorporate a wave-dependency in the original Bermslope model formulation, and hence allows for erosion during episodic energetic wave conditions.

Secondly, a model innovation is developed to account for incident band swash-induced sediment transport in the upper swash zone, which is not resolved in XBeach Surfbeat. An empirical formulation is developed (adapted from Stockdon et al., 2006) to estimate the runup height. The adaptation of the formulation significantly improves the accuracy with respect to the original formulation, especially when the gradient of the beachface differs significantly in cross-shore direction.

Subsequently, a method is described to re-distribute the calculated (process-based) swash zone sediment transport up to the estimated runup height, ensuring mass conservation. The innovations improve the predictive skill of the model significantly. The BSS improves from 0.78 to 0.96, and the RMAE decreases from 0.03 to 0.021 after 76 days of simulation. The recovery-averaged RMAE decreases from 0.24 to 0.13. The model is capable of predicting all of the four behavioural modes (as defined by Phillips, 2018, , see Section 3.4.1).

Chapter 7

Model validation

7.1 Introduction

The model results in Chapter 5 indicated the need for additional model development. The model did not capture the response to energetic conditions, and the vertical extent of the berm growth was under-predicted. Chapter 6 proposed and described the development of two model innovations that significantly improve the predictive skill of the model with respect to the behaviour throughout the recovery period, as well as the height of the berm growth.

In the present chapter, the adapted model is applied to a different beach recovery period, following the June 2016 storm at Narrabeen Beach, in order to validate its performance. Initially the exact same parameter settings from the model calibration of the adapted model will be used. Section 7.2 describes the impact of the June 2016 storm event and the subsequent recovery of the subaerial beach. The model setup is briefly described in Section 7.3. Section 7.4 presents the results of the adapted model and Section 7.5 discusses the model performance and sensitivity.

7.2 June 2016 storm and recovery

On June 4th 2016, the Narrabeen Coast was impacted by a severe East Coast Low (ECL), with offshore significant wave heights up to 6.5 m. Although the conditions were less energetic compared to the April 2015 storm, the storm conditions coincided with a winter solstice spring tide (resulting in a 0.44 m higher water level compared to average spring tides), and waves approached the coast from the east during the peak of the storm. Due to this anomalous wave direction, the Long Reef headland provided no sheltering, and the embayment was much more exposed to the waves. This rare combination of circumstances made the June 2016 storm, which lasted approximately 3 days, the most devastating one in the history of Narrabeen Beach. The storm caused a total erosion of 336,600 m^3, corresponding to an embayment-averaged erosion of 93.5 m^3/m (Harley et al., 2017). At the Lidar transect, this resulted in an erosion volume of approximately 75 m^3/m and a shoreline retreat of 35 meters. The effect of the storm on the cross-shore profile at the Lidar transect is illustrated in Figure 7.1 – left.

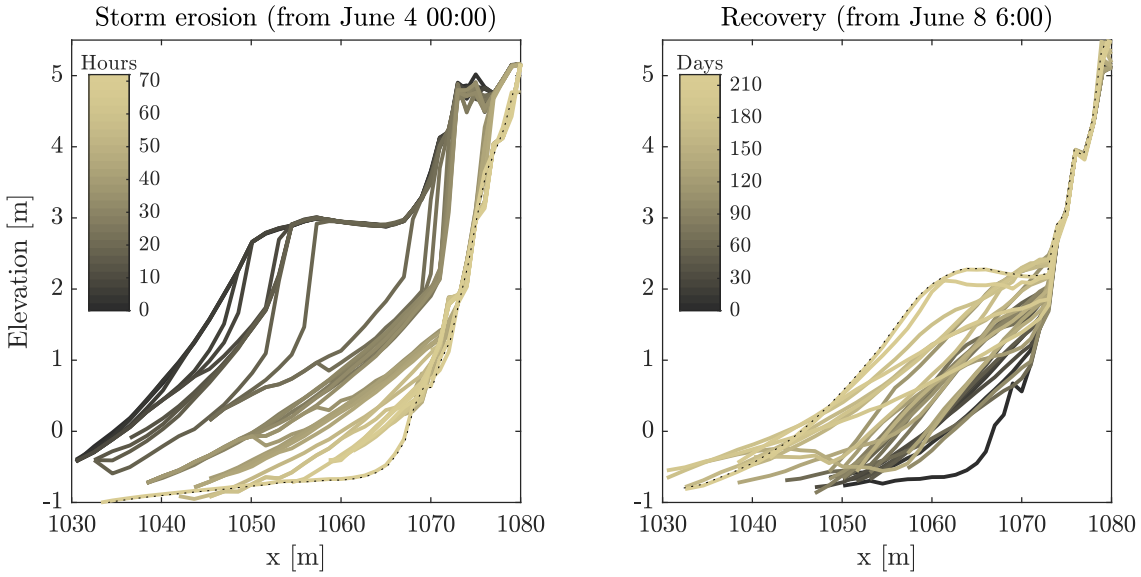

Figure 7.1: The April 2015 storm erosion (left, colours indicate hours after June 4^{th} 00:00) and subsequent recovery (right, colours indicate days after June 8^{th}). The last profile of both figures is indicated with a dotted black line.

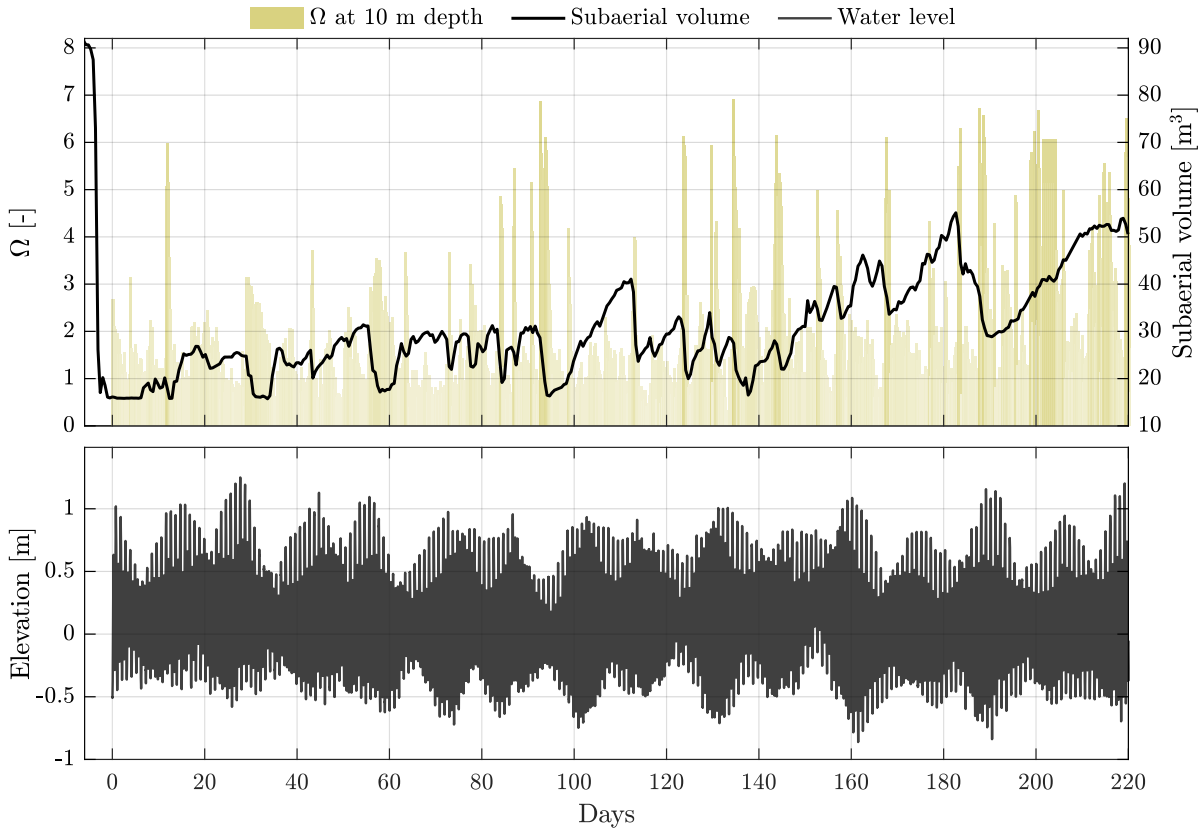

Figure 7.2: Subaerial beach volume development obtained from the low tide profiles (black line, right axis), with the dimensionless fall velocity Ω indicated in beige (left axis). The tide is presented in the lower figure.

Following the June 2016 storm, the subaerial beach profile is recovering towards its pre-storm conditions. However, in contrast to the post-storm recovery in 2015, the recovery following the June 2016 storm takes much longer. The profile evolution throughout the the first 220 days of the recovery is illustrated in Figure 7.1 – right. The subaerial beach volume evolution during the first 220 days following the storm event is presented in Figure 7.2 (right axis), together with the dimensionless fall velocity Ω to indicate the wave conditions (left axis). Additionally, the lower panel shows the astronomical tide for the considered period.

During the first $\sim$ 100 days following the storm, there is no significant accreting trend visible, and the subaerial beach volume remains mostly below 30 m^3/m. Between days 95 - 112 there is a rapid volume increase under calm wave conditions ($\Omega < 2$) and from day 140 onward there is a clear accreting trend. Striking is the relatively high rate of volume increase around day 200, when $\Omega \approx 6$, indicating storm conditions, which normally causes erosion. This is potentially the consequence of the welding of an offshore bar that was formed during the storm. Figure 7.3 shows the post-storm bathymetry, as well as the bathymetries 105 days and 252 days following the onset of recovery.

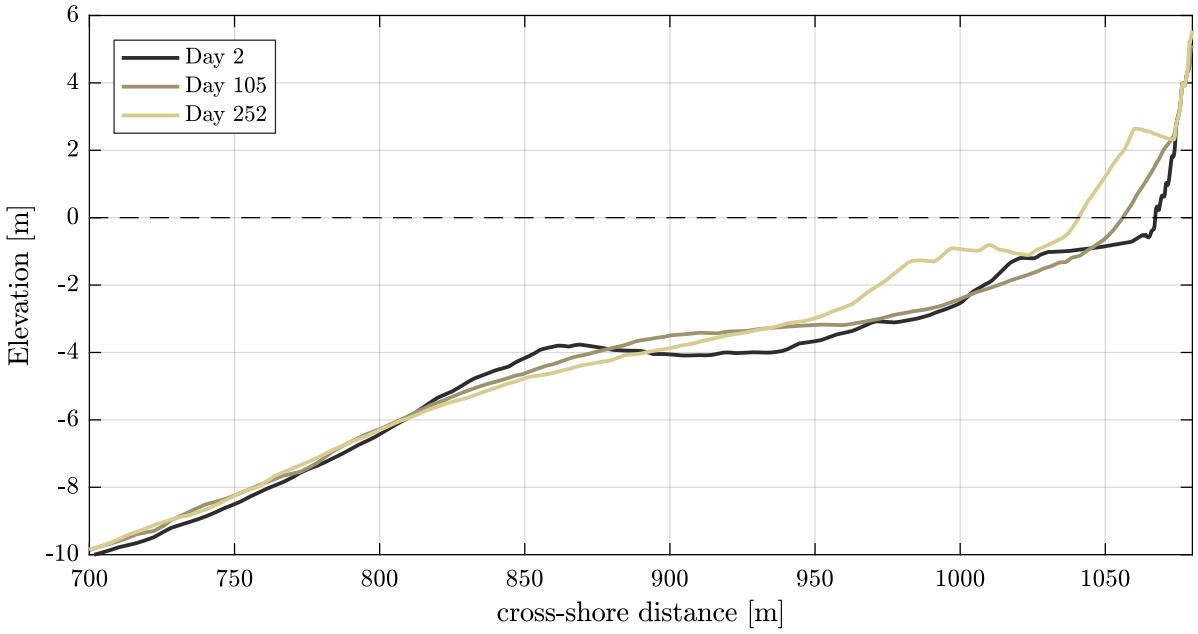

Figure 7.3: The post-storm bathymetry (black), and bathymetries 105 days (brown) and 252 days (beige) following the onset of recovery (relative to June 8th 2016).

During the storm, sediment was eroded from the beach and deposited further offshore as a sand bar, which is transported back onshore subsequently (Figure 7.3). 105 days after the onset of recovery, the offshore sand bar has migrated approximately 100 meters onshore, and after 252 days, the offshore bar has migrated another 150 meters onshore and reached the subaerial beach to form a Longshore Bar-Trough (LBT) profile with a berm. Hence, the offshore bar acts as a sediment source for the subaerial beach.

Besides the sediment supply from the offshore bar, there is also a significant net input of sediment along the transect. After 105 days there is a net volume gain of 100 m^3/m and after 252 days there is 220 m^3/m more sediment with respect to the post-storm profile. This net import of sediment indicates that alongshore sediment transport might be important for the recovery of the subaerial beach following the June 2016 storm.

7.3 Model setup

Just like for the simulation of the recovery following the April 2015 storm (see Section 4.3), a numerical model is set up for the simulation of the recovery following the June 2016 storm. Bathymetry surveys, Lidar data, sediment characteristics and wave and water level data (described in Chapter 3) are used to set up a 1D XBeach model, which requires the following input:

- Initial condition (bathymetry);
- Offshore water level (tide);
- Wave conditions (H_s, T_p and θ_0); and
- Sediment characteristics (i.e. D_{50}).

The initial bed level is constructed by combining the data from a bathymetry survey on June 10$^{\text{th}}$ (approximately two days following the onset of recovery), and the subaerial beach profile measured by the continuously scanning Lidar. This bed level is manually extended up to a water depth of 20 meters, and is presented in Figure 7.4. The right panel shows the subaerial beach in more detail, and the range of the offshore water level (astronomical tide) throughout the simulation is indicated in gray.

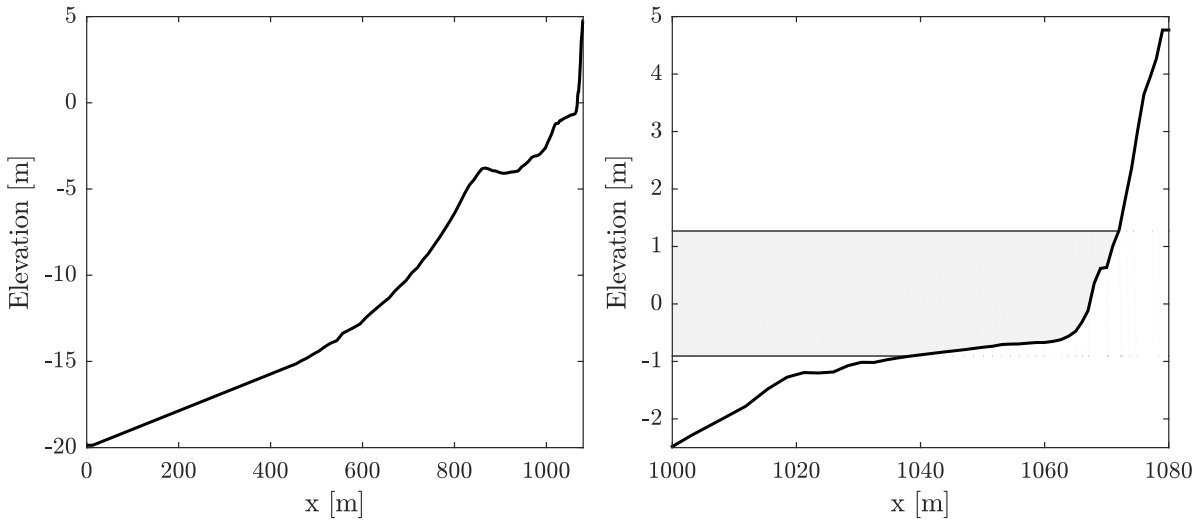

Figure 7.4: Initial condition of the bed level, based on measurements from June 10th 2016. The range of the tide is indicated in gray in the right figure.

Time series are constructed for the wave conditions as well as the water level, and they are both imposed at the offshore boundary of the model (at a water depth of 20 m).

The offshore wave data is again transformed to nearshore wave characteristics using the wave transformation model MIKE21 (DHI, 2014). The offshore waves are presented in Figure 7.5 – left, and the computed nearshore wave conditions are presented in the right panel.

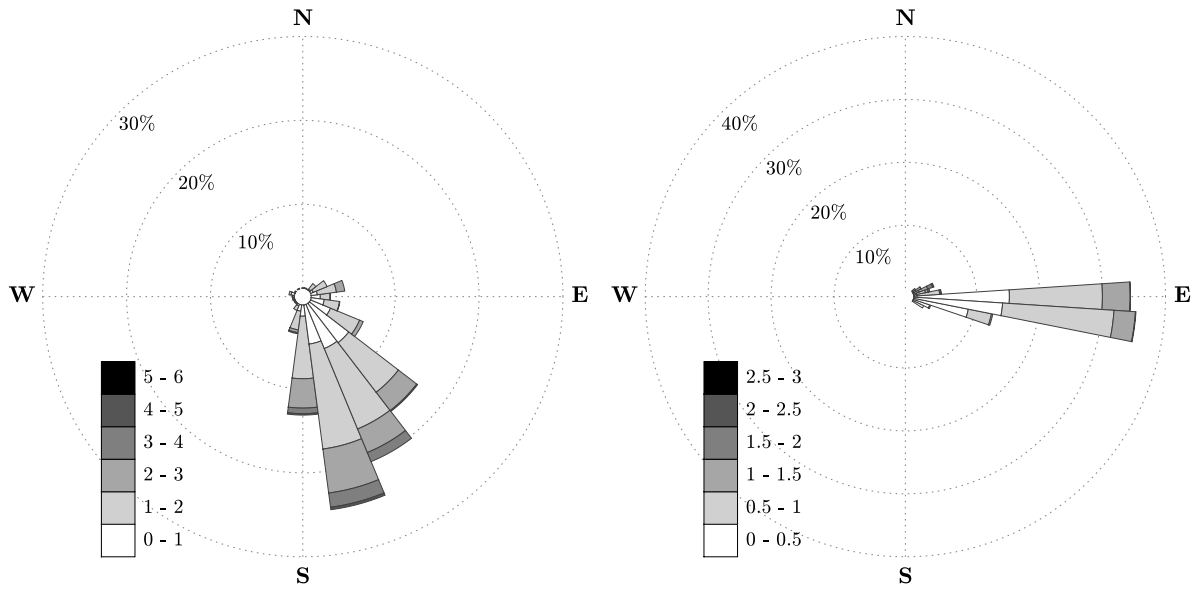

Figure 7.5: Offshore significant wave height and direction (left), obtained from the wave buoy measurements (see Figure 3.1 – left) and calculated nearshore wave height and direction at the 20 m depth contour (right), using a wave transformation model MIKE21 (DHI, 2014)

The sediment characteristics are specified in the input file, by means of a median grain size ($D_{50} = 0.3$ mm). The parameter setting for the model simulation, displaying the most important parameters, is presented in Table 7.1.

Parameter	Description	Value
D_{50}	Grain diameter [m]	0.0003
f_{Sk}	Wave skewness factor	0.24
f_{As}	Wave asymmetry factor	0.12
$Turb$	Turbulence-induced sediment stirring model	WA
$bermslope$	Equilibrium swash slope	0.27
$f_{bermslope}$	Calibration factor	7.0
Ω_{min}	Threshold Ω value for equilibrium conditions	1.6
Ω_{max}	Threshold Ω value for storm conditions	4.5
γ_{slope}	Calibration factor runup height	1.25

Table 7.1: Parameter settings for the simulation of the recovery following the June 2016 storm.

7.4 Model results

The predicted profile evolution throughout the recovery period is compared to the observations in Figure 7.6, where the post-storm (dotted line) and post-recovery (dashed-dotted line) profiles are indicated in gray. The predicted profile is indicated with the solid black line, and the observed profile is indicated by the dashed black line. The profiles are presented approximately 18 days apart throughout the 220 days of simulation.

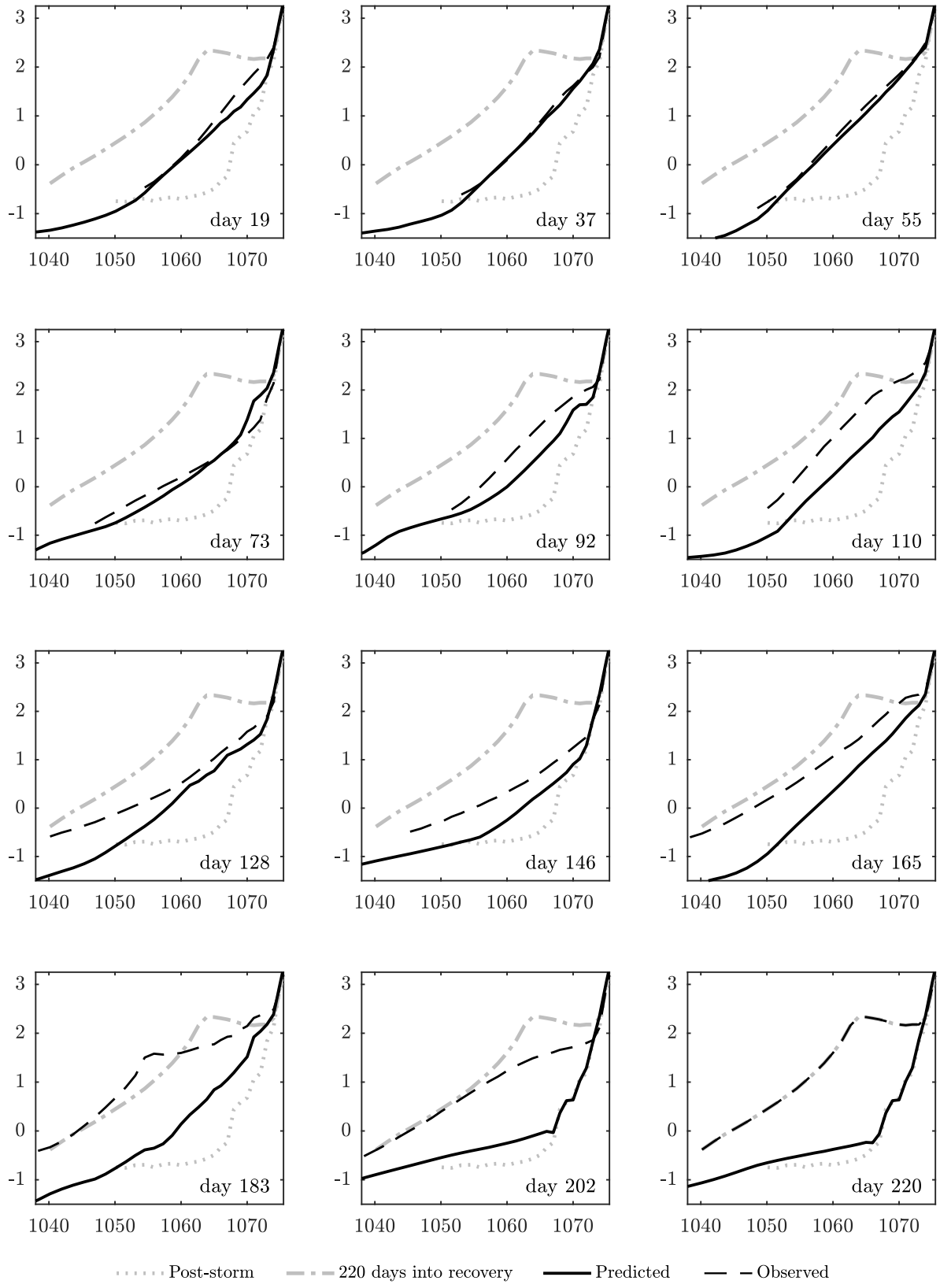

Figure 7.6: The predicted (solid) vs the observed (dashed) profile evolution throughout the first 220 days of the recovery. The post-storm profile is indicated with the dotted gray line, and the profile after 220 days is indicated with a dashed-dotted gray line.

The subaerial beach profile evolution is predicted well by the model during the first 73 days of simulation (Figure 7.6). However, from day 92 onward (i.e. panel 5 - 12 in Figure 7.6), the predicted profile starts to depart significantly from the observations. The model attains a high skill in the beginning of the simulation with a BSS ≥ 0.8 for over 70 % of the time during the first 100 days. Subsequently, the skill drastically deteriorates, and the BSS = 0.13 after 220 days of simulation, indicating poor model skill. The BSS is calculated throughout the entire simulation, and is presented in Figure 7.8 in dark gray.

A comparison between the predicted (solid black line) and the observed (dashed black line) subaerial beach volume throughout the first 220 days of the recovery period is presented in Figure 7.7, accompanied by the dimensionless fall velocity Ω (left axis) in beige, indicating the wave conditions.

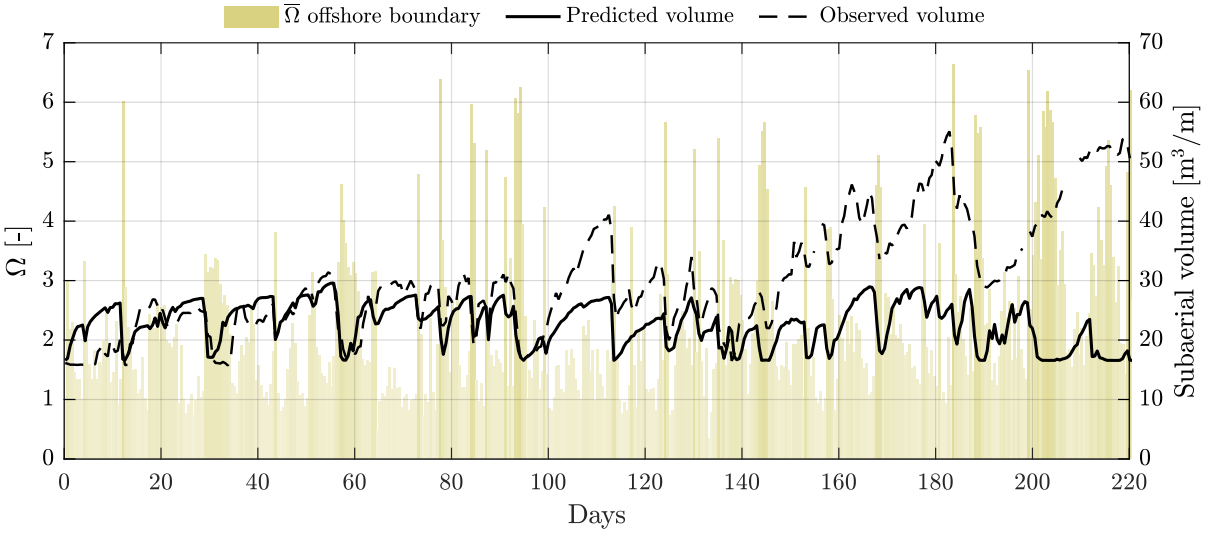

Figure 7.7: The predicted (solid) vs the observed (dashed) subaerial volume change during the first 220 days following the onset of recovery (right axis). The dimensionless fall velocity Ω is indicated in beige (left axis).

The subaerial beach volume is predicted very accurately during the first 100 days of simulation (Figure 7.7). The evolution of the volume responds very well to the varying wave conditions, and the model attains an average RMAE = 0.10 during the first 100 days of simulation. Between days 100 - 112, the model does not predict the observed accretion, and the subaerial beach volume is under-predicted. From day 140 onward, the observed volume starts to depart more and more from the predicted volume, and the model skill drastically deteriorates, resulting in a RMAE = 0.67 after 220 days of simulation. The RMAE is presented in Figure 7.8 in light gray for the entire simulation.

The model predicts no net subaerial beach volume growth after 220 days of simulation, while the observations show that the subaerial beach starts accreting from day 100 onward. Although the model doesn't predict the right magnitude of accretion towards the end of the simulation, it performs very well during the first 100 days of simulations, and the beach responds correctly to the varying wave conditions. This suggests that there is not enough supply of sediment from the surf zone to rebuild the subaerial beach towards the pre-storm conditions.

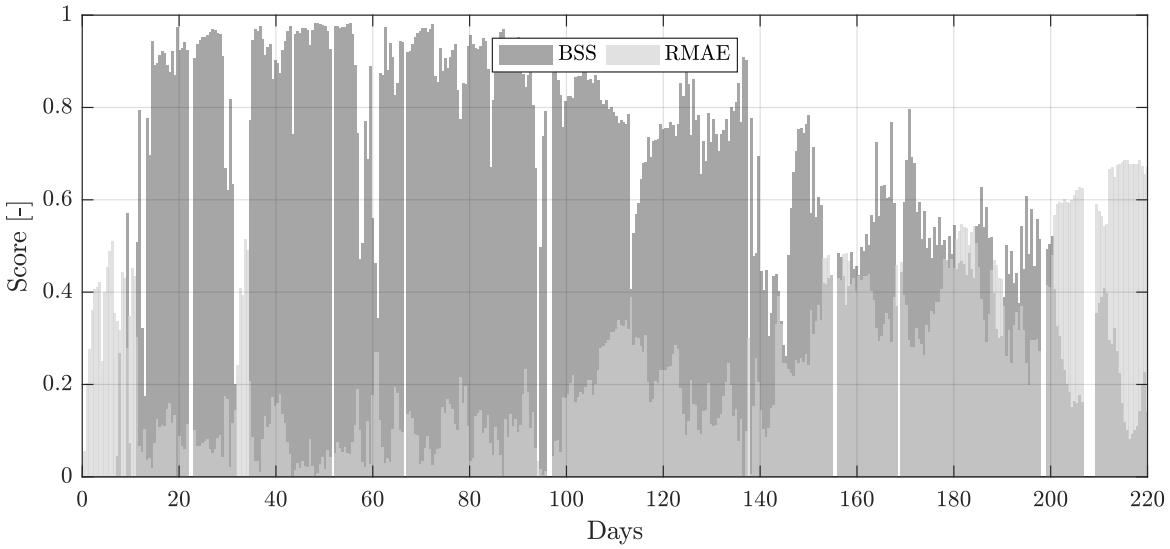

Figure 7.8: The model performance in terms of BSS (dark gray) and RMAE (light gray) throughout the entire simulated period (i.e. the first 220 days following the onset of recovery).

7.5 Discussion

From the bathymetry surveys (see Figure 7.3) was concluded that the offshore sand bar, composed of sediment which was eroded from the beach during the June 2016 storm, is migrating onshore, and acts as a sediment supply for the subaerial beach. After 105 days, the bar has migrated approximately 100 meters onshore according to the bathymetry survey (Figure 7.3), but the model shows little bed level changes near the bar (see Figure 7.9). This potentially explains why the model is not capable to correctly predict the recovery of the subaerial beach.

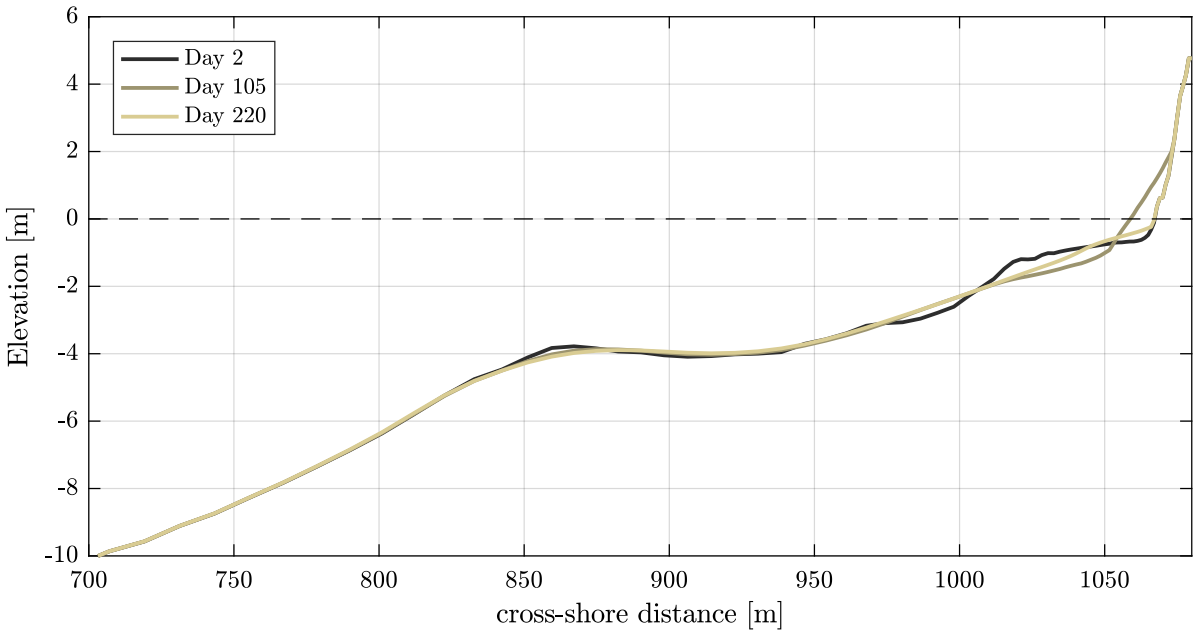

Figure 7.9: The post-storm bathymetry (black), and predicted bed level 105 days (brown) and 220 days (beige) following the onset of recovery (relative to June 8th 2016).

The rate of subaerial beach volume increase between days 100 - 112 is under-predicted by the model. The observed (left) and predicted (right) subaerial beach profile evolution in this period are illustrated in Figure 7.10.

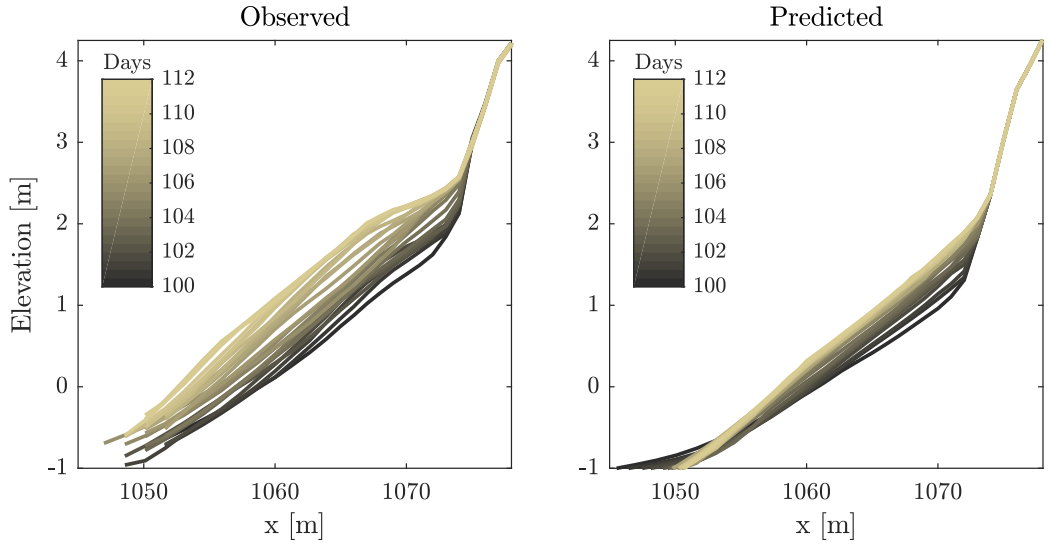

Figure 7.10: The observed (left) and predicted (right) subaerial beach profile evolution from day 100 to 112. The days are indicated by the shading, and evolve from black to beige in time.

The subaerial beach profile is rapidly accreting, and sediment is deposited over the entire beachface, causing a seaward progradation of the beachface, as well as horizontal growth and the formation of a berm (Figure 7.10 – left). Although the model also predicts horizontal as well as vertical growth (right figure), the supply of sediment from further offshore is absent.

Another interesting phenomenon is the subaerial volume increase around day 200, when the waves are relatively energetic ($\Omega \geq 5$). The observed (left) and predicted (right) subaerial beach profile evolution from day 194 to 206 are illustrated in Figure 7.11.

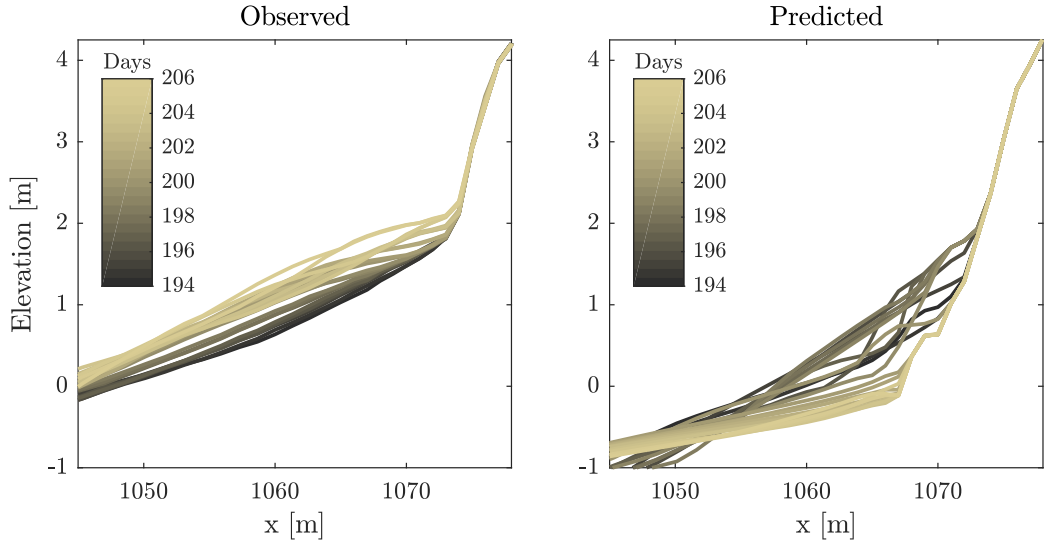

Figure 7.11: The observed (left) and predicted (right) subaerial beach profile evolution from day 194 to 206. The days are indicated by the shading, and evolve from black to beige in time.

It is not strange that the model predicts profile flattening and erosion of the subaerial beach, since the wave conditions are fairly energetic and dissipative ($\Omega \geq 5$), and are even considered as storm conditions ($\Omega \geq 4$, fllowing Phillips, 2018). It is counter-intuitive that there is such a significant berm growth during these conditions. However, the welding of the sand bar might be an explanation, and potentially higher waves enhance sediment mobilisation up to a greater depth.

Additionally, alongshore sediment transport is of significant importance, since there is a net sediment import of 220 m^3/m along the considered cross-shore profile during the first 6 months of the recovery. This is not captured in a 1D model, and hence, the observed recovery can never be predicted by the model, since there is no input of sediment along the boundaries of the model.

7.5.1 Tuning the onshore sediment transport

The onshore migration of the sand bar is not captured by the model, and hence there is not enough sediment supply from the surf zone to predict the right magnitude of subaerial beach volume growth (see e.g. Figure 7.10). However, the magnitude of the onshore sediment transport in the surf zone can be tuned through calibrating the wave skewness and asymmetry-induced sediment transport (as discussed in Chapter 4).

The calibration factors for the wave skewness and asymmetry (f_{Sk} and f_{As} respectively) are slightly increased to mimic the effect of the onshore migration of the sand bar on the sediment supply from the surf zone. The parameter setting is presented in Table 7.2. f_{Sk} is increased from 0.24 to 0.27 and f_{As} is increased from 0.12 to 0.17.

Parameter	Description	Value
D_{50}	Grain diameter [m]	0.0003
f_{Sk}	Wave skewness factor	0.27
f_{As}	Wave asymmetry factor	0.17
$Turb$	Turbulence-induced sediment stirring model	WA
$bermslope$	Equilibrium swash slope	0.27
$f_{bermslope}$	Calibration factor	7.0
Ω_{min}	Threshold Ω value for equilibrium conditions	1.6
Ω_{max}	Threshold Ω value for storm conditions	4.5
γ_{slope}	Calibration factor runup height	1.25

Table 7.2: Parameter settings for the simulation of the recovery following the June 2016 storm. The calibration factors for the wave skewness and asymmetry were calibrated in order to tune the onshore sediment transport.

7.5.2 Results

The predicted profile evolution (solid black line) throughout the recovery period is compared to the observations (dashed black line) in Figure 7.12, with the post-storm (dotted line) and post-recovery (dashed-dotted line) profiles indicated in gray. The profiles are again presented approximately 18 days apart for the first 220 days following the onset of recovery.

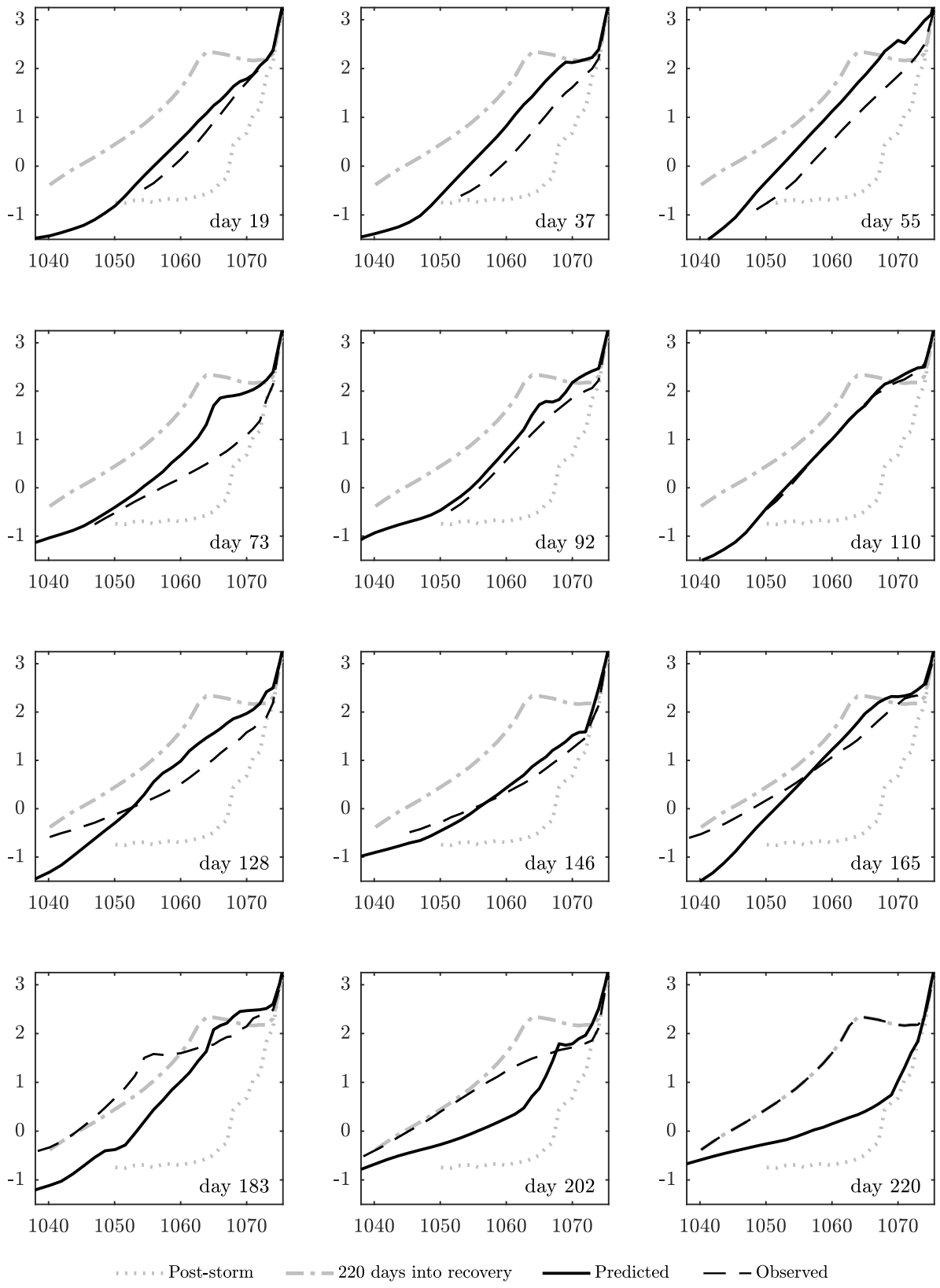

Figure 7.12: The predicted (solid) vs the observed (dashed) profile evolution throughout the first 220 days of the recovery. The post-storm profile is indicated with the dotted gray line, and the profile after 220 days is indicated with a dashed-dotted gray line.

The subaerial beach profile is accreting too rapidly during the first 73 days of simulation (Figure 7.12. However, from day 92 onward (i.e. panel 5 - 12 in Figure 7.12), the profile is predicted much more accurately with respect to the initial simulation (i.e. without calibration, see Section 7.4). From day 183 onward, the model still predicts a dissipative profile, which doesn't match the observations.

A comparison between the predicted (solid black line) and the observed (dashed black line) subaerial beach volume throughout the simulation is presented in Figure 7.13, accompanied by the dimensionless fall velocity Ω (left axis) in beige, indicating the wave conditions.

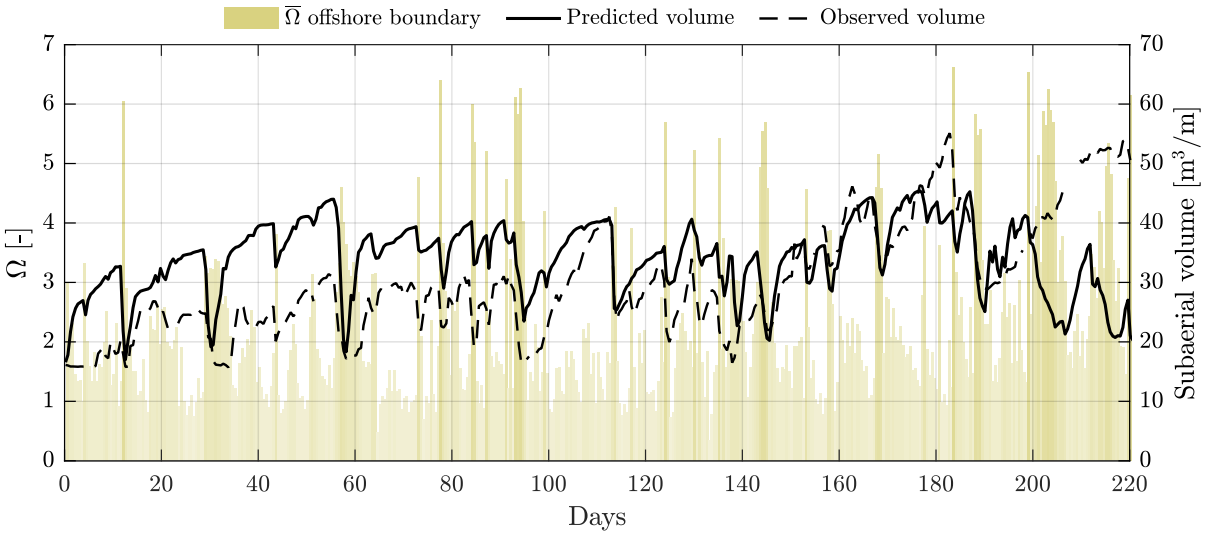

Figure 7.13: The predicted (solid) vs the observed (dashed) subaerial volume change during the first 220 days following the onset of recovery (right axis). The dimensionless fall velocity Ω is indicated in beige (left axis).

The slightly larger values for the wave skewness and asymmetry calibration factors enhance more onshore sediment transport immediately from the beginning of the simulation, which initially leads to an over-predicted rate of subaerial beach volume increase (Figure 7.13. However, after 100 days, possibly when the sand bar starts to act as a sediment source for the subaerial beach, the predicted volume matches the observations reasonably well. From day 183 onward, when the wave conditions are much more energetic, the model still predicts erosion, and the predicted subaerial beach volume is departing more and more from the observed trend.

The model attains a reasonable / good predictive skill throughout the simulation, especially between days 100 to 200. The average BSS = 0.74 and the RMAE = 0.16 during this 100-day period. The BSS and RMAE are calculated for the entire simulation and are presented in Figure 7.14.

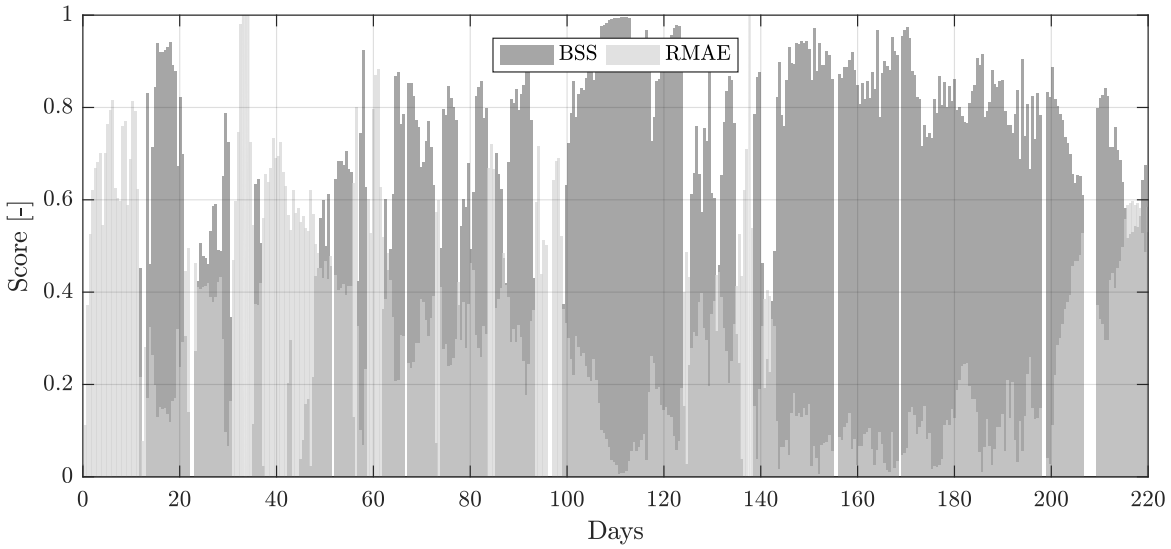

Figure 7.14: The model performance in terms of BSS (dark gray) and RMAE (light gray) throughout the entire simulated period (i.e. the first 220 days following the onset of recovery).

7.5.3 Conclusion

The two model innovation that were developed in this thesis (described Chapter 6) showed a major improvement of the model's ability to predict berm growth as well as storm-induced erosion following the April 2015 storm at Narrabeen Beach, using only one parameter setting. To validate the developed model, it is applied to simulate the recovery at Narrabeen Beach following the June 2016 storm.

The June 2016 storm event was much more devastating than the April 2015 storm, and the eroded beach sediment was deposited much further offshore. As a consequence, the model was not able to correctly predict the onshore transport of the eroded sediment, and hence the supply of sediment to the subaerial beach was insufficient to predict berm growth. Furthermore, alongshore sediment transport greatly contributes to the recovery of the subaerial beach, since there is a net sediment import of 220 m^3/m along the cross-shore profile within 6 months, which is not captured in the 1D model.

Despite the lack of sediment supply, and the under-predicted subaerial beach volume growth towards the end of the simulation, the model very accurately predicts the response of the subaerial beach to the wave conditions during the first 100 days of simulation, when the sand bar is not functioning as a sediment source yet. Although the model performance deteriorates towards the end of the simulation, the results are still promising.

Chapter 8

Conclusions and recommendations

8.1 Introduction

The main objective of this thesis was to develop a process-based wave-averaged model (XBeach Surfbeat) to successfully predict the recovery of the subaerial beach at Narrabeen Beach following the April 2015 storm. The research question was formulated as follows:

"How can a wave-averaged process-based model (XBeach Surfbeat) be applied to successfully model the recovery of the subaerial beach following a storm event?"

A straight-forward answer to this question is difficult to formulate, and in order to address the main research objective, a number of sub-objectives were formulated in Section 1.4. Section 8.2 discusses these sub-objectives and summarises the conclusions. Following the conclusions, recommendations are discussed in Section 8.3.

8.2 Conclusions

1. Identify the hydrodynamic and swash zone processes that are important for the onshore transport of sediment and the recovery of the subaerial beach.

A literature review (Chapter 2) provided insight in the morphodynamics of the coastal region. It was shown that reflective beaches are morphodynamically different from dissipative beaches, and that the concept of morphodynamic beach states (Wright and Short, 1984) is a useful tool to describe relations between wave conditions and the morphological response of the beach. Antecedent wave conditions determine the morphodynamics during calm conditions whereas the prevailing wave conditions are increasingly important during energetic conditions, when more wave energy is available. Wave skewness and asymmetry both enhance onshore sediment transport, and are of major importance for berm growth and beach recovery. In the swash zone, net onshore sediment transport is predominantly affected by turbulence, in- and exfiltration (i.e. groundwater flow), sediment characteristics and beachface gradient. Wave-induced setup and runup determine the vertical extent of sediment deposition, and empirical formulations provided a basis to estimate the wave-induced setup and total runup height on the beachface.

2. Analyse the recovery of the subaerial beach following the April 2015 storm at Narrabeen Beach, Australia.

Chapter 3 provided a description of the study site – Narrabeen Beach – and discussed the great amount of data that is collected over the past decades. Tide-by-tide (low tide) profiles were extracted from high-frequency (5 Hz) Lidar measurements, which were used to analyse the April 2015 storm at Narrabeen Beach, and subsequent natural recovery of the subaerial beach. The storm caused a total erosion of 53 m^3/m and a shoreline retreat of 30 meters at the Lidar transect. Subsequently, over a period of 76 days, the subaerial beach was rebuilt to its pre-storm state (in terms of subaerial beach volume, berm height and shoreline position). Throughout this recovery period, four different behavioural modes of the subaerial beach profile were identified (after Phillips, 2018), which are driven by the varying wave conditions as well as the tide.

Besides an analysis of the post-storm recovery at Narrabeen Beach, Chapter 3 provided a description of the site, and a review of the available data. Information on the environmental conditions (e.g. wave conditions, astronomical tide, sediment size) and post-storm bathymetry survey were used for the XBeach model setup (Chapter 4). Furthermore, the tide-by-tide profiles were used to quantify the model's predictive skill in terms of profile evolution and subaerial beach volume (Chapters 5 & 6). The high-frequency Lidar data also provided information on the runup height, which was used to develop an empirical formulation to estimate the total runup height based on the wave conditions and beach slope (discussed in Chapter 6).

3. Assess the performance of the currently available XBeach model formulations with respect to predicting the observed post-storm beach recovery at Narrabeen Beach, and potentially identify shortcomings:

    a. Assess the "standard" XBeach model performance; and
    b. Explore the recently-introduced "Bermslope" model (Roelvink and Costas, 2017).

The standard XBeach model is not capable of predicting berm growth and beach recovery at Narrabeen Beach. The model quickly forms a dissipative-looking profile without a berm, and with a mild beach slope, instead of the observed steep reflective beach. The Bermslope model (Roelvink and Costas, 2017) significantly improved the results as the latter model reproduced the steep beach slope and berm growth. However, the model persistently predicts onshore sediment transport and accretion, regardless of the wave conditions, and hence, episodic storm-induced erosion, and berm reset events are not captured. Furthermore, the vertical height of the berm is under-predicted. Chapter 5 highlights the two major shortcomings of the model, being the incorrect behaviour in terms of response to storm conditions, and the under-estimated vertical extent of sediment deposition.

4. Develop innovations to the model to account for wave-dependency in the Bermslope sediment transport correction, and account for incident band swash-induced sediment transport in the upper swash zone.

The shortcomings of the currently included formulations were highlighted in Chapter 5. A wave-dependency was incorporated in the model formulations, building up on the concept of morphodynamic beach states (Wright and Short, 1984) to address the first shortcoming – the model's disability to predict erosion during episodic energetic conditions. The magnitude of the swash zone sediment transport correction (in the Bermslope model) is made dependent on the dimensionless fall velocity Ω (Dean, 1973). For increasing Ω values, the "response" factor fac_{BS} decreases from $f_{bermslope}$ ($\Omega \leq \Omega_{min}$) to 0 ($\Omega \geq \Omega_{max}$), where Ω_{min} and Ω_{max} correspond

to threshold values for equilibrium and storm conditions respectively. This model innovation improves the behaviour and the ability to predict the correct response to energetic conditions. Despite the slightly less accurate post-recovery result (i.e. the BSS decreased from 0.78 to 0.71 and the RMAE increased from 0.03 to 0.19), the behavour throughout the recovery is captured much better. The recovery-averaged RMAE decreases from 0.24 to 0.09 due to the introduced wave-dependency, and the storm-induced profile changes are captured accurately (i.e. BSS = 0.9 following the reset event around day 10). Finally, the observed behavioural modes are more frequently assigned correctly (i.e. Mode 1 - 4 are predicted correctly 58%, 42% 80% and 43% of the time respectively).

A second model innovation was implemented to account for incident band swash-induced sediment transport in the upper swash zone, which is not resolved in XBeach Surfbeat. An empirical relation was developed (modified from Stockdon et al., 2006) and implemented in the XBeach model formulation to estimate the total runup height on the beachface. Subsequently, the by XBeach calculated (i.e. process-based) sediment transport in the swash zone is re-distributed up to the estimated runup height, while conserving mass. This innovation addresses the second shortcoming that was identified in Chapter 5 – the under-estimated height of the berm growth. The post-recovery profile is predicted much more accurately, as the BSS increased from 0.71 to 0.96 and the RMAE reduced from 0.19 to 0.021. Furthermore, the behavioural modes accompanied with vertical growth (i.e. Mode 2 and Mode 3) are assigned (correctly) more frequently.

5. Validate the developed XBeach model on the recovery of the subaerial beach following the June 2016 storm event at Narrabeen Beach, Australia.

The developed model is applied to (the first 220 days of) the recovery following the June 2016 storm, using exactly the same parameter setting as for the recovery following the April 2015 storm (Section 6.5). Without any calibration, the model performs very good the first 100 days of the recovery, with BSS $\geq$ 0.80 for over 70% of the time and an average RMAE of 0.10. After 100 days, however, the observations reveal a rapid volume growth which is not captured by the model. This is because the onshore migration of a sand bar is not captured by the model, and hence there is little sediment supply to the subaerial beach. Additionally, there is a significant net import of sediment due to alongshore transport (volume increase of 220 m^3/m after 6 months), which is not included in the 1D model either. From day 140 onward, the observed subaerial beach volume is progressively departing from the predicted volume due to the welding of the sandbar, and potentially sediment import due to alongshore processes. After 220 days, the model attains poor skill (BSS = 0.22 and RMAE = 0.78). However, the behaviour throughout the first 100 days is captured accurately, and the model results are promising for long-term simulations of beach recovery at (semi-)reflective beaches.

The calibration factors for the wave skewness and asymmetry are increased to push more sediment onshore, in order to represent the effect of the bar welding on the sediment supply to the subaerial beach. f_{Sk} is increased from 0.24 to 0.27, and f_{As} is increased from 0.12 to 0.17, which initially leads to an over-estimated rate of accretion (RMAE $\geq$ 0.8 occasionally). However, from day 100 onward, the subaerial beach profile is predicted very accurately (BSS $\geq$ 0.80 for 68% of the time), and towards day 200 the RMAE = 0.20 and BSS = 0.80. Eventually, the model still lacks berm growth towards the end of the simulation, which is a limitation of the 1D modelling approach rather than a shortcoming of the model.

8.3 Recommendations & future work

With respect to the model innovations that were developed in the present thesis, certain simplifications were made. Some of the assumptions or simplifications are believed to affect the quality of the results. The present section discusses these simplifications and highlights potential improvements to the formulation.

8.3.1 Wave-dependent Bermslope model

1. Wave-dependency was included in the Bermslope formulation through a response factor fac_{BS} which is inversely proportional to the dimensionless fall velocity Ω (Dean, 1973). This formulation is still based on a specified constant equilibrium swash slope (*bermslope*), which defines "target" swash slope, as well as the magnitude of the sediment transport correction. Chapter 2 however revealed that the beach slope is not constant. Initially, an attempt was made to describe a relation between the (antecedent) wave (and tide) conditions and the instantaneous swash slope, to replace the constant target *bermslope* for a more realistic varying equilibrium slope. However, the attempts were unsuccessful, and no relation could be derived that predicted the correct slope throughout the considered period. Further model development, to include a robust expression for a time-varying equilibrium swash slope rather than a constant slope potentially improves the capacity and applicability of the Bermslope model.

2. The wave-dependent Bermslope model (XBW – innovation 1) accounts for the rapid morphological response to increasingly energetic conditions, and a gradual adaptation during subsequent calm conditions (a kind of settling lag). For high instantaneous Ω values, the morphodynamics respond to the prevailing wave conditions, whereas for less energetic conditions (low Ω values) the antecedent conditions have a stronger relative contribution. This concept is based on several studies (e.g. Wright et al., 1985; Lippmann and Holman, 1990; Short and Aagaard, 1993), however, the considered antecedent time is believed to be chosen much too short. In the present formulation, the contribution of antecedent wave conditions is only spanning several hours (i.e. Figure 6.2), whereas the weighting of Wright et al. (1985) considered 50 antecedent days. Improving this weighting and increasing the considered antecedent temporal domain in the present formulation potentially improves the responsive behaviour.

3. The wave-dependency is introduced through the dimensionless fall velocity Ω. The definition of Ω is however not straightforward, and there are inconsistencies in the wave height that is used. The original formulation (Dean, 1973) used the breaking wave height. In the present study, a smoothed H_{rms} at the offshore boundary is used to calculate Ω, to ensure a stable definition of Ω. The breaking wave height H_b is a more appropriate representation for the wave conditions. Hence, a stable formulation for H_b should be developed in the XBeach source code to correctly determine the dimensionless fall velocity.

8.3.2 Swash zone sediment transport re-distribution model

1. Within the formulation for the runup height, use is made of a characteristic setup slope $\beta_{\langle\eta\rangle}$ and a swash slope β_S, which are both weighted average slopes taking into account the surf zone slope β_{sz} and swash slope β_{sw}. Although this formulation improved the accuracy for the present study, it is not consistent with the existing literature (Stockdon et al., 2006), and it is not validated on any other site or event. Either further research and model validation needs to be carried out to justify the approach followed in this thesis, or the present formulation needs to be adjusted in order to make it consistent with the existing literature.

2. The proposed formulation for the total runup height accounts for incident band runup as well as infragravity band runup in an empirical way. The infragravity motions are however already resolved in XBeach Surfbeach. Currently the estimated total runup height is superimposed on the offshore water level to determine the vertical extent of the sediment re-distribution. Since the infragravity motions are resolved (process-based), an alternative formulation would be to only add the incident band component to the calculated infragravity runup. This approach should be tested and compared to the current formulation.

3. The present formulation of the runup height, as well as the sediment transport re-distribution, are coded in such a way that the model itself is still applicable in a 2D simulation. However, the wave direction is not considered, and every wave is treated as if they approach the beach normally incident. furthermore, alongshore sediment transport is not considered either. Therefore, the formulation needs to be adjusted in order to make the re-distribution suitable for 2D modelling studies.

4. Finally, the sediment transport re-distribution over the upper swash zone is currently only performed on the suspended sediment transport. Instantaneous bed sediment transport rates were found to be discontinuous in the swash zone (unlike the suspended sediment transport rates). Interpolation and spreading of these discontinuous shapes complicated the development too much, and hence it was decided to focus only on the suspended sediment transport re-distribution. Further model development needs to be carried out to include the bed sediment transport in the re-distribution over the upper swash zone.

Bibliography

Aarninkhof, S. G. J. 2003. *Nearshore Bathymetry Derived from Video Imagery.* Ph.D. thesis, Delft University of Technology. 26

Aarninkhof, S. G. J., I. L. Turner, T. D. T. Dronkers, M. Caljouw and L. Nipius. 2003. A video-based technique for mapping intertidal beach bathymetry. *Coastal Engineering* **49**, p. 275–289. 26

Ahrens, J. 2000. A fall velocity equation. *Journal of Waterway, Port, Coastal and Ocean engineering,* **126**(2), p. 99–102. 36

Andrews, D. G. and M. E. McIntyre. 1978. An exact theory of nonlinear waves on a Lagrangian-mean flow. *Journal of Fluid Mechanics* **89**(4), p. 609–646. 35

Bagnold, R. A. 1940. Beach formation by waves: some model experiments in a wave tank. *Journal of the Institution of Civil Engineers* **15**, p. 27–52. 14, 21

Bagnold, R. A. 1962. Mechanics of marine sedimentation. *Proceedings of the Royal Society of London A* **265**, p. 315–319. 19

Bagnold, R. A. 1966. *An approach to the sediment transport problem from general physics.* Tech. Rep., US Geological Survey Professional Paper, Washington, DC:. 19

Bainbridge, T. R. 1985. The Committee on Standards: precision and bias. *ASTM Standardization News* **13**, p. 44–46. 44

Baldock, T. E., P. Holmes and D. P. Horn. 1997. Low frequency swash motion induced by wave grouping. *Coastal Engineering* **32**, p. 197–222. 14

Baldock, T. E., P. K. Son, P. Manoonvoravong, M. P. Barnes and J. M. Alsina. 2007. Probabilistic-deterministic modelling of swash zone morphology. In: N. C. Kraus and J. D. Rosati, eds., Coastal Sediments 2007, Am. Soc. of Civ. Eng., Reston, Va., p. 272–285. 20

Bascom, W. H. 1951. The relationship between sand size and beach face slope. *Transactions, American Geophysical Union* **32**(6), p. 866–874. 21

Battjes, J. A. 1974. Surf similarity. In: Proceedings of the 14$^{\text{th}}$ Conference on Coastal Engineering, Copenhagen. ASCE, p. 466–480. 9

Battjes, J. A. and J. P. F. M. Janssen. 1978. Energy loss and set-up due to breaking of random waves. In: Proceedings of the 16$^{\text{th}}$ International Conference on Coastal Engineering, ASCE, New York, p. 569–587. 35

Booij, N., R. C. Ris and L. H. Holthuijsen. 1999. A third-generation wave model for coastal regions 1. Model description and validation. *Journal of Geophysical Research* **104**, p. 7649–7666. 26

Bosboom, J. and M. J. F. Stive. 2015. *Coastal Dynamics I.* Delft University of Technology. 1

Bosboom, J., S. G. J. Aarninkhof, A. J. H. M. Reniers, J. A. Roelvink and D. J. R. Walstra. 1997. *UNIBEST-TC 2.0 - overview of model formulations.* Tech. Rep. Report H2305, Delft Hydraulics. 19

Bowen, A. J., D. L. Inman and V. P. Simmons. 1968. Wave 'set-down' and 'set-up'. *Journal of Geophysical Research* **73**(8), p. 2569–2577. 11

Bruun, P. M. 1962. Sea level rise as a cause of shore erosion. *Journal of the Waterways and Harbors Division* **88**, p. 117–130. ASCE. 1

Butt, T., P. Russell, J. A. Puleo and G. Masselink. 2005. The application of Bagnold-type sediment transport models in the swash zone. *Journal of Coastal Research* **21**, p. 887–895. 19, 20

Davidson, M. A., K. D. Splinter and I. L. Turner. 2013. A simple equilibrium model for predicting shoreline change. *Coastal Engineering* **73**, p. 191–202. 2, 19

Davies, J. L. 1973. *Geographical Variation in Coastal Development.* Hafner, New York. 204 p. 23

Dean, R. G. 1973. Heuristic models of sand transport in the surf zone. In: Engineering Dynamics in the Surf Zone, Sydney, N.S.W. 1973, p. 208–214. 18, 58, 96, 98

DHI. 2014. *MIKE21 SW. Spectral Wave FM Module User Guide.* Danish Hydraulics Lab, Hørsholm, Denmark. 24, 39, 84, 85, 117, 120

Doering, J. C. and A. J. Bowen. 1995. Parameterization of orbital velocity asymmetries of shoaling and breaking waves using bispectral analysis. *Coastal Engineering* **26**, p. 15–33. 37

Dubois, R. N. 1972. Inverse relation between foreshore slope and mean grain size as a function of the heavy mineral content.. *Geological Society of America Bulletin* **83**, p. 871–876. 21

Emery, K. O. 1961. A simple method of measuring beach profiles. *Limnology and Oceanography* **6**(1), p. 90–93. 25

Forbes, D. L., G. S. Parkes, G. K. Manson and L. A. Ketch. 2004. Storms and shoreline retreat in the southern Gulf of St. Lawrence. *Marine Geology* **210**(1–4), p. 169–204. 2

Galappatti, G. and C. B. Vreughenhil. 1985. A depth integrated model for suspended sediment transport. *Journal of Hydraulic Research* **23**(4), p. 359–377. 36

Galvin, C. J. 1968. Breaker Type Classification on Three Laboratory Beaches. *Journal of Geophysical Research* **73**(12), p. 3651–3659. 9, 117

Galvin, C. J. 1972. *Waves on Beaches.*, chap. Wave breaking in shallow water. Academic Press, New York, N.Y., p. 413–456. 18

Grasso, F., H. Michallet and E. Barthélemy. 2011. Sediment transport associated with morphological beach changes forced by irregular asymmetric, skewed waves. *Journal of Geophysical Research* **116**, p. 1–12. 37

Guza, R. T. and A. J. Bowen. 1977. Resonant interactions from waves breaking on a beach. In: Proceedings of the 15$^{\text{th}}$ International Conference on Coastal Engineering, Honolulu., p. 560–579. 18

Guza, R. T. and D. L. Inman. 1975. Edge wave and beach cusps. *Journal of Geophysical Research* **80**, p. 2997–3012. 14, 18

Guza, R. T. and E. B. Thornton. 1982. Swash oscillations on a natural beach. *Journal of Geophysical Research* **87**(C1), p. 483–491. 12

Hanslow, D. and P. Nielsen. 1993. Shoreline set-up on natural beaches. *Journal of Coastal Research* **SI**(15), p. 1–10. 12

Hardisty, J. 1986. A morphodynamic model for beach gradients. *Earth Surface Processes and Landforms* **11**, p. 327–333. 14

Hardisty, J., J. Collier and D. Hamilton. 1984. A calibration of the Bagnold beach equation. *Marine Geology* **61**, p. 95–101. 20

Harley, M. D., I. L. Turner, A. D. Short and R. Ranasinghe. 2010. Interannual variability and controls of the Sydney wave climate. *International Journal of Climatology* **30**, p. 1322–1335. 25

Harley, M. D., I. L. Turner, A. D. Short and R. Ranasinghe. 2011a. A re-evaluation of coastal embayment rotation: The dominance of cross-shore versus alongshore sediment transport processes, Collaroy-Narrabeen Beach, SE Australia. *Journal of Geophysical Research Atmospheres* **116**(F04033). 23, 25, 26

Harley, M. D., I. L. Turner, A. D. Short and R. Ranasinghe. 2011b. Assessment and integration of conventional, RTKGPS and image-derived beach survey methods for daily to decadal coastal monitoring. *Coastal Engineering* **58**, p. 194–205. 25

Harley, M. D., I. L. Turner and A. D. Short. 2015. New insights into embayed beach rotation: The importance of wave exposure and cross-shore processes. *Journal of Geophysical Research: Earth Surface* **120**, p. 1470–1484. 25, 26

Harley, M. D., I. L. Turner, K. D. Splinter, M. S. Phillips and J. A. Simmons. 2016. Beach response to Australian East Coast Lows: A comparison between the 2007 and 2015 events, Narrabeen-Collaroy Beach. *Journal of Coastal Research* **S**(75), p. 388–392. 1, 25, 27

Harley, M. D., I. L. Turner, J. H. Middleton, M. A. Kinsela, D. Hanslow, K. D. Splinter and P. Mumford. 2017. Observations of beach recovery in SE Australia following the June 2016 east coast low. In: Proceedings of Coasts and Ports 2017. Cairns, Australia. 25, 81

Hasselmann, K., T. P. Barnett, E. Bouws, H. Carlson, D. E. Cartwright, K. Enke, J. A. Ewing, H. Gienapp, D. E. Hasselmann, P. Kruseman, A. Meerburg, P. Müller, D. J. Olbers, K. Richter, W. Sell and H. Walden. 1973. Measurement of wind-wave growth and swell decay during the joint north sea wave project (jonswap). *Ergänzungsheft zur Deutschen Hydrographischen Zeitschrift* **A 8**(12), p. 95. 38

Holman, R. A. 1986. Extreme value statistics for wave run-up on a natural beach. *Coastal Engineering* **9**, p. 527–544. 12

Holman, R. A. and A. H. Sallenger Jr. 1985. Setup and swash on a natural beach. *Journal of Geophysical Research* **90**(C1), p. 945–953. 11, 67, 68, 72

Holman, R. A. and J. Stanley. 2007. The history and technical capabilities of Argus. *Coastal Engineering* **54**, p. 477–491. 25

Hsu, T. J. and B. Raubenheimer. 2006. Modelling sediment transport in the inner-surf and swash zones. *Continental Shelf Research* **26**, p. 589–598. 15

Hughes, M. G. and T. E. Baldock. 2004. Eulerian flow velocities in the swash zone: field data and model predictions. *Journal of Geophysical Research* **109**(C08009). 14

Hughes, M. G. and I. Turner. 1999. The beachface. In: A. D. Short, ed., Beach and shoreface morphodynamics, Wiley, p. 119–144. 13

Hughes, M. G., G. Masselink and R. Brander. 1997. Flow velocity and sediment transport in the swash-zone of a steep beach. *Marine Geology* **138**, p. 91–103. 20

Hunt, I. A. 1959. Design of seawalls and breakwaters. *Journal of Waterways and Harbours Division, ASCE* **85**(WW3), p. 123–152. 12

Iribarren, C. R. and C. Nogales. 1949. Protection des Ports. In: Proceedings of the XVII$^{\text{th}}$ International Navigation Congress, Section II, Communication, 4, Lisbon, pp. 31–80. 10

Komar, P. D. 1976. *Beach Processes and Sedimentation.* Englewood Cliffs (New Jersey), Prentice-Hall, xii et 429 p. 21

Kriebel, D. L. and R. G. Dean. 1993. Convolution method for time-dependent beachprofile response. *Journal of Waterway, Port, Coastal, and Ocean Engineering* **119**(2), p. 204–226. 2, 19

Larson, M. and M. C. Kraus. 1995. Prediction of cross-shore sediment transport at different spatial and temporal scales. *Marine Geology* **126**, p. 111–127. 20

Larson, M. and N. C. Kraus. 1989. *SBEACH: Numerical model for simulating storminduced beach change; Report 1. Empirical foundation and model development.* techreport, U.S. Army Corps of Engineers, Washington, DC. 19

Lippmann, T. and R. Holman. 1990. The spatial and temporal variability of sand bar morphology. *Journal of Geophysical Research* **95**(C7), p. 11575–11590. 18, 60, 98

Longuet-Higgins, M. S. and R. W. Stewart. 1960. Changes in the form of short gravity waves on long waves and tidal streams. *Journal of Fluid Mechanics* **8**, p. 565–583. 8

Longuet-Higgins, M. S. and R. W. Stewart. 1962. Radiation stress and mass transport in gravity waves, with application to 'surf beats'. *Journal of Fluid Mechanics* **13**(4), p. 481–504. 7, 8, 11, 117

Longuet-Higgins, M. S. and R. W. Stewart. 1964. Radiation stresses in water waves: a physical discussion with applications. *Deep-Sea Research* **11**, p. 529–562. 11

Luijendijk, A., G. Hagenaars, R. Ranasinghe, F. Baart, G. Donchyts and S. G. J. Aarninkhof. 2018. The State of the World's Beaches. *Scientific Reports* **8**(5). 1

Masselink, G. and M. Hughes. 1998. Field investigation of sediment transport in the swash zone. *Continental Shelf Research* **18**, p. 1179–1199. 15

Masselink, G. and J. A. Puleo. 2006. Swash-zone morphodynamics. *Continental Shelf Research* **26**(5), p. 661–680. 13, 14, 15, 21

Masselink, G. and A. D. Short. 1993. The Effect of Tide Range on Beach Morphodynamics and Morphology: A Conceptual Beach Model. *Journal of Coastal Research* **9**, p. 785–800. 20, 21, 26

McCall, R. T., J. van Thiel de Vries, N. G. Plant, A. R. Van Dongeren, J. A. Roelvink, D. M. Thompson and A. Reniers. 2010. Two-dimensional time dependent hurricane overwash and erosion modeling at Santa Rosa Island. *Coastal Engineering* **57**(7), p. 668–683. 33

McCall, R. T., G. Masselink, T. G. Poate, J. A. Roelvink, L. P. Almeida, M. Davidson and P. E. Russell. 2014. Modelling storm hydrodynamics on gravel beaches with XBeach-G. *Coastal Engineering* **91**, p. 231–250. 33

McCall, R. T., G. Masselink, T. G. Poate, J. A. Roelvink and L. P. Almeida. 2015. Modelling the morphodynamics of gravel beaches during storms with XBeach-G. *Coastal Engineering* **103**, p. 52–66. 33

Miche, R. 1944. *Mouvements ondulatoires des mers en profundeur constante on decroisante.* Annales des Ponts et Chaussees. 9

Morris, B. D. and I. L. Turner. 2010. Morphodynamics of intermittently open-closed coastal lagoon entrances: New insights and a conceptual model. *Marine Geology* **271**(1–2), p. 55–66. 23

Morton, R. A., J. G. Paine and J. C. Gibeaut. 1994. Stages and Durations of Post-Storm Beach Recovery, Southeastern Texas Coast, U.S.A. *Journal of Coastal Research* **10**(4), p. 884–908. 1

Munk, W. H. 1949. Surf Beats. *Transactions of the American Geophysical Union* **30**, p. 849–854. 8

Nielsen, P. and D. J. Hanslow. 1991. Wave runup distributions on natural beaches. *Journal of Coastal Research* **7**(4), p. 1139–1152. 12, 67, 68, 72

Oliveira, F. 2014. Modelling beach morphological changes during episodic erosion-recovery events: preliminary results. In: 3as Jornadas de Engenharia Hidrográfica., p. 233–236. 2, 49

Osborne, P. D. and G. A. Rooker. 1997. Surf zone and swash zone sediment dynamics on high energy beaches: West Auckland, New Zealand. In: Coastal Dynamics 1997, ASCE, p. 814–823. 13, 117

Osborne, P. D. and G. A. Rooker. 1999. Sand re-suspension events in a high energy infragravity swash zone. *Journal of Coastal Research* **15**, p. 74–86. 14

Palmsten, M. L. and K. D. Splinter. 2016. Observations and simulations of wave runup during a laboratory dune erosion experiment. *Coastal Engineering* **115**, p. 58–66. 33

Pearson, Karl. 1904. 1904. *On the theory of contingency and its relation to association and normal correlation.* Drapers' Company Research Memoirs, Biometric Series I, Deptartment of Applied Mathematics, University of London. 45, 118

Pender, D. and H. Karunarathna. 2013. A statistical-process based approach for modelling beach profile variability. *Coastal Engineering* **81**, p. 19–29. 2, 33

Phillips, M. S. 2018. *Wave-driven recovery of sandy beaches following storm erosion.* phdthesis, UNSW Sydney. i, iii, 1, 4, 20, 21, 25, 27, 28, 43, 61, 80, 90, 96

Phillips, M. S., I. L. Turner, R. J. Cox, K. D. Splinter and M. D. Harley. 2015. Will the sand come back? Observations and characteristics of beach recovery. In: Australasian Coasts & Ports Conference. 1

Phillips, M. S., C. E. Blenkinsopp, K. D. Splinter, M. D. Harley and I. L. Turner. 2019. Modes of Berm and Beachface Recovery Following Storm Reset: Observations Using a Continuously Scanning Lidar. *Journal of Geophysical Research: Earth Surface* **124**, p. 720–736. 28, 48, 52, 63, 77

Pierson, W. J., Jr. and L. Moskowitz. 1964. A proposed spectral form for fully developed wind seas based on the similarity theory of S. A. Kitaigorodskii. *Journal of Geophysical Research* **69**(24), p. 5181–5190. 38

Puleo, J. A., R. A. Beach, R. A. Holman and J. S. Allen. 2000. Swash zone sediment suspension and transport and the importance of bore-generated turbulence. *Journal of Geophysical Research* **105**, pp. 17,021–17,044. 14, 15, 20

Ranasinghe, R., C. Swinkels, A. Luijendijk, D. Roelvink, J. Bosboom, M. Stive and D. Walstra. 2011. Morphodynamic upscaling with the MORFAC approach: Dependencies and sensitivities. *Coastal Engineering* **58**, p. 806–811. 36

Ranasinghe, R., R. Holman, M. de Schipper, T. Lippmann, J. Wehof, T. M. Duong, D. Roelvink and M. Stive. 2012. Quantifying Nearshore Morphological Recovery Time Scales using Argus Video Imaging: Palm Beach, Sydney and Duck, North Carolina. *Proceedings of 33rd International Conference on Coastal Engineering.* Santander, Spain. 1

Raubenheimer, B., R. T. Guza and S. Elgar. 2001. Field observations of wavedriven setdown and setup. *Journal of Geophysical Research* **106**(c3), p. 4629–4638. 11, 67, 72

Reniers, A. J. H. M., J. A. Roelvink and E. B. Thornton. 2004. Morphodynamic modeling of an embayed beach under wave group forcing. *Journal of Geophysical Research* **109**(C01030). 36

Rienecker, M. M. and J. D. Fenton. 1981. A Fourier approximation method for steady water waves. *Journal of Fluid Mechanics* **104**, p. 119–137. 37

Roelvink, D. and S. Costas. 2017. Beach berms as an essential link between subaqueous and subaerial beach/dune profiles. *Geo-Temas* **17**, p. 79–82. i, iii, 2, 3, 34, 38, 43, 50, 58, 96

Roelvink, D., A. J. H. M. Reniers, A. R. van Dongeren, J. van Thiel de Vries, R. T. McCall and J. Lescinski. 2009. Modelling storm impacts on beaches, dunes and barrier islands. *Coastal Engineering* **56**(11-12), p. 1133–1152. i, iii, 2, 19, 33, 34, 43

Roelvink, J. A. 1993. Dissipation in random wave groups incident on a beach. *Coastal Engineering* **19**, p. 127–150. 34

Roelvink, J. A. 2006. Coastal morphodynamic evolution techniques. *Coastal Engineering* **53**, p. 277–287. 36

Roelvink, J. A. and A. J. H. M. Reniers. 2012. *A guide to modeling coastal morphology.* World Scientific, 1st Edition edn. Singapore. 19

Ruessink, B. G., M. G. Kleinhaus and P. G. L. van den Beukel. 1998. Observations of swash under highly dissipative conditions. *Journal of Geophysical Research* **103**(C2), p. 3111–3118. 18

Ruessink, B. G., G. Ramaekersm and L. C. van Rijn. 2012. On the parameterization of the free-stream non-linear wave orbital motion in nearshore morphodynamic models. *Coastal Engineering* **65**, p. 56–63. 37, 127

Sallenger, A. H. 2000. Storm impact scale for barrier islands. *Journal of Coastal Research* **16**(3), p. 890–895. 2, 33

Shand, T. D., I. D. Goodwin, M. A. Mole, J. T. Carley, S. Browning, I. G. Coghlan, M. D. Harley, W. L. Peirson, Z. J. You and M. A. Kulmar. 2011. Coastal storm data analysis: provision of extreme wave data for adaptation planning. In: Proceedings of Coasts and Ports 2011. Perth, Australia. 25

Short, A. D. 1984. Beaches and nearshore facies: southeast Australia. *Marine Geology* **60**, p. 261–282. 23

Short, A. D. 2007. *Beaches of the New South Wales Coast, 2nd edition.* Sydney University Press. 23, 46

Short, A. D. and T. Aagaard. 1993. Single and multi-bar beach change models. *Journal of Coastal Research* **SI**(15), p. 141–157. 18, 60, 98

Short, A. D. and N. L. Trenaman. 1992. Wave climate of the Sydney region, an energetic and highly variable ocean wave regime. *Australian Journal of Marine and Freshwater Research.* **43**(4), p. 765–791. 23, 25

Short, A. D., A. C. Trembanis and I. L. Turner. 2000. Beach oscillations, rotation and the Southern Oscillation, Narrabeen Beach, Australia. In: Proceedings of the 27$^{\text{th}}$ International Conference on Coastal Engineering (ICCE), Sydney, Australia., p. 2439–2452. 26

Small, C. and R. J. Nicholls. 2003. A Global Analysis of Human Settlement in Coastal Zones. *Journal of Coastal Research* **19**(3), p. 584–599. 1

Soulsby, R. L. 1997. *Dynamics of marine sands: a manual for practical applications.* Thomas Telford, London. 36

Splinter, K. D. and M. L. Palmsten. 2012. Modeling dune response to an east coast low. *Marine geology* **329–331**, p. 46–57. 33

Splinter, K. D., I. L. Turner, M. A. Davidson, P. Barnard, B. Castelle and J. Oltman-Shay. 2014. A generalized equilibrium model for predicting daily to interannual shoreline response. *Journal of Geophysical Research: Earth Surface* **119**, p. 1936–1958. 2, 19

Splinter, K. D., M. D. Harley and I. L. Turner. 2018. Remote Sensing Is Changing Our View of the Coast: Insights from 40 Years of Monitoring at Narrabeen-Collaroy, Australia. *Remote sensing* **10**(1744). 26, 27

Stive, M. J. F., S. G. J. Aarninkhof, L. Hamm, H. Hanson, M. Larson, K. M. Wijnberg, R. J. Nicholls and M. Capobianco. 2002. Variability of shore and shoreline evolution. *Coastal Engineering* **47**, p. 211–235. 1

Stockdon, H. F., R. A. Holman, P. A. Howd and A. H. Sallenger Jr. 2006. Emperical parameterization of setup, swash, and runup. *Coastal Engineering* **53**(7), p. 573–588. 11, 12, 67, 68, 69, 70, 71, 80, 97, 99, 119

Stockdon, H. F., D. M. Thompson, N. G. Plant and J. W. Long. 2014. Evaluation of wave runup predictions from numerical and parametric models. *Coastal Engineering* **92**, p. 1–11. 33

Sutherland, J., A. H. Peet and R. L. Soulsby. 2004. Evaluating the performance of morphological models. *Coastal Engineering* **51**(8), p. 917–939. 44

Tucker, M. J. 1950. Surf beats: sea waves of 1 to 5 minutes' period. *Proceedings of the Royal Society A* **202**, p. 565–573. 8

Turner, I. L. and G. Masselink. 1998. Swash infiltration-exfiltration and sediment transport. *Journal of Geophysical Research* **103**(C13), pp. 30,813–30,824. 15

Turner, I. L., M. D. Harley, A. D. Short, J. A. Simmons, M. A. Bracs, M. S. Phillips and K. D. Splinter. 2016. A multi-decade dataset of monthly beach profile surveys and inshore wave forcing at Narrabeen, Australia. *Scientific Data* **3**(160024). 25, 26

Van der Westhuysen, A. J., A. van Dongeren, J. Groeneweg, G. van Vledder, H. Peters, C. Gautier and J. C. C. van Nieuwkoop. 2012. Improvements in spectral wave modeling in tidal inlet seas. *Journal of Geophysical Research* **117**(C00J28). 44

Van Dongeren, A., R. Lowe, A. Pomeroy, D. M. Trang, D. Roelvink, G. Symonds and R. Ranasinghe. 2013. Numerical modeling of low-frequency wave dynamics over a fringing coral reef. *Coastal Engineering* **73**, p. 178–190. 33

Van Dongeren, A. R., A. J. H. M. Reniers and J. A. Battjes. 2003. Numerical modeling of infragravity wave response during DELILAH. *Journal of Geophysical Research* **108**(C9). 38

Van Rijn, L. C., D. J. R. Walstra, B. Grasmeijer, J. Sutherland, S. Pan and J. P. T. Sierra. 2003. The predictability of cross-shore bed evolution of sandy beaches at the time scale of storms and seasons using process-based Profile models. *Coastal Engineering* **47**(3), p. 295–327. 44, 48

Van Rooijen, A. 2011. *Modelling Sediment Transport in the Swash Zone.* Master's thesis, Delft University. 2, 37

Van Thiel de Vries, J. S. M. 2009. *Dune Erosion During Storm Surges.* Ph.D. thesis, Delft University of Technology. 37

Walstra, D. J. R., L. C. van Rijn, M. van Ormondt, C. Brière and A. M. Talmon. 2007. The effects of bed slope and wave skewness on sediment transport and morphology. *Coastal Sediments* ASCE. 41, 134

Weir, F. M., M. G. Hughes and T. E. Baldock. 2006. Beach face and berm morphodynamics fronting a coastal lagoon. *Geomorphology* **82**, p. 331–341. 20, 21

Wright, L. D. and A. D. Short. 1984. Morphodynamic variability of surf zones and beaches: A synthesis. *Marine Geology* **56**, p. 93–118. i, iv, 5, 16, 18, 21, 25, 26, 58, 60, 95, 96

Wright, L. D., J. Chappell, B. G. Thom, M. P. Bradshaw and P. Cowell. 1979. Morphodynamics of reflective and dissipative beach and inshore systems: Southeastern Australia. *Marine Geology* **32**(1), p. 105–140. 16, 55

Wright, L. D., P. Nielsen, A. D. Short and M. O. Green. 1982. Morphodynamics of a macrotidal beach. *Marine Geology* **50**, p. 97–128. 21, 72

Wright, L. D., A. D. Short and M. O. Green. 1985. Short-term changes in the morphodynamic states of beaches and surf zones: An empirical predictive model. *Marine Geology* **62**, p. 339–364. 16, 18, 19, 21, 26, 58, 60, 98

Abbreviations

BSS Brier Skill Score. ii, iv, 44, 45, 48, 49, 52, 53, 55, 63–65, 77, 78, 80, 87, 88, 92, 93, 97, 114–117

ECL East Coast Low. 25, 27, 81

GLM Generalized Lagrangian Mean. 35

ICOL Intermittently Opening and Closing Lagoon. 23

LBT Longshore Bar-Trough. 16, 17, 83, 113

LTT Low-Tide Terrace. 16, 17, 113

MSE Mean Squared Error. 44

MSL Mean Sea Level. 27, 45, 48

RBB Rhythmic Bar-Beach. 16, 17, 113

Rel. BIAS Relative BIAS. ii, 44, 45, 55, 69–72, 115

RMAE Relative Mean Absolute Error. ii, iv, 44, 45, 48, 49, 52, 53, 63–65, 77, 78, 80, 87, 88, 92, 93, 97, 114–117

RR Ridge-Runnel. 16, 17, 113

RTR Relative Tide Range. 20

SCI Scatter Index. ii, iv, 44, 45, 55, 69–72

SSC Suspended Sediment Concentration. 14, 15

SSE south south-east. 23

TBR Transverse Bar-Rip. 16, 17, 113

TWL Total Water Level. 27, 30

UNSW University of New South Wales. v

WRL Water Research Laboratory. v

List of Symbols

α	Calibration factor
β	beach slope (general)
$\beta_{\langle\eta\rangle}$	Setup-affecting beach slope
β_f	Foreshore beach slope
β_{sw}	Swash zone slope
β_{sz}	Surf zone slope
β_S	Swash excursion-affecting beach slope
η	Local water level
η_0	Offshore water level
γ_b	Breaker index
γ_{jsp}	Peak enhancement factor (JONSWAP)
Ω	Dimensionless fall velocity
ω	Wave frequency
Ω_{max}	Threshold Ω for storm conditions
Ω_{min}	Threshold Ω for equilibrium conditions
$\overline{\theta}$	Main wave angle of incidence (JONSWAP)
ρ	Density (of water)
ρ_s	Stone density
$\langle\eta\rangle$	Wave-induced setup
θ	Wave direction
ξ	Irribarren number / Surf similarity parameter
A	Wave action
As	Wave asymmetry
C	Sediment concentration
c	Wave celerity
c^u	Sediment concentration (u-point)
c_0	Wave celerity in deep water

C_{eq} Equilibrium sediment concentration

c_g Wave group velocity

D_{50} Mean grain diameter

D_w Wave energy dissipation

E Wave energy

f_{As} Wave asymmetry calibration factor

f_{Sk} Wave skewness calibration factor

g Gravitational acceleration

H Wave height

h Local water depth

H_0 Deep water wave height

H_b Breaking wave height

h_b Water depth where waves break

H_{m0} Spectral significant wave height

H_{rms} Root mean square wave height

H_S Significant wave height

k Wave number

L Wave length

L_0 Deep water wave length

n Ratio of wave wrt wave group velocity

q Sediment transport rate

$q_{bermslope}$ Bermslope sediment transport correction

Q_b Fraction of broken waves

R Runup height

$R_{2\%}$ 2% exceedance runup height

S Swash excursion

s Measure for directional spreading (JONSWAP)

S_{IG} Infragravity band swash excursion

S_{inc} Incident band swash excursion

S_w Wave energy density

S_x	x-component of the Radiation stress
Sk	Wave skewness
T	Wave period
T_p	Spectral wave peak period
U_r	Ursell number
v^u_{mag}	Velocity magnitude (u-point)
w_s	Sediment fall velocity
z_b	Bed level

List of Figures

List of Tables

Appendix A

Parameter sensitivity

A.1 Introduction

For the calibration of the XBeach Surfbeat model, some parameters are believed to be more important or sensitive than others. Following the literature review in Chapter 2, the onshore sediment transport turns out to be the main source of the sediment that needs to be deposited on the beachface, to ensure both the vertical and horizontal growth of the berm. Wave non-linearity was found to be very effective for the net onshore transport of sediment in the surf zone. Furthermore, processes in the swash zone that appeared to be relecant for the sediment transport in the upper swash zone were turbulence and in- and exfiltration. This section identifies and discusses the relative importance of the following processes on the model results:

- *Wave non-linearity* – The effect of wave non-linearity on the sediment transport is accounted for by an additional velicity term u_a in the advection-diffusion equation (Equation 4.12). This velocity term includes the contribution of wave skewness and wave asymmetry (Equation 4.18), and is calibrated with the factors f_{Sk} and f_{As} respectively.

- *Turbulence-induced sediment stirring* – There are 3 models to translate the turbulence at the surface to the near-bed turbulence. The near-bed turbulence affects the sediment concentrantion, and hence transport.

- *Groundwater flow* – A groundwater flow module is implemented in XBeach, which can be turned on to take into account groundwater flow and infiltration on the beachface.

- *Dilatancy* – Dilatancy refers to the reduction in sediment mobilisation during overwash conditions as high uprush velocities cause a stabilisation of the grains. Therefore dilatancy affects the onshore sediment transport and potentially "limits" vertical growth of the berm.

The processes listed above are accounted for in the XBeach model formulation through the parameters that are summarised in Table 4.2. The table presents the default values, and shows the range of tested values to assess their sensitivity on the model results.

The parameter setting is presented in Table A.1, including the range of values for the parameters that were varied for the sensitivity analysis. The varied parameters are highlighted in light gray.

Parameter	Description	Value
$wavemodel$	Wave model	$Surfbeat$
g	gravitational acceleration	9.81
ρ_w	Water density	1025
ρ_s	Stone density	2650
D_{50}	Grain diameter [m]	0.0003
$form$	Sediment transport formulation	vanthiel_vanrijn
$waveform$	Wave non-linearity-induced sediment transport model	vanthiel
f_{Sk}	Wave skewness calibration factor	0.13 - 0.27
f_{As}	Wave asymmetry calibration factor	0.10 - 0.16
$Turb$	Turbulence-induced sediment stirring model	BA/WA/none
f_{mor}	Morphological acceleration factor	10
$gwflow$	Groundwater flow module	0 - 1
$dilatancy$	Dilatancy effect modelling	0 - 1
$bermslope$	Equilibrium swash slope	0.24
$f_{bermslope}$	Calibration factor	10
$\gamma_{bermslope}$	H/h criterion for the Bermslope model	1.0

Table A.1: Overview of the baseline parameter setting used for the parameter sensitivity.

The highlighted parameters in Table A.1 are varied to assess their individual effect on the results of the simulation. Various combinations of settings were tested, and the model simulations that were carried out for the present sensitivity analysis are summarised in Table A.2.

Run ID	Parameter				
	f_{Sk}	f_{As}	$Turb$	$gwflow$	$dilatancy$
sk13_as10	0.13	0.10	none	1	0
sk20_as10	0.20	0.10	none	1	0
sk27_as10	0.27	0.10	none	1	0
sk25_as10	0.25	0.10	none	1	0
sk25_as13	0.25	0.13	none	1	0
sk25_as16	0.25	0.16	none	1	0
Turb_none	0.25	0.10	none	1	0
Turb_WA	0.25	0.10	WA	1	0
Turb_BA	0.25	0.10	BA	1	0
gwf0_dil0	0.27	0.13	none	0	0
gwf0_dil1	0.27	0.13	none	0	1
gwf1_dil0	0.27	0.13	none	1	0
gwf1_dil1	0.27	0.13	none	1	1

Table A.2: Overview of all the model simulations that were carried out for the parameter sensitivity analysis. The Run ID (left column) indicates which parameter is tested or varied.

A.2 Wave non-linearity

As explained in Section 4.2.2, the wave shape is not resolved, and the effect of wave non-linearity on the sediment transport is captured in an additional velocity term u_a. The Skewness and Asymmetry are calculated with a method according to Ruessink et al. (2012), and the magnitude of each component can be tweaked by means of two calibration factors f_{Sk} and f_{As} (see Equation 4.18).

Wave skewness

The effect of wave skewness on the sediment transport is calibrated by means of a factor f_{Sk}. To assess the effect of this factor, three different values have been tested, of which the results are presented in Figure A.1.

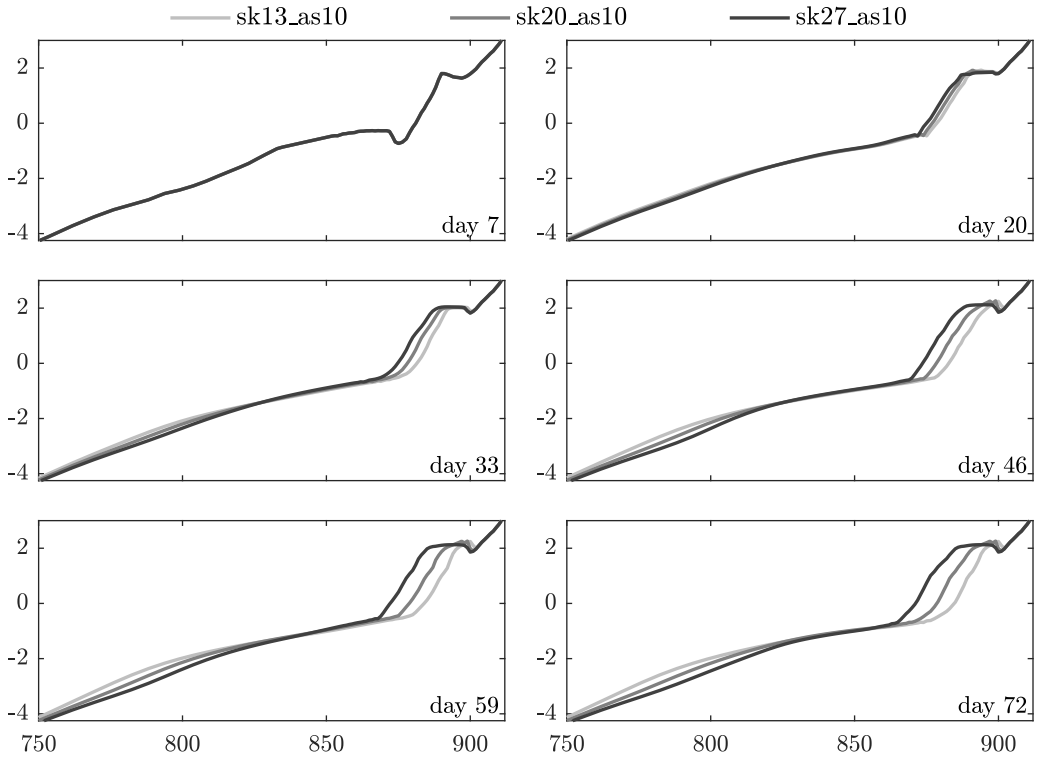

Figure A.1: The effect of increasing the calibration factor f_{Sk} on the evolution of the subaerial beach profile every 13 days throughout the simulation.

Clearly, the skewness strongly enhances the onshore sediment transport from the surf zone into the swash zone. For high values of f_{Sk}, the model predicts erosion in the left region of the domain (seaward of $x = 800$) which is deposited on the beachface. For lower values, there is an adverse sediment exchange between the swash zone and the surf zone. Figure A.2 shows the subaerial volume change in time for the three simulations.

The subaerial beach volume increase throughout the simulation is strongly enhanced by the wave skewness (Figure A.2). For increasing values of f_{Sk}, the rate of subaerial beach volume also increases, and the final volume is much larger. There is even a net erosion of the subaerial beach when $f_{Sk} = 0.10$.

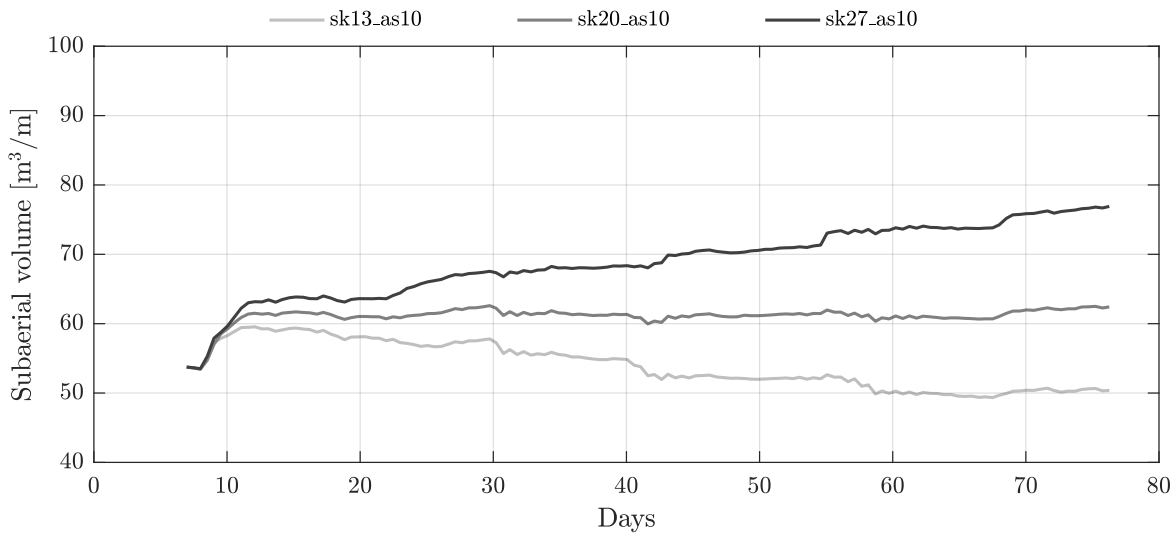

Figure A.2: The effect of increasing the calibration factor f_{Sk} on the subaerial beach volume throughout the simulation.

Figure A.1 shows the effect of the wave skewness on the cross-shore profile, and illustrates that the location of the berm is also affected by varying the calibration factor f_{Sk}. The berm location (cross-shore position and elevation) is calculated for each day throughout the simulation, and plotted in Figure A.3 for the three simulations. The colours indicate the simulation and the arrows represent the net propagation of the berm.

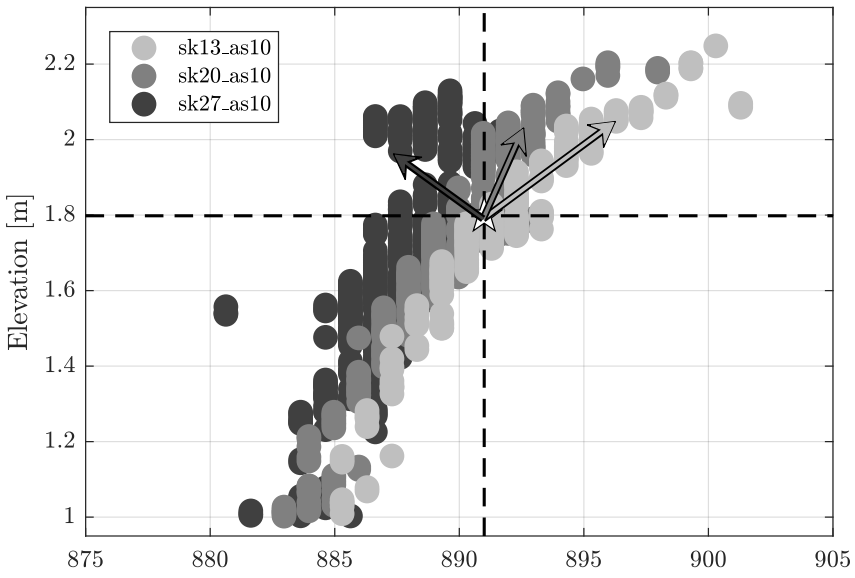

Figure A.3: The effect of increasing the calibration factor f_{Sk} on the cross-shore position (horizontal axis) and elevation (vertical axis) of the berm.

Wave asymmetry

The effect of wave asymmetry on the sediment transport is also calibrated by means of a factor f_{As}. Again, three different values have been tested to study the effect of this factor. The results of these simulations are presented in Figures A.4 - A.6. The profile evolution is illustrated in Figure A.4, where the subaerial beach profile is presented approximately 13 days apart.

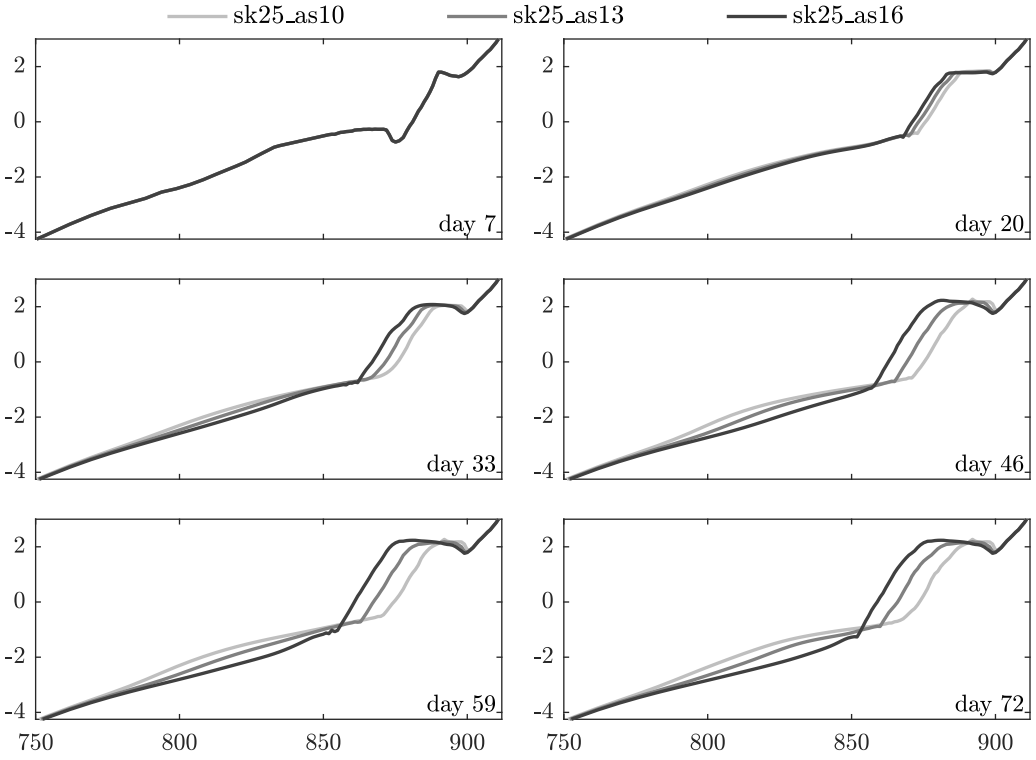

Figure A.4: The effect of increasing the calibration factor f_{As} on the evolution of the subaerial beach profile every 13 days throughout the simulation.

Figure A.4 shows that also the wave asymmetry enhances onshore sediment transport, and that the assigned values in these simulations result in unrealistically rapid accretion and hence should be reduced. The wave skewness calibration factor needed to be much higher to prevent the sediment transport from being offshore-directed. This is because the region where the wave asymmetry-induced sediment transport is most effective, overlaps more with the region where the Bermslope model performs. The Bermslope sediment transport correction is carried out in the swash zone, where the ratio $H/h \geq 1$, which corresponds to very shallow water.

The subaerial beach volume development for the three simulations is illustrated in Figure A.5.

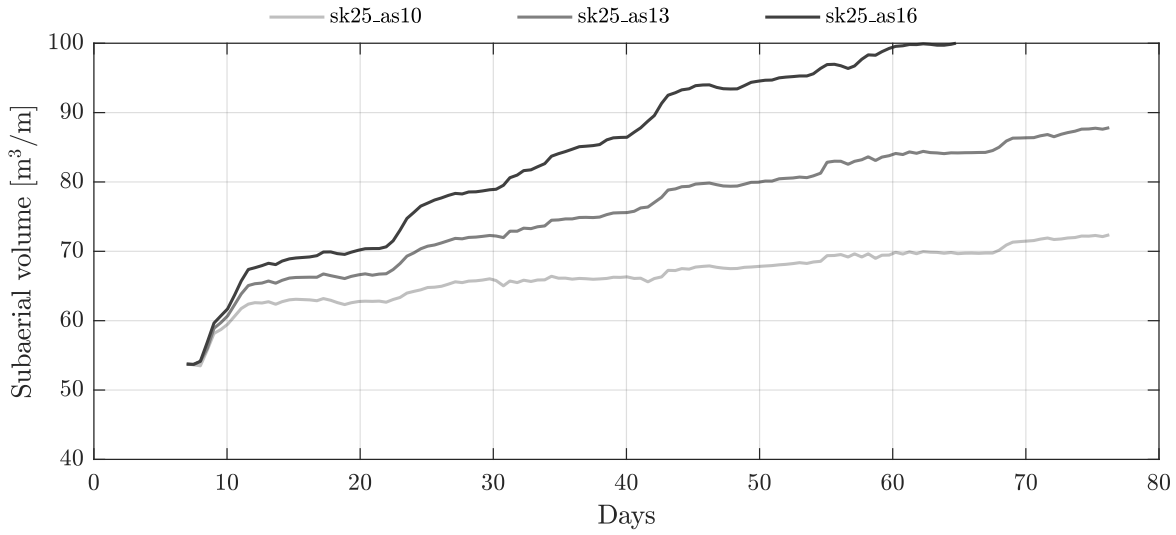

Figure A.5: The effect of increasing the calibration factor f_{As} on the subaerial beach volume throughout the simulation.

The subaerial beach volume increase throughout the simulation is also strongly enhanced by the wave asymmetry (Figure A.5). For increasing values of f_{As}, the rate of subaerial beach volume also increases, and the final volume is much larger. The simulation where $f_{As} = 0.16$ results in too much accretion f the subaerial beach. Figure A.5 illustrates again that the results are much more sensitive to the wave asymmetry factor than to the wave skewness factor. Small changes in f_{As} lead to very large differences in subaerial beach profile and hence volume changes.

The evolution of the berm location throughout the simulation is visualised in Figure A.6. The horizontal axis represents the cross-shore position of the berm crest, and the vertical axis shows the elevation.

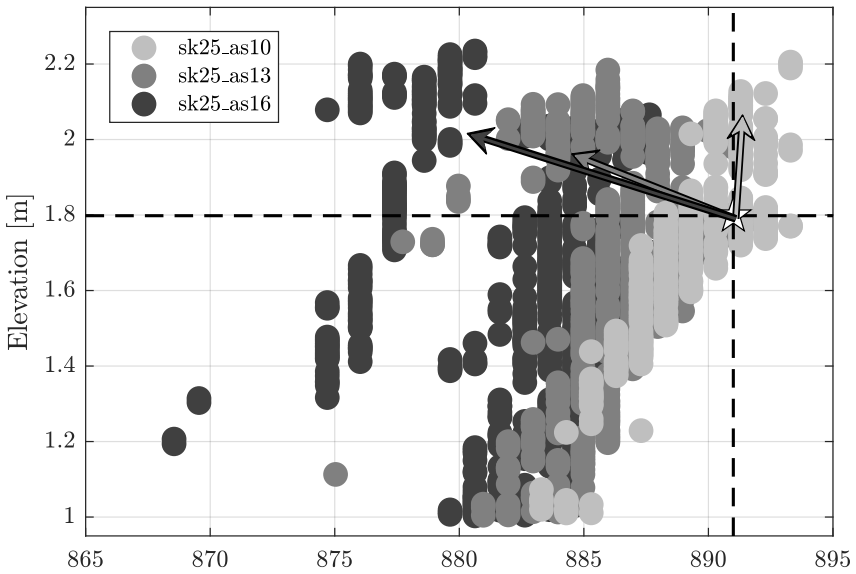

Figure A.6: The effect of increasing the calibration factor f_{As} on the cross-shore position (horizontal axis) and elevation (vertical axis) of the berm.

Turbulence model

As discussed in Section 2.5.2, turbulence enhances the mobilisation and transport of sediment. In XBeach, the near-bed turbulence can be derived from the surface turbulence in two ways. Additionally, it is possible to neglect the influence of surface turbulence on the sediment stirring. The results of these three model settings are compared in Fig.

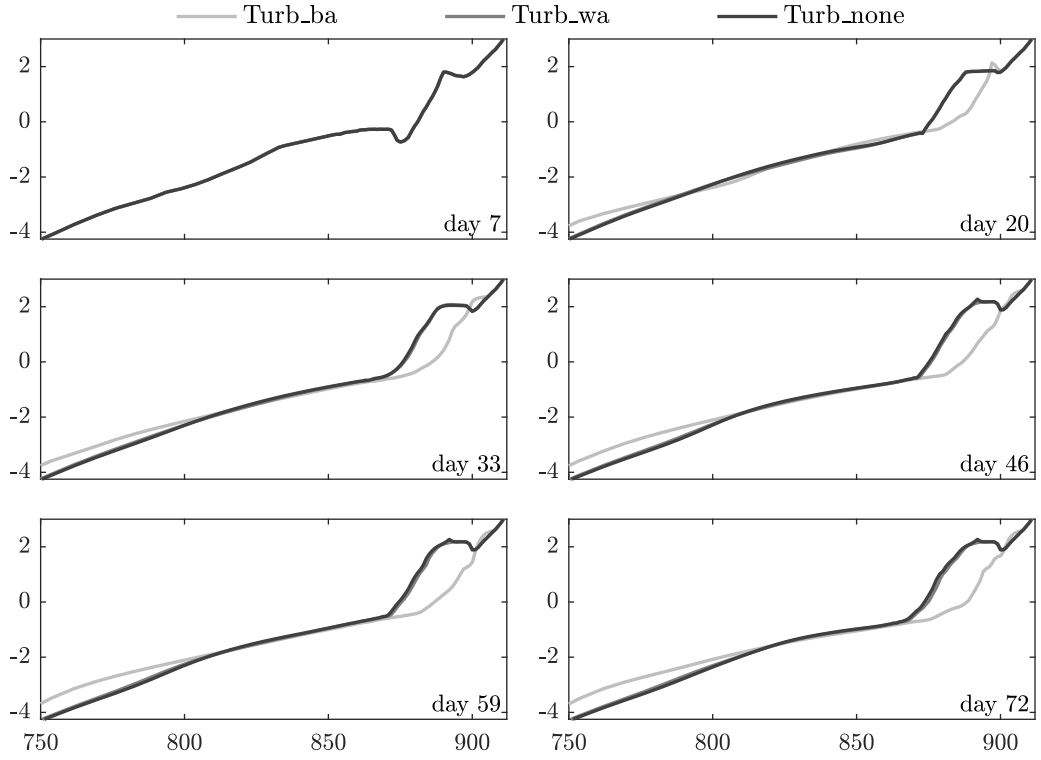

Figure A.7: The effect of using different turbulence-induced sediment stirring models on the evolution of the subaerial beach profile every 13 days throughout the simulation.

The type of model to compute near-bed turbulence strongly affects the behaviour of the beachface (Figure A.7). Figure A.7 shows that the bore-averaged turbulence formulation results in an unrealistically dynamic beachface. Within the first 13 days of simulation, the entire berm is eroded and deposited further offshore. The other two models show the same behaviour throughout the simulation, and perform much better. The bore-averaged model needs a lot more wave skewness- and asymmetry-induced onshore sediment transport (i.e. higher values of f_{Sk} and f_{As}) in order to not completely erode the beachface, even under low-energy wave conditions.

The subaerial beach volume is calculated throughout the entire simulation, and the evolution of the volume is illustrated in Figure A.8 for the three different simulations.

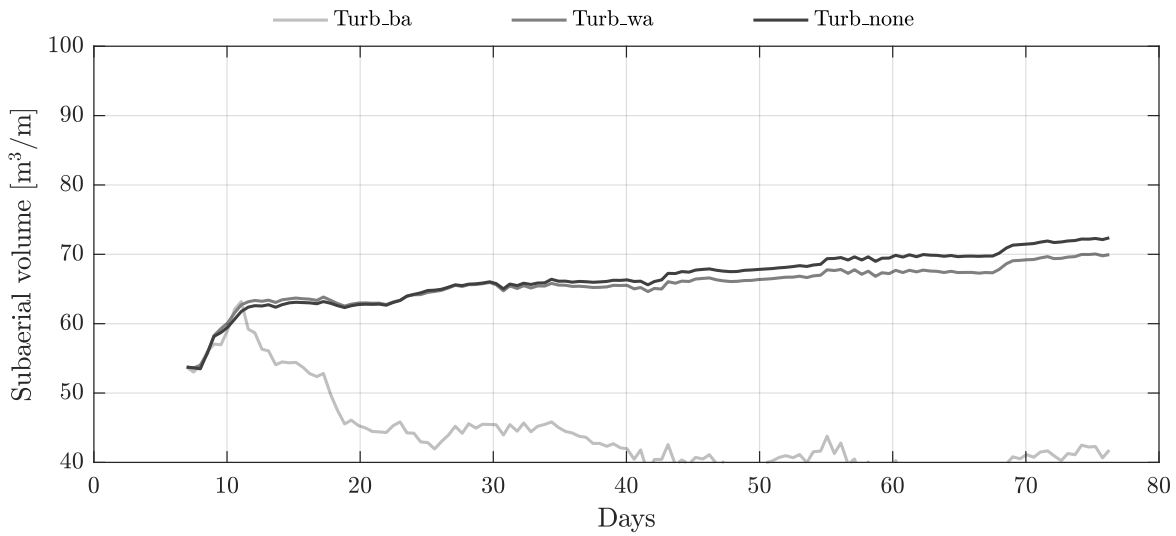

Figure A.8: The effect of different turbulence models on the subaerial beach volume throughout the simulation.

The subaerial beach volume change throughout the simulation is strongly affected by the turbulence model (Figure A.8). The bore-averaged model predicts erosion, while the wave conditions are mild. This turbulent model is therefore considered to be inappropriate for the simulation of berm growth, and is more suitable for modelling storm erosion.

The other two models (wave-averaged and no turbulence) show similar behaviour, and the wave-averaged turbulent model results in slightly less accretion towards the end of the simulation. During the first approximately 15 days, however, the wave-averaged model predicts a slightly more rapid accretion.

Groundwater flow and dilatancy

Realistically, as water over-tops the berm crest, the water that ends up on the beach infiltrates into the beach and does not stay on top of the berm. Therefore groundwater flow is assumed to be important for the simulation of subaerial beach growth. Since XBeach is used in 1D mode, the water that rushes up the beach, simply follows the same way back down the slope, also eroding the back of the berm. This is prevented, or at least reduced, by including groundwater flow and hence allowing for in- and exfiltration of the beachface.

Dilatancy is the effect of high uprush velocities stabilising the grains, and reducing the mobilisation and hence limiting erosion. Dilatancy is mainly considered important during overwash conditions.

The effect of turning on the groundwater flow module ("gwf1") or not ("gwf0"), and the effect of modelling dilatancy ("dil1") or not ("dil0") on the evolution of the subaerial beach profile is illustrated in Figure A.9. Note that the scale is different from the previous figures, to better illustrate the changes on the berm.

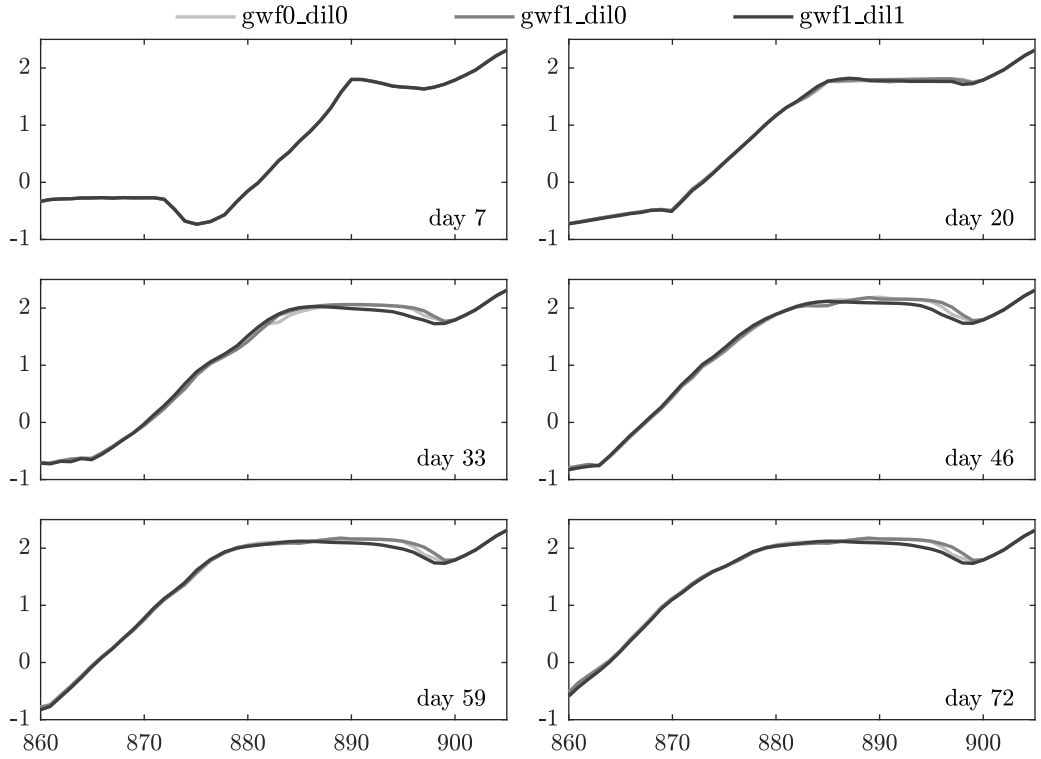

Figure A.9: The effect of modelling groundwater flow ("gwf1") or not ("gwf0"), and the effect of modelling dilatancy ("dil1") or not ("dil0") on the evolution of the subaerial beach profile every 13 days throughout the simulation.

As expected, the simulation that does take into account groundwater flow *gwf1_dil0* (without dilatancy) results in slightly more sediment deposition on top of the berm. Taking into account both dilatancy and groundwater flow in the simulation (gwf1_dil1), results in less overwash with respect to the other two simulations, due to the reduced sediment mobilisation.

The effect of modelling groundwater flow ("gwf1") or not ("gwf0"), and modelling dilatancy ("dil1") or not ("dil0") on the subaerial beach volume is illustrated in Figure A.10.

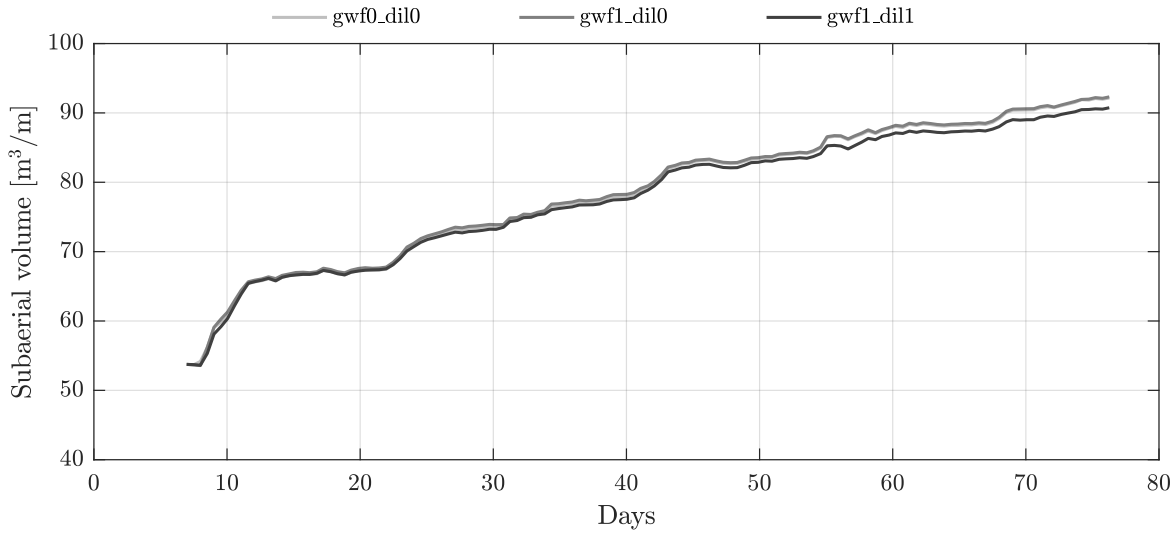

Figure A.10: The effect of modelling groundwater flow ("gwf1") or not ("gwf0"), and the effect of modelling dilatancy ("dil1") or not ("dil0") on the subaerial beach volume evolution.

The groundwater flow module does not affect the subaerial beach volume (Figure A.10), and only affects the shape of the berm. The dilatancy module, on the other hand, results in less subaerial beach volume growth, as expected.

A.3 Summary

The effect of wave skewness and asymmetry are accounted for by means of two calibration factors f_{Sk} and f_{As}, which both enhance onshore sediment transport. The effect of f_{As} is more prominent closer to the beachface, whereas f_{Sk} has more influence slightly further offshore, which agrees with the theory discussed in Section 2.3. The wave skewness acts more in the shoaling zone and is found to drive onshore bar migration (e.g. Walstra et al., 2007), and the asymmetry becomes more important in shallower water in the breaker and swash zone. Especially wave asymmetry is effective for the exchange of sediment between the inner surf zone and the subaerial beach. However, to ensure enough sediment supply from the surf zone, the wave skewness factor should tweaked as well.

The turbulence model has a major effect on the magnitude of the sediment transport in the surf zone and swash zone. The bore-averaged model BA results in the highest near-bed turbulent intensities, and hence the largest magnitude of sediment transport. As a consequence, the beach is unrealistically dynamic, even under very moderate wave conditions, leading to several meters of shoreline progradation and retreat within one tidal cycle. The wave-averaged formulation results in a much more stable beach profile, and gives a slightly smoother berm profile. Not taking into account the effect of surface-generated turbulence on the near-bed turbulent intensity yields the lowest magnitude of sediment transport.

Groundwater flow modelling takes into account the effect of in- and exfiltration, and affects the stability of the grains on the beachface. Turning on the groundwater flow module slightly enhances the onshore transport of sediment, and vertical growth of the berm.

As expected, dilatancy limits the mobilisation of sediment during uprush, and hence reduces the onshore and more importantly up-slope sediment transport. Therefore, the dilatancy module should not be used when one is interested in simulating berm growth.

Appendix B

Model calibration

B.1 Introduction

The present chapter summarises the simulations that have been performed during the calibration process and presents the resulting final parameter setting for all four modelling aproaches. The standard XBeach model calibration is discussed in Section B.2, the Bermslope model is discussed in Section B.3, The wave-dependent Bermslope model is presented in Section B.4 and finally, the swash zone sediment transport re-distribution model is discussed in Section B.5.

B.2 Standard XBeach

Parameter	Description	Value
$wavemodel$	Wave model	$Surfbeat$
g	gravitational acceleration	9.81
ρ_w	Water density	1025
ρ_s	Stone density	2650
D_{50}	Grain diameter [m]	0.0003
$form$	Sediment transport formulation	vanthiel_vanrijn
$waveform$	Wave non-linearity-induced sediment transport model	vanthiel
f_{Sk}	Wave skewness factor	0.45
f_{As}	Wave asymmetry factor	0.35
$Turb$	Turbulence-induced sediment stirring model	BA
f_{mor}	Morphological acceleration factor	10
$gwflow$	ground water flow module	1
$dilatancy$	Dilatancy effect modelling	0

Table B.1: Final parameter setting for the standard XBeach model after calibration.

Run ID	Parameter		
	f_{Sk}	f_{As}	$Turb$
sk10_as10_BA	0.10	0.10	BA
sk20_as20_BA	0.20	0.20	BA
sk30_as20_BA	0.30	0.20	BA
sk40_as20_BA	0.40	0.20	BA
sk50_as20_BA	0.50	0.20	BA
sk20_as30_BA	0.20	0.30	BA
sk30_as30_BA	0.30	0.30	BA
sk40_as30_BA	0.40	0.30	BA
sk50_as30_BA	0.50	0.30	BA
sk40_as35_BA	0.40	0.35	BA
sk50_as35_BA	0.50	0.35	BA
sk50_as35_BA	0.50	0.35	WA
sk50_as35_BA	0.50	0.40	WA
sk50_as35_BA	0.50	0.50	WA
sk50_as35_BA	0.50	0.50	none
sk45_as35_BA	0.45	0.35	BA

Table B.2: Overview of the calibration runs that resulted in the final parameter setting for the standard XBeach model.

B.3 XBeach Bermslope

Parameter	Description	Value
$wavemodel$	Wave model	$Surfbeat$
g	gravitational acceleration	9.81
ρ_w	Water density	1025
ρ_s	Stone density	2650
D_{50}	Grain diameter [m]	0.0003
$form$	Sediment transport formulation	vanthiel_vanrijn
$waveform$	Wave non-linearity-induced sediment transport model	vanthiel
f_{Sk}	Wave skewness factor	0.27
f_{As}	Wave asymmetry factor	0.14
$Turb$	Turbulence-induced sediment stirring model	none
f_{mor}	Morphological acceleration factor	10
$gwflow$	ground water flow module	1
$dilatancy$	Dilatancy effect modelling	0
$Bermslope$	Equilibrium swash slope	0.24
$f_{Bermslope}$	Calibration factor	10
$\gamma_{Bermslope}$	H/h criterion for $Bermslope$ index	1.0

Table B.3: Final parameter setting for the XBeach Bermslope model after calibration.

Run ID	Parameter				
	f_{Sk}	f_{As}	$bermslope$	$f_{bermslope}$	$Turb$
sk10_as10_bs15_bf15_WA	0.10	0.10	0.15	15.0	WA
sk20_as10_bs15_bf15_WA	0.20	0.10	0.15	15.0	WA
sk25_as10_bs15_bf15_WA	0.25	0.10	0.15	15.0	WA
sk30_as10_bs15_bf15_WA	0.30	0.10	0.15	15.0	WA
sk35_as10_bs15_bf15_WA	0.35	0.10	0.15	15.0	WA
sk40_as10_bs15_bf15_WA	0.40	0.10	0.15	15.0	WA
sk20_as15_bs15_bf15_WA	0.20	0.15	0.15	15.0	WA
sk20_as20_bs15_bf15_WA	0.20	0.20	0.15	15.0	WA
sk20_as15_bs20_bf15_WA	0.20	0.15	0.20	15.0	WA
sk25_as15_bs20_bf15_WA	0.25	0.15	0.20	15.0	WA
sk25_as15_bs22_bf10_WA	0.25	0.15	0.22	10.0	WA
sk30_as15_bs22_bf10_WA	0.30	0.15	0.22	10.0	WA
sk30_as11_bs24_bf10_WA	0.30	0.11	0.24	10.0	WA
sk30_as12_bs24_bf10_WA	0.30	0.12	0.24	10.0	WA
sk30_as13_bs24_bf10_WA	0.30	0.13	0.24	10.0	WA
sk30_as14_bs24_bf10_WA	0.30	0.14	0.24	10.0	WA
sk29_as14_bs24_bf10_WA	0.29	0.14	0.24	10.0	WA
sk28_as14_bs24_bf10_WA	0.28	0.14	0.24	10.0	WA
sk28_as13_bs24_bf10_WA	0.28	0.13	0.24	10.0	WA
sk27_as13_bs24_bf10_WA	0.27	0.13	0.24	10.0	WA
sk27_as14_bs24_bf10_WA	0.27	0.14	0.24	10.0	WA
sk27_as14_bs24_bf10_none	0.27	0.14	0.24	10.0	none
sk27_as15_bs24_bf10_none	0.27	0.15	0.24	10.0	none
sk27_as13_bs24_bf10_none	0.27	0.13	0.24	10.0	none

Table B.4: Overview of the calibration runs that resulted in the final parameter setting for the Bermslope model.

B.4 Wave-dependent Bermslope model

Parameter	Description	Value
$wavemodel$	Wave model	$Surfbeat$
g	gravitational acceleration	9.81
ρ_w	Water density	1025
ρ_s	Stone density	2650
D_{50}	Grain diameter [m]	0.0003
$form$	Sediment transport formulation	vanthiel_vanrijn
$waveform$	Wave non-linearity-induced sediment transport model	vanthiel
f_{Sk}	Wave skewness factor	0.28
f_{As}	Wave asymmetry factor	0.13
$Turb$	Turbulence-induced sediment stirring model	none
f_{mor}	Morphological acceleration factor	10
$gwflow$	ground water flow module	1
$dilatancy$	Dilatancy effect modelling	0
$Bermslope$	Equilibrium swash slope	0.24
$f_{Bermslope}$	Calibration factor	10
$\gamma_{Bermslope}$	H/h criterion for $Bermslope$ index	1.0
Ω_{min}	Threshold Ω value for equilibrium conditions	2.0
Ω_{max}	Threshold Ω value for storm conditions	4.0

Table B.5: Final parameter setting for the wave-dependent Bermslope model after calibration.

Run ID	Parameter				
	f_{Sk}	f_{As}	$bermslope$	$f_{bermslope}$	$Turb$
sk27_as14_bs24_bf10_none	0.27	0.14	0.24	10.0	none
sk27_as14_bs26_bf10_none	0.27	0.14	0.26	10.0	none
sk27_as14_bs28_bf10_none	0.27	0.14	0.28	10.0	none
sk27_as12_bs28_bf10_none	0.27	0.12	0.28	10.0	none
sk27_as12_bs26_bf10_none	0.27	0.12	0.26	10.0	none
sk27_as12_bs24_bf10_none	0.27	0.12	0.24	10.0	none
sk27_as13_bs24_bf10_none	0.27	0.13	0.24	10.0	none
sk27_as13_bs25_bf10_none	0.27	0.13	0.25	10.0	none
sk28_as12_bs24_bf10_none	0.28	0.12	0.24	10.0	none
sk28_as13_bs24_bf10_none	0.28	0.13	0.24	10.0	none
sk28_as14_bs24_bf10_none	0.28	0.14	0.24	10.0	none

Table B.6: Overview of the calibration runs that resulted in the final parameter setting for the wave-dependent Bermslope model.

B.5 Swash zone sediment transport re-distribution model

Parameter	Description	Value
$wavemodel$	Wave model	$Surfbeat$
g	gravitational acceleration	9.81
ρ_w	Water density	1025
ρ_s	Stone density	2650
D_{50}	Grain diameter [m]	0.0003
$form$	Sediment transport formulation	vanthiel_vanrijn
$waveform$	Wave non-linearity-induced sediment transport model	vanthiel
f_{Sk}	Wave skewness factor	0.24
f_{As}	Wave asymmetry factor	0.12
$Turb$	Turbulence-induced sediment stirring model	none
f_{mor}	Morphological acceleration factor	10
$gwflow$	ground water flow module	varied
$dilatancy$	Dilatancy effect modelling	0
$Bermslope$	Equilibrium swash slope	0.27
$f_{Bermslope}$	Calibration factor	7.0
$\gamma_{Bermslope}$	H/h criterion for $Bermslope$ index	1.0
Ω_{min}	Threshold Ω value for equilibrium conditions	1.6
Ω_{max}	Threshold Ω value for storm conditions	4.5
γ_{slope}	Calibration factor runup height	1.25

Table B.7: Final parameter setting for the swash zone sediment transport re-distribution model after calibration.

Run ID	Parameter						
	f_{Sk}	f_{As}	$bermslope$	$f_{bermslope}$	Ω_{min}	Ω_{max}	γ_{slope}
sk28_as14_bs24_bf10_20-40_100	0.28	0.14	0.24	10.0	2.0	4.0	1.00
sk25_as12_bs24_bf10_20-40_110	0.25	0.12	0.24	10.0	2.0	4.0	1.10
sk25_as12_bs24_bf10_20-40_120	0.25	0.12	0.24	10.0	2.0	4.0	1.20
sk25_as12_bs24_bf10_20-40_130	0.25	0.12	0.24	10.0	2.0	4.0	1.30
sk25_as11_bs24_bf10_20-40_125	0.25	0.11	0.24	10.0	2.0	4.0	1.25
sk25_as11_bs24_bf10_10-50_125	0.25	0.11	0.24	10.0	1.0	5.0	1.25
sk25_as11_bs24_bf10_15-45_125	0.25	0.11	0.24	10.0	1.5	4.5	1.25
sk25_as11_bs25_bf10_15-45_125	0.25	0.11	0.25	10.0	1.5	4.5	1.25
sk25_as11_bs25_bf05_15-45_125	0.25	0.11	0.25	5.0	1.5	4.5	1.25
sk25_as11_bs26_bf05_15-45_125	0.25	0.11	0.26	5.0	1.5	4.5	1.25
sk25_as11_bs26_bf06_15-45_125	0.25	0.11	0.26	6.0	1.5	4.5	1.25
sk25_as11_bs26_bf07_15-45_125	0.25	0.11	0.26	7.0	1.5	4.5	1.25
sk25_as11_bs26_bf08_15-45_125	0.25	0.11	0.26	8.0	1.5	4.5	1.25
sk25_as11_bs27_bf08_15-45_125	0.25	0.11	0.27	8.0	1.5	4.5	1.25
sk24_as11_bs27_bf08_15-45_125	0.24	0.11	0.27	8.0	1.5	4.5	1.25
sk24_as11_bs27_bf07_15-45_125	0.24	0.11	0.27	7.0	1.5	4.5	1.25
sk23_as11_bs27_bf07_15-45_125	0.23	0.11	0.27	7.0	1.5	4.5	1.25
sk24_as11_bs27_bf07_16-45_125	0.24	0.11	0.27	7.0	1.6	4.5	1.25
sk24_as12_bs27_bf07_16-45_125	0.24	0.12	0.27	7.0	1.6	4.5	1.25

Table B.8: Overview of the calibration runs that resulted in the final parameter setting for the swash zone sediment transport re-distribution model.

Sandy beaches are found along a large part of the world's coastline, and form the highly dynamic interface between sea and land. The dynamic nature of beaches is best displayed during storms as large amounts of sand are eroded in a matter of hours, potentially causing coastline retreat and increased vulnerability to the area behind it. Subsequent natural beach recovery is a longer-term wave-driven process where eroded sediment is transported back onshore to rebuild the beach towards its pre-storm conditions, providing coastal protection as it used to before. Understanding of post-storm beach recovery, and the ability to predict this process is therefore of fundamental importance for coastal managers.

While an abundance of numerical models is developed to simulate the morphological response to a storm event, the subsequent beach recovery is a process that has received significantly less attention. The complexity in numerical modelling of post-storm beach recovery lies in the importance of small-scale processes within a long-term period of months up to years, making process-based modelling of beach recovery still unsuccessfull today. The present thesis describes the development of a hybrid behavioural / process-based wave-averaged model (XBeach Surfbeat) that successfully predicts the recovery of the subaerial beach at Narrabeen Beach, Australia, following a severe storm erosion in April 2015.

Two innovations are developed and implemented in the XBeach model formulations. The concept of morphodynamic beach states is used to develop a behavioural model that predicts storm-induced erosion, as well as berm growth during subsequent calm conditions. A second innovation re-distributes the sediment transport in the upper swash zone, and accounts for incident band swash-induced sediment transport, which is not resolved in XBeach Surfbeat.The proposed model is applied to a second recovery period at Narrabeen Beach, following a devastating storm in June 2016, and shows promising results.

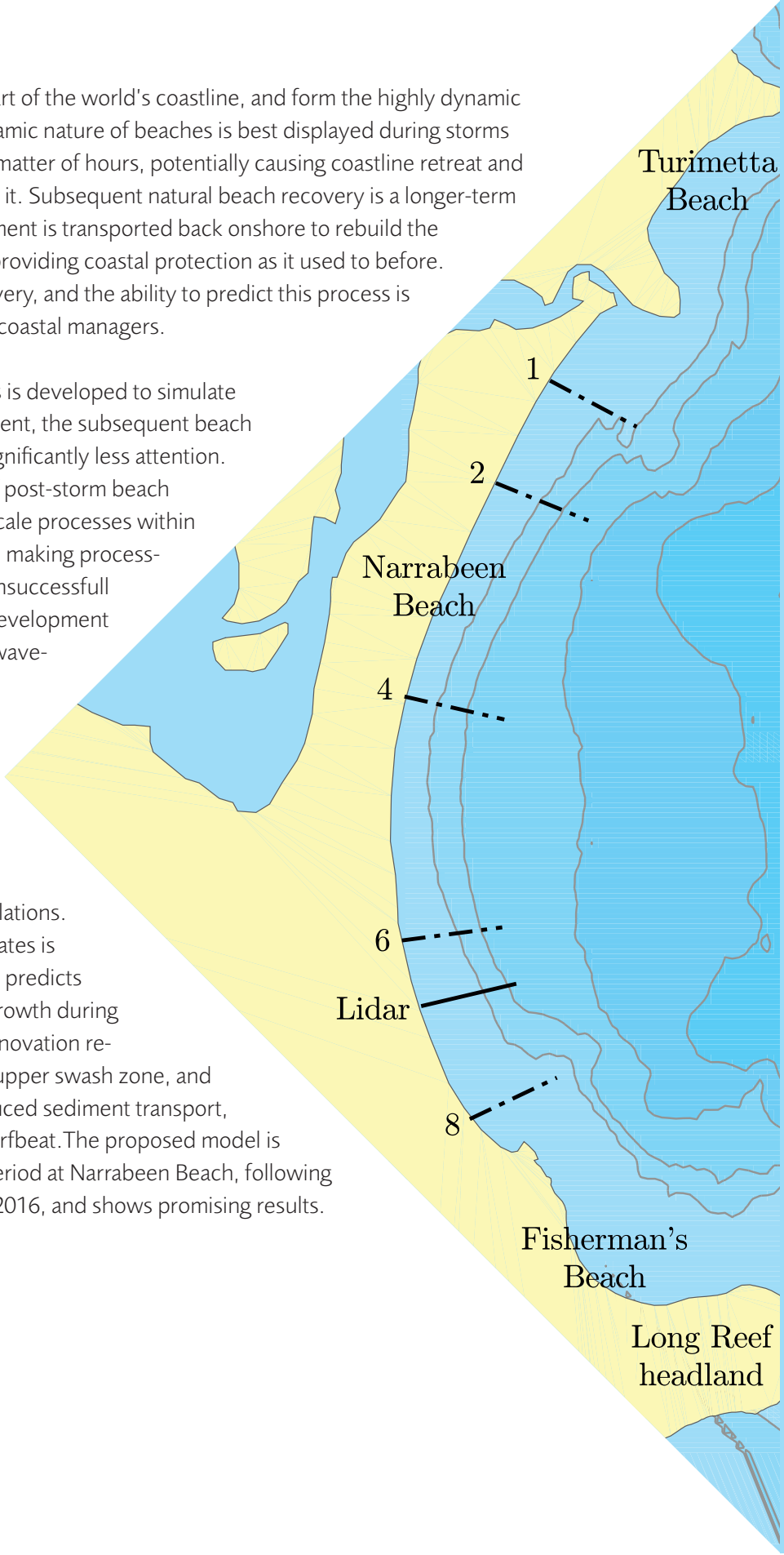

Deltares
Enabling Delta Life
TU Delft
UNSW SYDNEY
Water Research Laboratory
School of Civil and Environmental Engineering